Drag force in random arrays of mono- and bidisperse spheres

Renske Beetstra

Samenstelling promotiecommissie:

Prof. dr. ir. G.F. Versteeg, voorzitter	Universiteit Twente
Prof. dr. ir. J.A.M. Kuipers, promotor	Universiteit Twente
Dr. ir. M.A. van der Hoef, assistent-promotor	Universiteit Twente
Prof. dr. E.G. Flekkøy	University of Oslo, Noorwegen
Dr. ir. J.J. Derksen	TU Delft
Prof. dr. A.P. Philipse	Universiteit Utrecht
Prof. dr. ir. M.M.C.G. Warmoeskerken	Universiteit Twente
Dr. R.M. van der Meer	Universiteit Twente

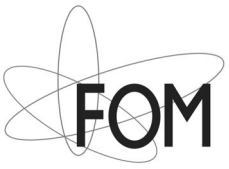

This work is part of the research programme of the 'Stichting voor Fundamenteel Onderzoek der Materie (FOM)', which is financially supported by the 'Nederlandse Organisatie voor Wetenschappelijk Onderzoek (NWO)'. This work was sponsored by the Stichting Nationale Computerfaciliteiten (National Computing Facilities Foundation, NCF) for the use of supercomputer facilities, with financial support from the Nederlandse Organisatie voor Wetenschappelijk Onderzoek (Netherlands Organization for Scientific Research, NWO).

Printed by PrintPartners Ipskamp, Enschede

ISBN 90-365-2232-3

DRAG FORCE IN RANDOM ARRAYS OF MONO- AND BIDISPERSE SPHERES

PROEFSCHRIFT

ter verkrijging van
de graad van doctor aan de Universiteit Twente,
op gezag van de rector magnificus,
prof. dr. W.H.M. Zijm,
volgens besluit van het College voor Promoties
in het openbaar te verdedigen
op donderdag 22 september 2005 om 16.45 uur

door

Renske Beetstra
geboren op 6 april 1976
te Voorburg

Dit proefschrift is goedgekeurd door de promotor

Prof. dr. ir. J.A.M. Kuipers

en de assistent-promotor

Dr. ir. M.A. van der Hoef

Contents

Summary

Fluid-particle contact is essential in many processes in the chemical, petrochemical, metallurgical and food processing industry. A reactor type which is particularly successful in establishing a thorough contact between fluid and particles, and has excellent heat and mass transfer properties, is the fluidised bed reactor. In these reactors the interaction between fluid and particles (drag force) balances the gravity acting on the particles, with the effect that the particles 'float' in the reactor, which enhances mixing properties.

The hydrodynamics of fluidised bed reactors are very complex, which has caused severe problems in the design and scale-up of these reactors in the past. Computational Fluid Dynamics (CFD) models may form an important tool in this process, as they provide the possibility to study the influence of several parameters in a cost efficient way. In the multilevel modelling approach a continuum model is used to simulate engineering scale fluidised beds. The closures which describe the effective particle-particle interaction can be obtained from discrete particle simulations, whereas the closures describing the effective fluid-particle interaction can be obtained from lattice-Boltzmann simulations. This thesis focuses on the last item: the derivation of accurate drag closures from lattice-Boltzmann simulations. The fluid-particle interaction (drag force) is an essential element of modelling fluidised bed reactors, that is, accurate closures are required to obtain realistic results from the higher order models. Currently combinations of the Ergun and Wen and Yu models are often used. However, these equations are 40 to 50 years old and their validity has recently been questioned. Furthermore, they do not take into account the effects of polydispersity and inhomogeneities that occur in practical applications.

The lattice-Boltzmann simulations of monodisperse systems showed that for

low Reynolds numbers the Kozeny-Carman equation is a good description of the drag force at high packing fractions. For more dilute systems a correction is necessary to ensure that the drag force does not vanish in the limit $\varepsilon \rightarrow 1$, which would follow from the Kozeny-Carman equation. For intermediate and high Reynolds numbers the results for the drag force showed a behaviour that is not a linear function of the Reynolds number, contrary to what is often assumed. The simulation data were compared to several literature models, none of which proved accurate over the entire range of porosities and Reynolds numbers. Therefore, a new relation is presented that fits the simulation data over the entire range of Reynolds numbers ($0 < Re < 1000$) and porosities ($0.4 < \varepsilon < 0.9$) with an average deviation of only 3 %. In the limit of $\varepsilon \rightarrow 1$, this relation yields a drag coefficient which is close to the expression by Turton and Levenspiel (1986), which provides the best fit to the experimental data for the drag on a single sphere.

Simulations of binary mixtures were performed with various diameter ratios ($0.25 < d_1/d_2 < 0.7$), porosities ($0.35 < \varepsilon < 0.9$), mixture compositions and Reynolds numbers ($0 < \langle Re \rangle < 500$). The relation that was derived from the monodisperse simulations proved capable of predicting the overall pressure drop over a binary system with an average deviation of less than 5 %. The drag force acting on an individual particle in a binary system was shown to be very different from the drag force on the same particle in a monodisperse system with identical porosity and Reynolds number. In order to correct for the effect of polydispersity, a new relation was derived from theoretical considerations using the Kozeny-Carman approximation. This relation was shown to be in very good agreement with the simulation data for all porosities and Reynolds numbers, provided that the diameter ratios are not very extreme. With an extra term the average deviation from the simulation results for the individual particle drag force was reduced to 4.5 % over the entire range. Simulations of a polydisperse system, consisting of four particle species, indicated that the validity of the correction factor is not limited to bidisperse systems. It is stressed that the difference between predictions from a model with this correction term and predictions from the classical drag models may be up to a factor of 5. The model that was originally proposed by Patwardhan and Tien (1985) gave similarly accurate results for the drag force on individual particles, but only after modification to incorporate the correct average diameter. For the use in larger scale numerical codes, the explicit expression suggested in this work will be far more practical.

Pressure drop measurements in mono- and bidisperse packed beds were performed in order to experimentally validate the numerical results. For low Reynolds numbers the agreement with the new relation was excellent, with an average deviation of around 5 %. In the intermediate Reynolds number regime the deviations were much larger (around 24 %) and systematic. It is anticipated that some systematic error was introduced in the calculation of the porosity or the viscosity. The deviation decreases for higher Reynolds numbers.

The new drag relations were implemented in the discrete particle model, with which two types of simulations were done: (*i*) the formation of a single bubble by a jet, and (*ii*) the segregation of a mixture of particles of different sizes. The results were compared to experiments with similar systems, where the focus was in particular on the effect of the boundary conditions and the drag models. From the single bubble simulations it could be concluded that a fine grid is necessary to obtain realistic structures in the bed. No definite conclusion could be drawn about the best drag model, although it should be noted that the Ergun/Wen and Yu model overestimated the bubble size. The difference between the model of Hill et al. (2001b) and the new model was negligible. The segregation simulations showed that the correction factor for polydispersity improves the predictions for the segregation rate considerably. The combination of the new drag relation and the correction factor gave the best results for the segregation rate. However, a one-to-one comparison proved difficult, since the segregation rate was found to be somewhat effected by the type of boundary conditions employed in the simulations.

A calculation of the inversion velocity in mixtures that differ in size and density showed that the new drag model is capable of predicting reasonably accurate values for this velocity. The correct trend was predicted when the composition is changed, in contrast to many literature relations.

Finally, the drag force in clusters was studied using lattice-Boltzmann simulations. The drag coefficient of irregularly shaped particles (clusters with zero inter-particle distance) agreed very well with literature values. When the inter-particle distance was increased, the drag force on the cluster increased as well due to the development of flow in between the particles. The drag force that individual particles in the clusters experience was shown to depend heavily on the shielding by other particles.

Samenvatting

Contact tussen een gas of vloeistof en vaste deeltjes is essentieel in talrijke processen in de chemische, petrochemische, metallurgische en voedselverwerkende industrie. Een type reactoren dat een goed contact tussen de vaste stof en het fluïdum combineert met uitstekende eigenschappen wat betreft warmte- en stofoverdracht is het gefluïdiseerde bed. De wrijvingskracht tussen gas (of vloeistof) en deeltjes is in deze reactoren zo groot, dat hij de zwaartekracht opheft zodat de deeltjes als het ware door de reactor gaan zweven, wat de menging in de reactor sterk bevordert.

De stroming in zo'n gefluïdiseerd bed is erg ingewikkeld, en daardoor zijn in het verleden al problemen ontstaan met het ontwerpen en opschalen van deze reactoren. Computermodellen kunnen hierbij uitkomst bieden, omdat deze het mogelijk maken de invloed van verschillende parameters op een grondige en goedkope manier te bestuderen. Het modelleren van deze reactoren op verschillende niveaus lijkt hierbij uitermate veelbelovend. Hierbij wordt de hele reactor gemodelleerd met behulp van een continuum model. Informatie over de interactie tussen deeltjes onderling wordt verkregen met behulp van het discrete deeltjes model, en informatie over de wrijving tussen gas en deeltjes uit simulaties met het rooster-Boltzmann model. In dit proefschrift ligt de nadruk op het meest fundamentele niveau: de afleiding van een vergelijking voor de interactie tussen deeltjes en fluïdum, die in de modellen op grotere schaal gebruikt kan worden om de wrijvingskracht te beschrijven. Deze wrijving is een essentieel onderdeel van het model van een gefluïdiseerd bed, en een nauwkeurige vergelijking hiervoor kan de overeenstemming van de simulatieresultaten met de praktijk sterk verbeteren. Tot nu toe worden in de meeste modellen combinaties van de Ergun en Wen en Yu vergelijkingen gebruikt, die beide al 40 tot 50 jaar oud zijn en waarvan de geschiktheid steeds meer in twijfel wordt getrokken. Bovendien houden deze modellen geen rekening met de aanwezigheid van inhomogeniteiten en polydispersiteit

(mengsels), die in de praktijk vrijwel onvermijdelijk blijkt te zijn.

Uit de rooster-Boltzmann simulaties van monodisperse systemen bleek dat bij lage Reynoldsgetallen de Kozeny-Carman vergelijking een goede beschrijving geeft van de wrijvingskracht in systemen met een hoge pakkingsfractie. In verdunde systemen is een correctie nodig die ervoor zorgt dat het gedrag voor $\varepsilon \to 1$ ook juist wordt weergegeven. In het geval van middelmatige en hoge Reynoldsgetallen bleek dat de wrijvingskracht geen lineaire functie van het Reynoldsgetal is, in tegenstelling tot wat vaak wordt aangenomen. Een nieuwe vergelijking beschrijft de simulatiedata voor alle Reynoldsgetallen ($0 < Re < 1000$) en porositeiten ($0.4 < \varepsilon < 0.9$) met een gemiddelde afwijking van slechts 3 %.

Simulaties van bidisperse systemen zijn gedaan met variabele diameter ratio's ($0.25 < d_1/d_2 < 0.7$), porositeiten ($0.35 < \varepsilon < 0.9$), samenstelling van het mengsel en Reynoldsgetallen ($0 < \langle Re \rangle < 500$). De vergelijking die was gevonden voor de wrijvingskracht in een monodispers systeem blijkt ook de drukval over een bidispers systeem goed te beschrijven, met een gemiddelde afwijking van de simulatieresultaten van minder dan 5 %. Individuele deeltjes in een binair systeem ondergaan een wrijvingskracht die sterk afwijkt van de kracht op hetzelfde deeltje in een monodispers systeem met gelijke porositeit en Reynoldsgetal. Een correctiefactor die was afgeleid op basis van theoretische overwegingen geeft goede resultaten bij het beschrijven van de individuele wrijvingskracht op de deeltjes voor alle porositeiten en Reynoldsgetallen, mits de diameters van de deeltjes niet te veel verschillen. Met een extra term kan voor dit laatste gecorrigeerd worden, en is de gemiddelde afwijking nog slechts 4.5 % voor alle simulaties. Simulaties van een polydispers systeem met vier verschillende deeltjes geven aan dat de correctiefactor ook in dit geval geldig is. Het verschil tussen voorspellingen voor de kracht op een enkel deeltje met en zonder deze correctie kan oplopen tot een factor 5. Het model dat oorspronkelijk is voorgesteld door Patwardhan en Tien (1985) geeft - met een aanpassing voor de juiste gemiddelde diameter - vergelijkbare resultaten voor de wrijvingskracht op individuele deeltjes. Dit model is echter ingewikkelder in gebruik vergeleken met de correctiefactor die in dit proefschrift wordt voorgesteld, waardoor deze laatste toch de voorkeur verdient.

De nieuwe vergelijking voor de wrijvingskracht is experimenteel gevalideerd met behulp van drukvalmetingen in mono- en bidisperse gepakte bedden. Voor lage Reynoldsgetallen was de overeenstemming uitstekend, met een gemiddelde afwijking van rond de 5 %. Bij middelgrote Reynoldsgetallen

werd echter een systematische afwijking van rond de 24 % gevonden, die waarschijnlijk veroorzaakt is door een fout in de bepaling van de porositeit of de viscositeit. Bij hogere Reynoldsgetallen werd de afwijking minder.

De nieuwe vergelijkingen voor de wrijvingskracht zijn geïmplementeerd in het discrete deeltjes model, waarmee vervolgens simulaties van twee verschillende systemen gedaan zijn, namelijk de vorming van een enkele bel door een jet en de segregatie van een mengsel met verschillende deeltjesgroottes. De simulatieresultaten zijn vergeleken met experimentele data, waarbij de gebruikte randvoorwaarden en wrijvingsmodellen in de simulatie zijn gevarieerd. Uit de belvormingssimulaties bleek dat het nodig is om een fijn grid te gebruiken om de structuren in het bed terug te vinden in een simulatie. Een conclusie over het beste model voor de wrijvingskracht kan op basis van deze simulaties niet worden getrokken, al is duidelijk dat met de combinatie van Ergun en Wen en Yu de belgrootte overschat wordt. Het verschil tussen het nieuwe model en dat van Hill e.a. (2001b) is echter zeer klein bij deze simulaties. De segregatie simulaties maken duidelijk dat de segregatiesnelheid aanzienlijk beter voorspeld wordt indien de correctiefactor voor polydispersiteit gebruikt wordt. De combinatie van de nieuwe vergelijking met de correctiefactor geeft de beste resultaten.

Berekeningen van de snelheid waarbij inversie optreedt - in systemen met deeltjes met verschillende groottes en dichtheden - laten zien dat deze redelijk goed voorspeld wordt met de nieuwe vergelijkingen voor de wrijvingskracht. Bovendien wordt ook de juiste trend voorspeld indien de samenstelling van het mengsel gewijzigd wordt, iets waartoe veel literatuurmodellen niet in staat zijn.

Tot slot is gekeken naar de wrijvingskracht die op clusters van deeltjes werkt. De kracht op clusters waarin de deeltjes elkaar raken komt goed overeen met literatuurwaarden. Bij een toenemende afstand tussen de deeltjes neemt de totale kracht op het cluster ook toe door de ontwikkeling van stroming tussen de deeltjes. De wrijvingskracht op individuele deeltjes in het cluster is afhankelijk van de mate van afscherming van dat deeltje door andere deeltjes.

Chapter 1

Introduction

Abstract

Computational Fluid Dynamics constitute an emerging tool for the design and optimisation of fluidised beds and other types of multiphase chemical reactors. In the multi-level modelling approach, discussed in this chapter, various models provide information on processes prevailing at different length and time scales: the lattice-Boltzmann model is used to obtain accurate closure relations for the drag force, the discrete particle model does the same for the particle-particle interaction, and with these closures continuum models can simulate engineering scale reactors more accurately. This thesis focuses on the most fundamental step of the process: the derivation of an accurate relation for the drag force between fluid and particles.

1.1 Introduction

Fluid-solid contact is essential for many processes in the chemical, petrochemical and metallurgical industries, and encountered as well in energy production and food processing. To illustrate this heterogeneously catalysed reactions are mentioned, where the intensity of the contact between gas or liquid and solid is directly linked to the chemical conversion rate. If the reactants cannot reach the catalyst, the reaction does not occur. Other systems where fluid-solid contact is crucial are those where one of the reactants is a solid that reacts with a gas or liquid. The burning of solid fuels and the formation of syngas from coal are important processes where this type of contact occurs, as well as the production of polymers where the solid polymer is formed as the result of a fast heterogeneously catalysed chemical transformation.

A thorough contact between a fluid and a solid can be achieved in several reactor types. The packed bed is the oldest and most often applied reactor type to contact gases or liquids with solid catalysts. In these reactors the fluid flows through a vessel filled with solid particles, usually comprising a catalyst. Smaller particles have a larger specific surface area, thereby increasing the contact area between the phases and thus the heat and mass transfer rates. However, when smaller particles are used the pressure drop increases strongly as well. Another disadvantage of the packed bed is possible 'hot spot' formation if the (exothermic) reaction becomes too fast at a certain position in the bed, which could ultimately lead to a runaway reaction.

To achieve high heat and mass transfer rates, fluidised beds are often applied. In these reactors, the particles are not fixed in the bed, but move along with the carrier phase, which in most cases is gaseous. The gas and solids mixing rate is high compared to that encountered in packed bed reactors, thus preventing the formation of hot spots. Furthermore, the pressure drop over a fluidised bed is usually lower than over a packed bed, and limited to the buoyant weight of the particulate phase. Well-known examples of fluidised bed processes are the fluidised catalytic cracking (FCC) of oil in a riser-reactor and the polymerisation of olefins in a fluidised bed.

Important factors that determine the intensity of the fluid-solid contact, and therefore the efficiency of the reactor, are the amount of particles residing in the reactor, their size, fluid properties like density and viscosity, and the

(relative) velocities of fluid and particles. These factors determine the force that the phases exert on each other, the so-called drag force, and with that the flow behaviour in the reactor.

1.2 Drag force

When a solid particle moves in a fluid, or when a gas or liquid finds its way through a bed of solid particles, the fluid and solids exert a force on each other. This force is called the drag force, and its magnitude depends (among others) on the slip velocity between the fluid and the solid and the porosity of the system. In everyday life we encounter the action of the drag force for example when the wind is blowing through a tree and moves its leaves or even the entire tree. Its action is felt as well when cycling against the wind.

In chemical engineering applications the importance of the drag force is found in its direct relation to the pressure drop over a reactor, heat exchanger or entire plant, and therefore to the loss of energy during a process. Pressure drop often constitutes an important issue for the design and operation of processes. Usually a compromise has to be found between energy loss due to drag force and variables like process selectivity and equipment size to determine the optimal process conditions.

For the abovementioned reasons a thorough understanding of the drag force in particulate flows is of fundamental importance for many applications in chemical engineering. Establishing accurate drag force relations has challenged both the physics and the engineering community for many years, and no consensus has been reached on this subject. The aim of this thesis is to contribute to this subject area by use of lattice-Boltzmann simulations, which will be discussed later.

1.3 Fluidisation

When a gas or liquid flows through a bed of particles contained in a vessel, at a certain velocity the drag force becomes so large that it balances gravity and the particles start to 'float' in the reactor. This phenomenon is called fluidisation and the velocity at which it commences is called the minimum fluidisation velocity. When the velocity is increased further the particles are

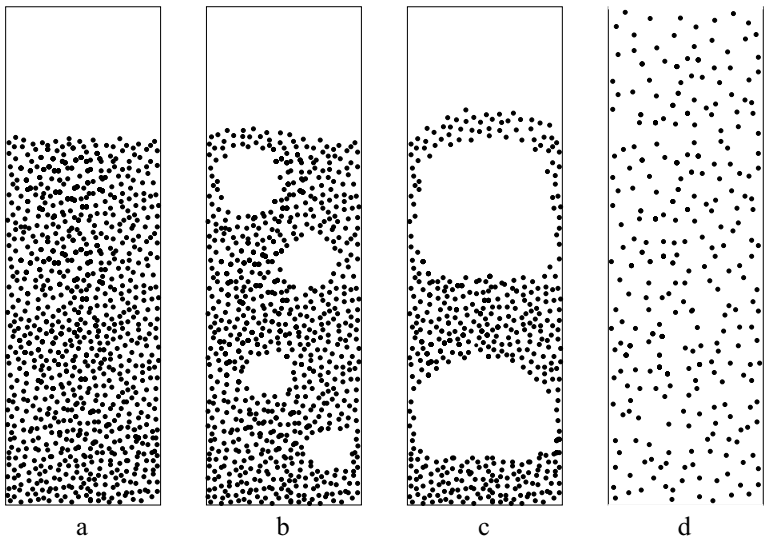

Figure 1.1: Various regimes in a fluidised bed reactor. a: homogeneous expansion; b: bubbling; c: slugging; d: fast fluidisation (riser).

lifted higher and the porosity increases with it, until at the minimum bubbling point the excess gas starts to form bubbles. At even higher velocities slugs may occur (bubbles as wide as the bed diameter), followed by the fast fluidisation regime where particles are entrained over the top of the bed. These regimes are schematically shown in figure 1.1.

The fluidisation behaviour of particles depends on their size and density. Small particles with a low density are more easily fluidised than large and heavy particles, as the gravity acting on the latter type is much larger. The inter-particle forces on small particles are relatively more important than the same forces acting on large particles, causing small particles to exhibit a certain (velocity) range of homogeneous expansion.

Although the basics of fluidisation are conceptually simple, the hydrodynamic behaviour of fluidised beds is extremely complex. Throughout the bed large gradients may occur in for example the solids hold-up and velocities due to bubble passage and/or clustering, making it difficult to quantitatively predict the bed behaviour. This complex behaviour has caused severe problems in the design and scale-up of these reactors in industrial practice. It is anticipated that validated CFD-models can contribute to the successful design and optimisation of these industrially relevant reactors.

1.4 CFD modelling of fluidised beds

Computational fluid dynamics (CFD) is the discipline that uses computer simulations to calculate the flow behaviour in for example a chemical reactor. Analytical solutions are often not available for these systems, and CFD simulations provide a valuable method to obtain realistic estimates of the flow behaviour. CFD models have been developed for various types of reactors, of which the gas-solid fluidised bed and gas-liquid bubble column are two important examples. In CFD models, the computational domain is usually divided into cells and discretised versions of the hydrodynamical equations are solved iteratively for each cell.

The capabilities of these models have advanced considerably in recent years and with the ever increasing computational power solutions can be generated relatively fast. Flow patterns can be calculated with greater accuracy and in more detail than before. Reactor geometries that are used are becoming more complex, and new features concerning particle growth, coalescence and break-up of bubbles and chemical reactions are included in various models. With these models the influence of several parameters on reactor behaviour can be studied in a very cost efficient way.

1.5 Multi-level modelling approach

Models of fluidised beds have been developed at several scales, differing in level of details provided in the solution and computational demands.

The largest scale model is the continuum or multi-fluid model. In this type of model both the gas and the solid phase are represented as continuous, interacting phases. Particles with different physical properties (such as diameter and density) are treated as separate phases. The volume fraction and average velocity of each phase are calculated for each computational cell by solving Navier-Stokes type of equations. Closure relations are used to describe the particle-particle interaction and distributions of e.g. particle velocities (usually a model based on the kinetic theory of granular flow) and fluid-particle interaction (usually a combination of the Ergun- and Wen and Yu-equations). Major advantage of this model is that it does not require much memory and for this reason it is in principle very well suited to simulate engineering-scale fluidised beds. Disadvantages are clearly the

large amount of assumptions made in deriving the closure relations and the relatively low level of detail in the solution: only average properties are calculated.

The discrete particle model simulates fluidised beds on a smaller scale. As the name suggests, this model uses individual particles in its calculation of the flow pattern. The coordinates and velocities of each particle are governed by Newton's laws. Interaction between particles is calculated either through a hard-sphere approach (using simple collision rules) or through a soft-sphere approach (spring-dashpot model). The gas-phase is treated as a continuum, requiring a closure relation for the gas-particle interaction. The increased level of detail is clearly an advantage of this model. Since all information is available about each individual particle, it can be used to check the assumptions made on the effective particle-particle interaction in the continuum models, or even to derive new correlations. On the other hand, the model is very demanding when it comes to both memory usage and CPU-capacity of the computer, and therefore the scale at which simulations can be conducted is limited. Even with modern computers the maximum amount of particles that can be simulated is about 10^6, which is several orders of magnitude smaller than the number of particles contained in an industrial reactor. Besides, this model also makes an assumption about the fluid-particle drag, which may influence the results if this correlation is incorrect.

At the most detailed level of description, the gas flow is described on a grid which is an order of magnitude smaller than the size of the dispersed particles. The gas-solid interaction on the surface can then be modelled by stick boundary conditions instead of effective drag laws. A particularly efficient method to compute the gas flow for these types of models is the lattice-Boltzmann method, which uses discrete time, space and velocities. Due to this discreteness the method is very fast compared to other iterative methods. However, due to the large grids (lattices) used, only small systems can be simulated. Even though the method is easily parallelised, the maximum number of particles currently lies in the order of several thousands. This makes it impossible to simulate even laboratory-size fluidised beds using lattice-Boltzmann simulations. Nonetheless, this method is the obvious choice when it comes to testing drag correlations that are used in larger scale models, or for deriving new drag correlations.

When a multi-level modelling approach is used the advantages of each model can be used to its full capacity, while minimizing the downsides. This con-

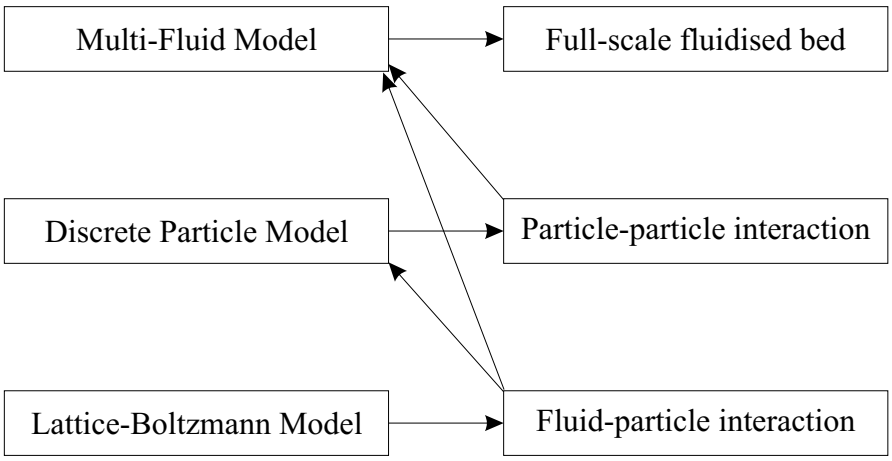

Figure 1.2: Muli-level modelling approach.

cept is shown in figure 1.2. The lattice-Boltzmann model is used to derive a correlation for the gas-particle interaction (drag force). This correlation is implemented in both the discrete particle and the multi-fluid model, to make these models as accurate as possible. The discrete particle model at its turn is used to provide information about the particle-particle interaction, such as the distribution of the velocity over the particles and the amount of energy that is lost due to collisions between particles. This is used to improve the multi-fluid model, by which simulations of engineering scale fluidised beds will be performed for design and optimisation of these reactors.

This thesis focuses on the first step in the process described above: the derivation of an accurate correlation for the drag force to improve the higher scale models.

1.6 Outline of this thesis

In chapter 2 the definitions of the variables used in this thesis are given, and an overview is presented of several drag force correlations that are known to date. Analytical calculation of the drag is possible only in the simplest cases that involve few particles and creeping flow conditions. In other systems the use of approximations and empirical relations is inevitable, which has led to a vast amount of drag relations that appeared in literature throughout the

years. The conditions for which these correlations are valid is shown, and the drag force in non-ideal systems is discussed. A new relation for the drag force on a single particle in polydisperse systems is derived from theory.

Chapter 3 describes the lattice-Boltzmann model that is used in this work and the setup of the simulations, as well as the analysis of the results. The discrete particle model that is used in the validation in chapter 6 is discussed briefly as well.

Chapter 4 deals with the results of the lattice-Boltzmann simulations for the drag force in monodisperse systems. The results are compared to literature data and equations, and a new relation is presented that fits the simulation data better than the current literature relations.

Chapter 5 presents the drag force data for particles in bi- and polydisperse systems. It is virtually impossible to measure the drag force on a single particle in such a system via direct experimentation, and therefore these simulations provide truly new data. These data are compared to the new relation for the drag on individual particles that was derived in chapter 2 and empirical relations from literature.

The new relation is validated with experiments in chapter 6. These experiments consist of pressure drop measurements over mono- and bidisperse packed beds through which various liquids were pumped at various velocities. Furthermore, this chapter shows the application of the new drag relation in simulations with the discrete particle model. The simulations are compared both qualitatively and quantitatively to experiments and discrete particle simulations using other drag relations. A last test of the new relation is the calculation of the inversion velocity in mixtures of particles that differ both in size and density.

The influence of clustering on the drag force is studied in chapter 7. The relation that is presented in chapter 4 is, like many other drag relations, derived for homogeneous systems. In practical applications however, formation of bubbles and clusters disturbs this homogeneity. The results in chapter 7 show that both the configuration and the distance of surrounding particles have a strong effect on the drag force that a particle experiences.

Chapter 2

Drag relations

Abstract

This chapter presents the current state of drag force relations. Firstly, the definitions of the variables used in this work are given, followed by an overview of the drag force correlations that are currently used in engineering applications. The overview of literature relations is by no means extensive, and is limited to the relations that are most often encountered, together with the conditions for which they are valid.

2.1 Definitions

When a fluid (i.e. a gas or a liquid) percolates through a bed filled with particles, each particle experiences two forces, namely the drag force $\mathbf{F}_d$ and a buoyancy type force $\mathbf{F}_b$, the sum of which is the total force $\mathbf{F}_{f\to s}$ that the fluid exerts on a solid particle. The reaction force from the particles on the fluid manifests itself in a pressure drop. The forces are related to the pressure drop over the system as follows:

$$-\nabla P = \frac{N}{V}\mathbf{F}_{f\to s} = -\frac{N}{V}\left(\mathbf{F}_d + \mathbf{F}_b\right) = \frac{N}{V}\left(\mathbf{F}_d - V_p \nabla P\right) \ , \tag{2.1}$$

where N is the number of particles in the system, V the system volume and V_p the volume of a single particle. Equation (2.1) can also be written as:

$$-\nabla P = \frac{1-\varepsilon}{\varepsilon}\frac{\mathbf{F}_d}{V_p} \ , \tag{2.2}$$

with ε the bed porosity, that is, the fluid volume fraction in the system (the exact definition of the porosity will be given later). It follows from equations (2.1) and (2.2) that the drag force $\mathbf{F}_d$ is related to the total fluid-particle interaction force as:

$$\mathbf{F}_{f\to s} = \frac{1}{\varepsilon}\mathbf{F}_d \ . \tag{2.3}$$

Since the buoyancy force is directly proportional to $\mathbf{F}_d$, the drag force is sometimes defined as the total force $\mathbf{F}_{f\to s}$. Much discussion in literature has been devoted to the correct definition of the drag force, as can be seen in the review article of Di Felice (1995). He makes strong arguments that favour the definition of the drag force as $\mathbf{F}_d$ rather than the total interaction force. The same choice was made by Foscolo et al. (1983). In this work, the drag force is also defined as $\mathbf{F}_d$. However, it should be noted that many authors, among others Hasimoto (1959), Sangani and Acrivos (1982), Hill et al. (2001a) and Clift et al. (1978) define the total interaction force $\mathbf{F}_{f\to s}$ as the drag force.

For comparison of drag relations from various sources it is convenient to define a dimensionless drag force F that depends only on other dimensionless parameters, namely the porosity ε and particle Reynolds number Re, where the particle Reynolds number Re is defined as

$$Re = \frac{\rho\,|\mathbf{U}|\,d}{\mu} \ , \tag{2.4}$$

with ρ the fluid density, d the particle diameter, μ the fluid viscosity and $\mathbf{U}$ the superficial slip velocity, defined as $\varepsilon(\mathbf{u}-\mathbf{v})$, where $\mathbf{u}$ represents the local fluid velocity and $\mathbf{v}$ the particle velocity.

The porosity ε of a system is the fluid volume fraction in the system:

$$\varepsilon = 1 - \phi = 1 - \frac{NV_p}{V} , \tag{2.5}$$

where ϕ is the packing fraction of solids in the system. In this work, both ε and ϕ are used to indicate the volume fraction, whatever is most convenient.

One of the few exact results for the drag force is the Stokes-Einstein relation $\mathbf{F}_{d,St} = 3\pi\mu d\mathbf{U}$ for a single particle ($\varepsilon \to 1$) in the zero Reynolds number limit. It is therefore natural to use this expression to normalise the general drag force, so the normalised drag force is defined as:

$$F(\varepsilon, Re) = \frac{|\mathbf{F}_d|}{|\mathbf{F}_{d,St}|} = \frac{|\mathbf{F}_d|}{3\pi\mu d\,|\mathbf{U}|} . \tag{2.6}$$

Note that Di Felice (1995) uses a different normalisation function, namely the drag force on a single particle, where the influence of the Reynolds number is taken into account. Hasimoto (1959), Zick and Homsy (1982), Sangani and Acrivos (1982) and Hill et al. (2001a) use the normalisation function that is used in this work, but apply it to the total force $\mathbf{F}_{f\to s}$ rather than the drag force $\mathbf{F}_d$. Consequently, their expressions for F differ a factor of ε from the normalised drag force in this thesis (see equation (2.3)).

Combining equations (2.2) and (2.6) shows that the relation between the overall pressure drop and the normalised drag force on a particle is given by:

$$\frac{\varepsilon}{1-\varepsilon}(-\nabla P) = 18\mu\mathbf{U}\frac{F}{d^2} . \tag{2.7}$$

CFD models of fluidised beds often use an inter-phase momentum transfer coefficient β to calculate the momentum flux due to gas-solid friction (see e.g. Goldschmidt, 2001a; Gidaspow and Ettehadieh, 1983; Enwald et al., 1996). The relation between this coefficient and the normalised drag force used in this work is:

$$\beta = 18\mu\varepsilon(1-\varepsilon)\frac{F}{d^2} . \tag{2.8}$$

The drag force on a single particle at arbitrary Reynolds number is traditionally described via a drag coefficient C_d, defined as:

$$F_d = C_d\left(Re\right)\frac{\pi d^2}{4}\frac{\rho U^2}{2}\ . \tag{2.9}$$

For multi-particle systems it is then assumed that the drag force can be described by equation (2.9), multiplied by a voidage function $f\left(\varepsilon\right)$ to account for the presence of neighbouring particles, viz.:

$$F_d = C_d\left(Re\right)\frac{\pi d^2}{4}\frac{\rho U^2}{2}\cdot f\left(\varepsilon\right)\ . \tag{2.10}$$

The relation between the normalised drag force used in this work and the drag coefficient C_d and voidage function $f\left(\varepsilon\right)$ is then:

$$F\left(\varepsilon, Re\right) = \frac{Re}{24}C_d\left(Re\right)\cdot f\left(\varepsilon\right)\ . \tag{2.11}$$

Note that in order to obey the Stokes-Einstein relation, the drag coefficient should obey $\lim\limits_{Re\to 0} C_d\left(Re\right) = 24/Re$.

In the literature on sedimentation of particles often a hindrance function h is used to calculate the sedimentation velocity. This function of the porosity represents a correction factor on the terminal velocity of a single particle (Masliyah, 1979). The relation to the normalised drag force in this work at low Reynolds numbers is:

$$h = \frac{\varepsilon}{F}\ . \tag{2.12}$$

At higher Reynolds numbers, when the drag on a single particle is not equal to the Stokes drag, this relation becomes:

$$h = \frac{\varepsilon F_{sp}}{F}\ , \tag{2.13}$$

where F_{sp} represents the normalised drag force on a single particle ($\varepsilon \to 1$) with equal Reynolds number.

2.1.1 Polydisperse systems

The normalised drag force F_i on a sphere i in a polydisperse system is defined analogous to equation (2.1), using the individual particle diameter d_i to determine the Stokes force:

$$F_i = \frac{|\mathbf{F}_{d,i}|}{3\pi\mu d_i \, |\mathbf{U}|} \, , \tag{2.14}$$

where d_i is the diameter of particle i.

The average drag force in a polydisperse system is related to the pressure drop in the same way as in a monodisperse system (equation (2.7)):

$$\frac{\varepsilon}{1-\varepsilon}\nabla P = -18\mu\mathbf{U}\frac{\langle F\rangle}{\langle d\rangle^2} \, , \tag{2.15}$$

where the average particle diameter $\langle d\rangle$ is given by

$$\langle d\rangle = \left(\sum_i \frac{\chi_i}{d_i}\right)^{-1} \, , \tag{2.16}$$

with $\chi_i = \phi_i/\phi$ the fraction of solids volume occupied by particles of type i and the overall volume fraction of particles of type i, ϕ_i, defined as:

$$\phi_i = \frac{N_i V_{p,i}}{V_{tot}} \, . \tag{2.17}$$

The total solids volume fraction is equal to $\phi = \sum \phi_i$ and the porosity again equals $\varepsilon = 1 - \phi$. The average drag force in equation (2.15) is defined as

$$\langle F\rangle = \sum_i \frac{\chi_i}{y_i^2} F_i \, . \tag{2.18}$$

where y_i represents the ratio of the diameter of type i to the average diameter, $d_i/\langle d\rangle$.

2.2 General equations

To calculate the drag force exerted on a particle, knowledge about the flow profile surrounding this particle is required. The drag force can then be

obtained by integration of the stress tensor over the particle surface. The flow around the particle obeys the Navier-Stokes equations, which for the case of a fluid interacting with a solid phase are given by:

Continuity equation:

$$\frac{\partial \rho}{\partial t} + (\nabla \cdot \rho \mathbf{u}) = 0 \, . \tag{2.19}$$

Momentum equation:

$$\frac{\partial (\rho \mathbf{u})}{\partial t} + (\nabla \cdot \rho \mathbf{u} u) = -\nabla P - \beta \Delta \mathbf{u} - (\nabla \cdot \tau) + \rho \mathbf{g} \, . \tag{2.20}$$

where P is the pressure, τ the stress tensor of the fluid and β the momentum exchange coefficient, which is directly related to the drag force and is defined in equation (2.8).

In very simple cases these equations can be solved analytically. However, in most cases approximations are made or the drag force is determined empirically, as will become clear in the following sections.

2.3 Single particle

As discussed in section 2.1, when a single spherical particle moves through a fluid, the drag force on this particle is given by the Stokes-Einstein drag in the limit of $Re \to 0$, so that the normalised drag force in this case is obviously equal to one. The Stokes equation is only valid in the zero Reynolds number limit. When the Reynolds number increases the (normalised) drag increases as well, as the form drag starts to play a role. Various authors have attempted to give an analytical solution for the drag on a single particle at higher Reynolds numbers, as shown in the review work by Clift et al. (1978). The first term in these approximations was first found by Oseen and is equal to:

$$F(1, Re) = 1 + \frac{3}{16} Re \, . \tag{2.21}$$

However, as Clift et al. (1978) point out, all of the solutions deviate markedly from experimental data when $Re > 3$ (at most). Therefore, they concluded that these analytical solutions have little value for $Re > 1$. Beyond this

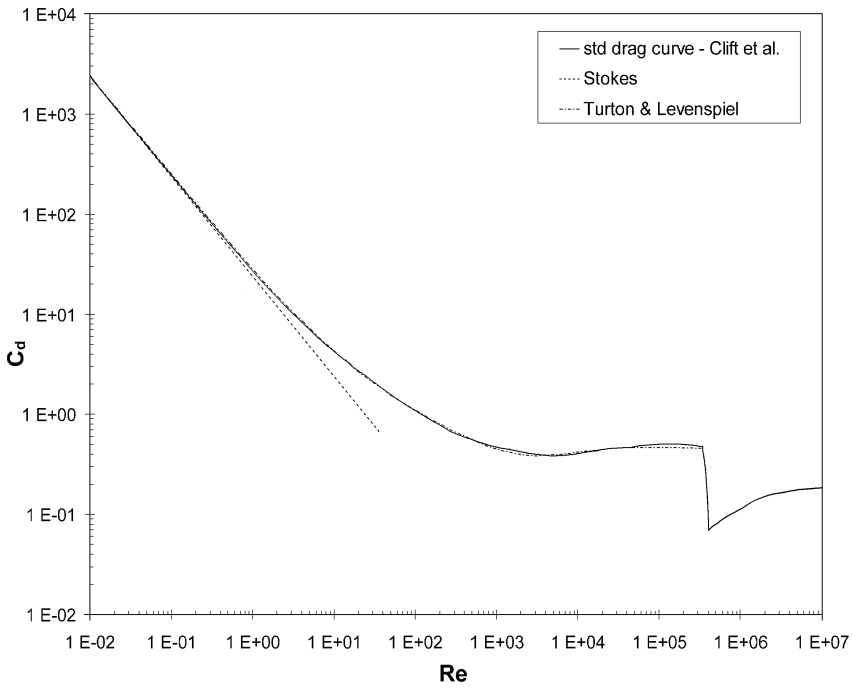

Figure 2.1: Drag force on a single particle.

value, empirical equations should be used, based on e.g. experimental data and/or numerical solutions. The standard drag curve for a single particle as proposed by Clift et al. (1978) is shown in figure 2.1. In this figure the drag coefficient C_d as defined in equation (2.9) is shown as a function of the Reynolds number. At low Reynolds numbers the Stokes-Einstein equation forms a good approximation of the drag force. At $Re > 1000$ the drag coefficient assumes an almost constant value. At $Re > 3 \cdot 10^5$ a sudden drop in the drag coefficient occurs, which is called the critical transition. The subcritical range is by far the most interesting range in chemical engineering, and this is also the range where most research was done.

Schiller and Naumann (1933) found that the normalised drag force on a

single particle in this range is equal to:

$$F\left(1, Re\right) = \begin{cases} 1 + 0.15Re^{0.687} & Re < 1000 \\ 0.44\frac{Re}{24} & Re > 1000 \end{cases} \tag{2.22}$$

Obviously, the limiting value for F in case of $Re = 0$ is equal to the Stokes drag ($F = 1$).

Clift et al. (1978) argue that the best representation of the drag force is obtained when the entire range of Re is split into ten subintervals: seven intervals in the subcritical regime, one for the transition and two in the supercritical regime. For each subinterval a different equation is used to calculate the drag force, which makes their drag correlation very complex. The drag curve shown in figure 2.1 was based on these equations, which are not shown here. Turton and Levenspiel (1986) found that an equation with only five fit-parameters,

$$F\left(1, Re\right) = \left(1 + 0.173Re^{0.657}\right) + \frac{Re}{24}\frac{0.413}{\left(1 + 16300Re^{-1.09}\right)}\ , \tag{2.23}$$

matches the experimental data in the subcritical regime just as well as the set of seven equations - with no less than eighteen fitparameters - used by Clift et al. (see also figure 2.1).

2.4 Regular arrays of monodisperse spheres

If more than one particle is present, the flow around each particle is influenced by the presence of the other particles, and thus the drag force is influenced as well. The simplest case of a multi-particle system is an array of spherical particles in the limit of zero Reynolds number, where the flow pattern is very well-defined and periodic, leading to an equal drag force on each particle.

Hasimoto (1959) was one of the first people to tackle this problem. Using Fourier series he obtained spatially periodic fundamental solutions of the Stokes equations of motion. The results for simple cubic (S.C.), body centred

cubic (B.C.C.) and face centred cubic (F.C.C.) lattices are as follows:

$$F = \begin{cases} \varepsilon \left(1 - 1.7601\phi^{1/3} + \phi - 1.5593\phi^2 + O\left(\phi^{8/3}\right)\right)^{-1} & \text{S.C.} \\ \varepsilon \left(1 - 1.7918\phi^{1/3} + \phi - 0.3292\phi^2 + O\left(\phi^{8/3}\right)\right)^{-1} & \text{B.C.C.} \\ \varepsilon \left(1 - 1.7917\phi^{1/3} + \phi - 0.3020\phi^2 + O\left(\phi^{8/3}\right)\right)^{-1} & \text{F.C.C.} \end{cases} \quad (2.24)$$

Since only terms up to order ϕ^2 are taken into account, the validity of these equations is limited to low packing fractions ($\phi < 0.1$). Sangani and Acrivos (1982) modified Hasimoto's method and calculated the drag force in cubic arrays over the complete porosity range. Converged results for several values of ϕ over the whole range are listed in their article. Their extended equation for simple cubic lattices is given by:

$$F = \varepsilon \Big(1 - 1.7601\phi^{1/3} + \phi - 1.5593\phi^2 + 3.9799\phi^{8/3} - 3.0734\phi^{10/3} + O\left(\phi^{11/3}\right)\Big)^{-1} , \quad (2.25)$$

which is very accurate for packing fractions up to $\phi = 0.2$ and fairly accurate beyond this value. They also provide coefficients for all three lattices for a series expansion up to order ϕ^{10}, which provides accurate results up to $\phi = 0.6 \cdot \phi_{max}$, and for BCC-lattices at even higher values.

Zick and Homsy (1982) solved an integral equation over the surface of the spheres to obtain the drag force as a function of porosity. Their results agree well with those obtained by Sangani and Acrivos (1982).

Hill et al. (2001a) used lattice-Boltzmann simulations to study the drag force in arrays of spheres. The results agree very well with the results of Zick and Homsy (1982) and Sangani and Acrivos (1982). The effect of increasing Reynolds numbers on the drag force in arrays of spheres was also studied using lattice-Boltzmann simulations. Hill et al. (2001b) found that for low Reynolds numbers, the drag increases quadratically with Reynolds. For $Re > 40$ they found a linear dependence on the Reynolds number. At high Reynolds numbers the drag was found to depend on the direction of the flow as well, which was not observed for low Reynolds numbers.

2.5 Random arrays of monodisperse spheres

2.5.1 Low Reynolds numbers

There are two approaches for evaluating the drag force in random multi-particle systems at low Reynolds numbers. The first one views the porous medium as a bundle of tubes and calculates the drag force based on the analogy with the drag force of a fluid flowing through a tube. Important parameters are the width of the pores (tubes) and the path length of the fluid. This approach works quite well in dense systems. In more dilute systems no separate channels can be distinguished, so in these cases the system is usually viewed as a collection of submerged objects and the drag relations are usually based on the drag force on a single particle, taking into account some correction for the presence of other particles.

Batchelor (1972) followed the submerged particle approach. He calculated the influence of the interaction between particles in dilute random systems on the drag force, which led to the following equation:

$$F(\varepsilon, 0) = \frac{\varepsilon}{1 - 6.55\,(1-\varepsilon)}\ , \tag{2.26}$$

which is valid at very low particle volume fractions (note that the equation has a singular point at $\varepsilon \approx 0.853$ and even shows negative drag forces at lower porosities) and in the absence of inter-particle forces.

The Kozeny-Carman equation is a typical example of an equation that views the porous medium as a collection of channels. At low Reynolds numbers, the relation between the fluid flow through a dense porous medium and the pressure drop over this system can be described in general by the Darcy equation:

$$-\nabla P = \frac{1}{\kappa}\mu\mathbf{U}\ . \tag{2.27}$$

In this equation, κ is the permeability of the medium. The permeability depends, in principle, on the detailed geometrical structure of the medium, however in practice it is well-described by the Kozeny-Carman equation (Carman, 1937):

$$\kappa = \frac{\varepsilon r_h^2}{k}\ , \tag{2.28}$$

where r_h is the hydraulic radius and k is a constant. The hydraulic radius is defined as the ratio of the pore volume to the surface area of the medium. For a packing of spheres with diameter d the hydraulic radius is equal to:

$$r_h = \frac{d}{6}\frac{\varepsilon}{(1-\varepsilon)} \tag{2.29}$$

Substituting equations (2.28) and (2.29) in equation (2.27) gives the following result for the pressure drop over a porous system:

$$-\nabla P = 36k\frac{(1-\varepsilon)^2}{\varepsilon^3}\frac{\mu \mathbf{U}}{d^2} \tag{2.30}$$

In terms of the normalised drag force on a single sphere, the Kozeny-Carman equation predicts that (see equation (2.6)):

$$F(\varepsilon, 0) = 2k\frac{(1-\varepsilon)}{\varepsilon^2} \tag{2.31}$$

The Kozeny-constant k was experimentally found to be close to 5 (Carman, 1937). Fand et al. (1987) measured an average value of $k = 5.34$.

The Kozeny-Carman approximation provides a reasonably accurate description of fluid-solid drag. However, there are some limitations. Firstly, the Kozeny-Carman equation was derived for dense porous systems. It is obviously not valid in dilute systems, since the normalised drag force approaches $F = 0$ for $\varepsilon \to 1$, where its limit should be the Stokes drag $F = 1$. Secondly, the equation is based on the assumption that all pores have more or less equal sizes. If this is not true, a lower value for the Kozeny-constant will be found. Thirdly, it is assumed that the system is isotropic: the direction of the flow should not make a difference for the permeability of a system. If there are more pores in one direction than in the other direction or if there is a variation in pore size between various directions, the Kozeny constant will depend on the direction of the flow (Thies-Weesie and Philipse, 1994). Finally, the validity of the Kozeny-Carman equation and its derivatives is limited to fluid flow in the limit of zero Reynolds number.

2.5.2 Intermediate and higher Reynolds numbers

At higher Reynolds numbers no theoretical derivation of the drag force is available. All results are empirical, obtained from measurement of either the pressure drop or sedimentation velocity.

One of the most often used equations for the pressure drop in chemical engineering is the Ergun-equation, $-\nabla P = 150\frac{(1-\varepsilon)^2}{\varepsilon^3}\frac{\mu \mathbf{U}}{d^2} + 1.75\frac{(1-\varepsilon)}{\varepsilon^3}\frac{\rho \mathbf{U}^2}{d}$, (Ergun, 1952). For the normalised drag force this corresponds to:

$$F = \frac{150}{18}\frac{(1-\varepsilon)}{\varepsilon^2} + 1.75\frac{Re}{18\varepsilon^2} \ , \tag{2.32}$$

where the Kozeny-Carman equation is recognised in the first term (viscous forces), and a Reynolds-dependent term was added to account for the inertial forces. As discussed in the previous section, the Kozeny-Carman equation is not valid in high-porosity systems, and so the Ergun equation cannot be used for these systems either. Although Ergun used only a limited porosity range in his experiments ($\varepsilon = 0.43 - 0.54$), the equation is currently used for porosities up to 0.8 (see e.g. Enwald et al., 1996). Furthermore, it should be noted that Ergun used crushed porous material for his experiments with a range of sizes. As will become clear in chapter 5, this size range results in a lower drag force compared to systems where perfect monodisperse spheres are used.

Ergun assumes that the total drag force is the sum of the viscous and inertial forces. Other authors have found relationships of the type

$$F_d = (F_v^\alpha + F_i^\alpha)^{1/\alpha} \ , \tag{2.33}$$

where F_v is the viscous drag and F_i the drag due to inertial effects, and α is either a constant or a function of the porosity (see e.g. Gibilaro et al., 1986; Di Felice, 1995).

Fand et al. (1987) concluded from their experiments in packed beds that three main regimes exist in fluid flow through packed beds. The first regime at low Reynolds numbers ($Re < 2.3$) is the Darcy flow, where the drag (and thus pressure drop) are given by the Kozeny-Carman equation mentioned above (equation (2.31)). The Kozeny-constant is equal to 5.34 according to their work. Ergun type equations apply at higher Reynolds numbers:

$$F = \frac{A}{18}\frac{(1-\varepsilon)}{\varepsilon^2} + B\frac{Re}{18\varepsilon^2} \ . \tag{2.34}$$

In the Forchheimer-regime, $5 < Re < 80$, the coefficients in equation (2.34) take the values $A = 182$ and $B = 1.92$. At higher Reynolds numbers turbulence starts developing in the porous system, and for $Re > 120$ all data again fall onto a straight line, with the coefficients $A = 225$ and $B = 1.61$.

In between the three main regimes transition regimes are found where the regime gradually changes. The experiments of Fand et al. (1987) were conducted in random dense packed beds, with porosities varying from $0.342 - 0.360$. The validity of the equations beyond these values was not tested, although their formulation suggests they are valid over a large range of porosities. The maximum Reynolds number for which experiments were done was 408.

An equation of a completely different type that has found widespread use in CFD-modelling is the Wen and Yu-equation (Wen and Yu, 1966):

$$F = \frac{Re}{24} C_d\left(Re\right) \varepsilon^{-3.65} \,, \tag{2.35}$$

with the drag coefficient $C_d\left(Re\right)$ given by:

$$C_d\left(Re\right) = \begin{cases} \frac{24}{Re}\left(1 + 0.15 Re^{0.687}\right) & Re < 1000 \\ 0.44 & Re > 1000 \end{cases} \tag{2.36}$$

In the limit of $\varepsilon \to 1$ (single particle) F approaches the Schiller and Naumann-drag relation. When other particles are present the movement is hindered, represented by the term $\varepsilon^{-3.65}$. In CFD-models, this equation is often encountered to describe the drag in dilute regions ($\varepsilon > 0.8$), where the Ergun-equation is not valid (see e.g. Enwald et al., 1996). Wen and Yu based their equation on previous sedimentation research by Richardson and Zaki (1954), who stated that

$$\frac{U}{U_t} = \varepsilon^n \,, \tag{2.37}$$

with U the 'superficial' sedimentation velocity of the assembly of particles (that is, the velocity multiplied by the porosity ε) and U_t the terminal velocity of a single particle. The power n was found to be a function of the Reynolds number:

$$n = \begin{cases} 4.65 & Re < 0.2 \\ 4.35 Re^{-0.03} & 0.2 < Re < 1 \\ 4.45 Re^{-0.1} & 1 < Re < 500 \\ 2.39 & Re > 500 \end{cases}$$

In the original work n was a function of the particle to tube diameter ratio d/D as well, but this dependency was not confirmed in later research (Di Felice, 1995). For low Reynolds numbers, when $F \sim U$, equation (2.37) is similar to:

$$F = \frac{Re}{24} C_d \varepsilon^{-(n-1)} \,, \tag{2.38}$$

whereas for high Reynolds numbers, when $F \sim U^2$, equation (2.37) is similar to

$$F = \frac{Re}{24} C_d \varepsilon^{-(2n-1)} \,. \tag{2.39}$$

Consequently, for $Re < 0.2$ we get $F \sim \varepsilon^{-3.65}$ and for $Re > 500$ we find $F \sim \varepsilon^{-3.78}$. Therefore, in the Wen and Yu equation a constant power -3.65 is assumed in the calculation of the drag force over the entire Reynolds number range. Di Felice (1994) noticed that the power was weakly dependent on the Reynolds number and proposed the relation

$$F = \frac{Re}{24} C_d \left(Re\right) \varepsilon^{p} \,, \tag{2.40}$$

with p given by

$$p = 3.7 - 0.65 \exp\left\{ \frac{-\left(1.5 - \log\left(Re\right)\right)^2}{2} \right\} \,. \tag{2.41}$$

This approach is particularly popular in sedimentation literature and liquid fluidisation. Many researchers proposed relations for C_d and n or p as a function of Reynolds or Galileo numbers. For an overview of various relations see Di Felice (1995).

Hill et al. (2001b) used lattice-Boltzmann simulations to study the drag force in porous systems. Equation (2.42) shows their results:

$$F = F_0 + \frac{1}{2} F_3 Re \,, \tag{2.42}$$

with

$$F_0 = \begin{cases} (1-\phi)\, \frac{1+\left(3/\sqrt{2}\right)\sqrt{\phi}+(135/64)\phi\ln\phi+16.14\phi}{1+0.681\phi-8.48\phi^2+8.16\phi^3} & \phi < 0.4 \\ 10\frac{\phi}{(1-\phi)^2} & \phi > 0.4 \end{cases}$$

$$F_3 = 0.0673 + 0.212\phi + \frac{0.0232}{(1-\phi)^5} \ ,$$

where it should be remembered that $\phi = 1 - \varepsilon$. F_0 represents the drag force in the limit of $Re = 0$. In this case the Kozeny-Carman equation is used for dense packings, while the drag force in more dilute systems is derived from the equation that was proposed by Kim and Russell (1985). Hill et al. (2001b) further report that at very low Reynolds numbers ($Re < 1$) the drag force is quadratic in the Reynolds number: $F = F_0 + (1/4)\, F_1 Re^2$. Although according to their work equation (2.42) is valid when $Re > 40$, the differences with the quadratic equation in the low Reynolds number regime are very small, and the limit for $Re = 0$ is the same. Therefore, for practical purposes equation (2.42) can be used over the entire range of Reynolds numbers, which has the advantage that there is no discontinuity in the representation. The equation above was derived from simulations up to $Re = 150$.

2.6 Random bi- and polydisperse systems

2.6.1 Overall pressure drop

The Kozeny-Carman equation (equation (2.30)) is, in principle, valid for all random porous media, independent of the details of the geometry and hence of the particle shapes and sizes, provided the system is dense and homogeneous. The correct expression for the hydraulic radius in a mixture of spheres is given by:

$$r_h = \frac{\langle d \rangle}{6} \frac{\varepsilon}{(1-\varepsilon)} \ , \tag{2.43}$$

with the average diameter $\langle d \rangle$ defined by equation (2.16). By comparing equation (2.43) to equation (2.29) we find that the pressure drop over the mixed system is given by the same equation as for monodisperse systems (equation (2.30)), where the diameter is replaced by the average diameter of the mixture. The Kozeny-constant k is independent of the details of the porous medium. For binary systems, Thies-Weesie and Philipse (1994) found a value for the Kozeny-constant of $k = 3.92$ in their experiments. From lattice-Boltzmann simulations of similar systems Maier et al. (1999) arrived at a value $k \approx 5.0$. The difference is probably due to the sintering necessary to measure the porosity in the experiments. The measured

porosity is slightly lower than the actual porosity during the experiments, resulting in a lower experimental value for k.

As was shown by Fand et al. (1987), the same method of replacing d by $\langle d \rangle$ is also valid at higher Reynolds numbers, where other drag relations apply.

2.6.2 Drag force on individual particles

In monodisperse media, the drag force on a single particle is (more or less) equal to $1/N$ times the total drag force in the system. For bi- and polydisperse systems this is not necessarily true. Unfortunately, up to now it has not been possible to measure the drag on a single individual particle in a bidisperse system. Although several methods have been developed to measure the drag force on a particle directly (see e.g. Liang et al., 1996; Katoshevski et al., 2001; Zhu et al., 2003), these are all limited to single particles or particles that are surrounded by only a few others, which cannot be representative of a bi- or polydisperse system. A fair amount of research was done on sedimentation of bi- and polydisperse mixtures (see e.g. Mirza and Richardson, 1979; Biesheuvel et al., 2001). However, most of this data is concerned with the sedimentation velocities of each particle species rather than with the drag force and thus provides only indirect information on the drag force. It should be noted that in most cases assumptions concerning the local porosity and composition of the mixture are made that even further question the validity of the model. As will be shown later, it is this individual drag that turns out to be very different from what is commonly accepted.

Batchelor (1982) derived an equation for the falling velocity of spheres in dilute polydisperse suspensions at low Reynolds numbers based on pair interactions. From his work it follows that the normalised drag force in dilute systems is equal to

$$F_i = \frac{\varepsilon}{1 + \sum_j S_{ij}\phi_j} \ . \tag{2.44}$$

It was shown before that the coefficient S_{ij} in a monodisperse system in the absence of inter-particle forces is equal to -6.55 (see equation (2.26)). In polydisperse systems S_{ii} assumes the same value. The other coefficients depend on the diameter and density ratios, and are not symmetrical, that is $S_{ij} \neq S_{ji}$ (Batchelor and Wen, 1982).

The approach that is most often encountered in CFD-modelling to calculate the drag on a single particle is to assume that a particle experiences the same normalised drag force as it would in a monodisperse system of equal porosity, with the average Reynolds number Re replaced by the individual value $Re_i = \rho d_i U/\mu$ (see e.g. Hoomans, 1999). However, this approach usually results in an incorrect overall pressure drop, as is easily demonstrated for $Re = 0$ using the Kozeny-Carman equation. Assuming an equal normalised drag force of $F_i = 2k(1-\varepsilon)/\varepsilon^2$ for all particles adds up to an overall pressure drop equal to:

$$-\nabla P = \frac{1}{\varepsilon V}\sum_i N_i F_{d,i} = 36k\mu\mathbf{U}\frac{(1-\varepsilon)^2}{\varepsilon^3}\frac{\sum\limits_i N_i d_i}{\sum\limits_i N_i d_i^3}\ , \tag{2.45}$$

whereas the value for the pressure drop in the Kozeny-Carman approximation is given by (see equations (2.27), (2.28) and (2.43)):

$$-\nabla P = 36k\mu\mathbf{U}\frac{(1-\varepsilon)^2}{\varepsilon^3}\frac{1}{\langle d\rangle^2} = 36k\mu\mathbf{U}\frac{(1-\varepsilon)^2}{\varepsilon^3}\left(\frac{\sum\limits_i N_i d_i^2}{\sum\limits_i N_i d_i^3}\right)^2\ . \tag{2.46}$$

Syamlal (1985) adjusted the Ergun and Wen and Yu-equations to polydisperse systems as follows:

$$F_i = \frac{150}{18}\frac{\phi_i}{\varepsilon^2} + 1.75\frac{Re}{18\varepsilon^2}\frac{\phi_i}{1-\varepsilon}\ , \tag{2.47}$$

$$F_i = \frac{Re}{24}C_d\frac{\phi_i}{1-\varepsilon}\cdot f(\varepsilon)\ . \tag{2.48}$$

However, this approach does not predict the Kozeny-Carman pressure drop either.

A new approach that does result in the average drag force according to the Kozeny-Carman equation (where d is replaced by $\langle d\rangle$) will be presented in section 2.6.3.

Patwardhan and Tien (1985) assumed that the porosity that a particle experiences is mainly determined by the ratio of the average pore size to its diameter. This means that in a binary mixture the smaller particles will experience a larger porosity, as the pores are large compared to their diameter. The larger particles however will experience a relatively low porosity

since the ratio of the pore size to the particle diameter is much smaller. The average space available for each particle is represented by a layer of thickness δ surrounding this particle. For monodisperse systems this δ is evaluated from

$$\frac{1}{\phi} = \left(1 + \frac{\delta}{d}\right)^3 , \tag{2.49}$$

which is equivalent to

$$\delta = d\left(\phi^{-1/3} - 1\right) . \tag{2.50}$$

The effective porosity for type i in a polydisperse suspension is evaluated as:

$$\frac{1}{\phi_i} = \left(1 + \frac{\delta}{d_i}\right)^3 . \tag{2.51}$$

This effective porosity is used in the calculation of the drag force on a particle, for which any drag relation may be used. The main difficulty of this approach lies in evaluating δ in a mixture. Patwardhan and Tien approximate this by:

$$\delta = d_{avg}\left(\phi^{-1/3} - 1\right); , \tag{2.52}$$

using $d_{avg} = \sum_i \chi_i d_i$. However, this choice for d_{avg} seems to be rather ad hoc, and no justification is given. A significant improvement is achieved by using $d_{avg} = \langle d \rangle$ as defined in equation (2.16). The difference is especially noteworthy in the case of high packing fractions and/or extreme diameter ratios. Note that with a little more work the third order polynomial may also be solved exactly.

Koo and Sangani (2002) proposed various adjustments to the effective medium theory that extend its validity to bidisperse systems. This kind of theories calculates the effective properties of suspensions by solving averaged equations taking into account some of the interactions between particles. The three models differ in choice of the exclusion radius R of the particles and the properties used for the fluid within this radius. The model that gives the best results for monodisperse systems is limited to low volume fractions of the smaller particles in binary systems. Koo and Sangani (2002) tested the validity of their theories with simulations using a multipole expansion

method. The drag forces were calculated in mixtures with two sizes ratios ($d_1/d_2 = 0.5$ and $d_1/d_2 = 0.7$) at two porosities ($\varepsilon = 0.65$ and $\varepsilon = 0.90$). To our knowledge, this is the only available data in literature on the drag force on individual particles in bidisperse systems. The predictions from the effective medium theory were a good approximation of the simulation values at low packing fractions ($\phi = 0.1$), whereas for higher packing fractions ($\phi = 0.35$) the drag force was overestimated by 7% on average.

2.6.3 A new drag relation for polydisperse systems

In the framework of the Kozeny-Carman approximation, the correct overall pressure drop is found when one of the following expressions is used for the drag force on individual particles:

$$F_i = y_i F_{mono} \qquad \text{or} \qquad F_i = y_i^2 F_{mono} \,,$$

where $y_i = d_i/\langle d \rangle$ and F_{mono} stands for the normalised drag force in a monodisperse system of equal porosity. The most general form for F_i that saisfies the Kozeny-Carman expression for the pressure drop is then:

$$F_i = \left((1-p)\, y_i + p y_i^2\right) F_{mono} \,, \tag{2.53}$$

with p a yet unknown variable, which may be determined from the limit $d_i/d_j \to 0$, while ϕ_i and ϕ are kept constant. In that limit $y_i = \chi_i$, and therefore equation (2.53) reduces to

$$\lim_{d_i/d_j \to 0} F_i = \chi_i \left(1 - p + p\chi_i\right) F_{mono} \,. \tag{2.54}$$

The same system may also be considered as a system where all particles except type i are infinitely large. The drag force on particles of type i should thus be equal to the drag force in a monodisperse system consisting of the same particles, with an effective volume of $V - \sum_{j \neq i} N_j V_j$. This can be shown to be equal to:

$$\lim_{d_i/d_j \to 0} F_i = \chi_i \left(1 - \phi + \phi\chi_i\right) F_{mono} \,. \tag{2.55}$$

Comparing to equation (2.53) gives $p = \phi$. Thus, the drag force on a single particle can be represented by:

$$F_i = \left((1-\phi)\, y_i + \phi y_i^2\right) F_{mono} \,. \tag{2.56}$$

This equation will be compared to our results from lattice-Boltzmann simulations in chapter 5.

Chapter 3

Numerical methods

Abstract

This chapter describes the numerical methods that are used in this work. The drag force simulations are performed with a lattice-Boltzmann model, which describes the fluid phase with discrete time, space and velocities. The solid particles are mapped on this grid, and the drag force is measured from the momentum change on the boundary nodes. The simulation setup and analysis of the results are explained here as well.

The discrete particle model, which is used in the validation of the drag relation, models the gas phase as a continuum and requires a closure relation for the gas-particle interaction. For the particle-particle and/or particle-wall interaction a collision model is invoked which is based either on the hard sphere or on the soft sphere approach.

3.1 Introduction

The enormous increase in computer capacities in the last decades has led to a strong development in the field of Computational Fluid Dynamics. Several models were developed for various systems (e.g. liquid-gas or gas-solid) at different levels of detail and accuracy. This thesis focuses on the modelling of fluid-solid systems. For the largest scale models, a number of closures are required to account for the effective solid-solid and fluid-solid interaction (drag force), since even with present-day computers memory and processor speed are far from sufficient to obtain results with greater detail in a reasonable amount of time. These effective interactions are often based on theoretical or empirical relations from literature, but correlations may also be derived from more detailed computer simulations. In this thesis a new correlation for the particle-fluid interaction is derived from lattice-Boltzmann simulations. This model is based on a discretised version of the Boltzmann-equation and is particularly suited ro resolve the fluid flow on a scale smaller than the particle size, thus providing accurate information on the interaction force. The lattice-Boltzmann model used in this work is described in section 3.2.

The drag relation that was derived from the lattice-Boltzmann simulation results was tested in discrete particle model simulations. Since the fluid phase in this model is calculated at a resolution greater than the particle sizes, a closure relation is necessary to calculate the interaction between the phases. The discrete particle model is described in section 3.5.

3.2 Lattice-Boltzmann method

The lattice-Boltzmann method originates from lattice-gas cellular automata, a simulation method that uses discrete time, space, velocity and mass. It is faster and uses less memory than e.g. molecular dynamics simulations, whereas results with respect to the large scale fluid motion can be very similar. In lattice-gas simulations fluid particles move on a fixed lattice. The fluid particles can only be present at lattice sites, and velocities are discrete in such a way that each particle moves from grid point to grid point in exactly one time step. Two particles at the same grid point are not allowed to have equal velocities. Each simulation time step consists of two parts: propagation and collision. The propagation to the next grid

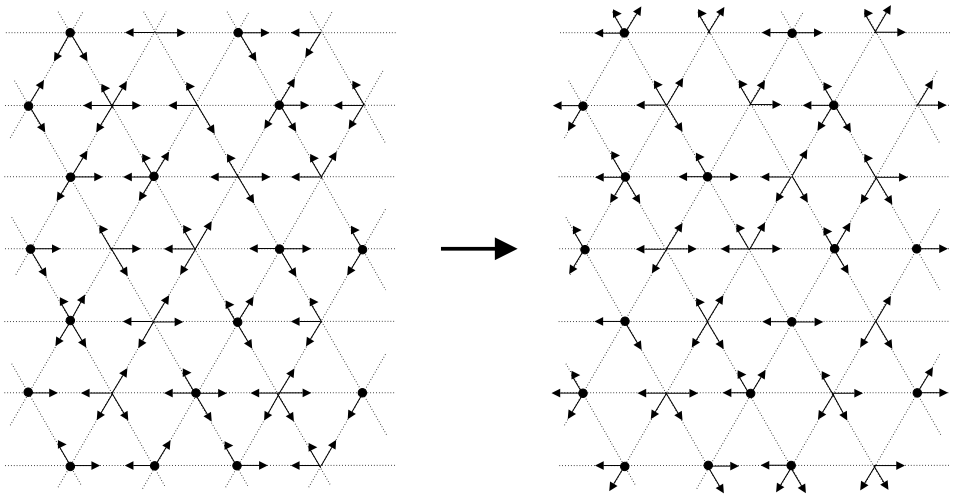

Figure 3.1: Propagation step in lattice-gas cellular automata.

point is shown in figure 3.1. When a particle arrives at the new grid point it collides with particles coming from other directions, thereby preserving total mass and momentum. An example is shown in figure 3.2. If there are several possibilities to preserve mass and momentum starting from the same initial configuration, a choice between the possibilities can be made either at random or according to a predetermined scheme.

The lattice-gas method is a very efficient way to simulate hydrodynamics, and - because of its discreteness - unconditionally stable. However, due to the same discreteness it also suffers from statistical noise, so massive averaging in time and/or space, as well as ensemble averaging, is required before reliable results are obtained. To overcome this problem, the lattice-Boltzmann method was introduced by McNamara and Zanetti (1988). Instead of discrete particles this method uses an ensemble averaged particle occupation number, which is equivalent to the single-particle distribution

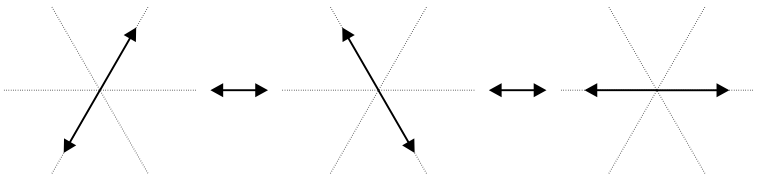

Figure 3.2: Collision step in lattice-gas cellular automata.

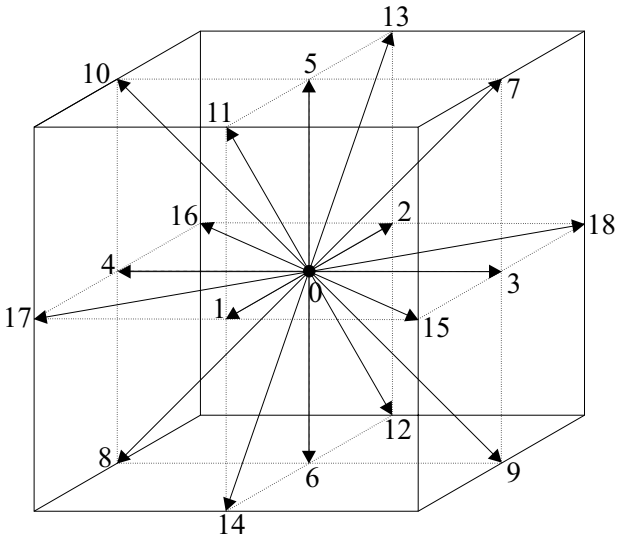

Figure 3.3: D3Q19-lattice used in this work.

function which appears in the Boltzmann-equation (mass is no longer a discrete variable). The ensemble averaged equations of motion of the discrete lattice gas method turn out to yield a discretised version of the Boltzmann equation.

The model, and also the code, that is used in this work was developed by Ladd (1994a), and is briefly described below. It uses a nineteen velocity cubical grid (D3Q19, see the classification of Qian et al. (1992)), as shown in figure 3.3. The nineteen velocities are formed by the (100)- and (110)-directions of the cube, and particles at rest (zero velocity). The magnitudes of the velocities are thus:

- $c = 1$ for the (100)-directions
- $c = \sqrt{2}$ for the (110)-directions
- $c = 0$ for the rest particles.

The update of the discretised velocity distribution n can be represented as follows:

$$n_i\left(\mathbf{r} + \mathbf{c}_i, t + 1\right) = n_i\left(\mathbf{r}, t\right) + \Delta_i\left(n\left(\mathbf{r}, t\right)\right) \ . \tag{3.1}$$

Equation (3.1) is the basic equation of the lattice-Boltzmann method. The second term on the right hand side represents the change in the distribution function due to collision. The post-collision distribution is then shifted to the next lattice site in the direction of the velocity c_i. Each time step thus consists of a propagation step and a collision (or relaxation) step, similar to the lattice-gas cellular automata. The collision step will be explained in more detail in section 3.2.2.

The hydrodynamic fields (density ρ, momentum $\mathbf{j}$ and stress $\mathbf{\Pi}$) are calculated from the moments of the velocity distribution:

$$\rho = \sum_i n_i \ , \tag{3.2}$$

$$\mathbf{j} = \sum_i n_i \mathbf{c}_i \ , \tag{3.3}$$

$$\mathbf{\Pi} = \sum_i n_i \mathbf{c}_i \mathbf{c}_i \ . \tag{3.4}$$

3.2.1 Equilibrium distribution

In case of equilibrium the velocity distribution should not change during a collision. The moments of the equilibrium distribution function n_i^{eq} define the equilibrium density, momentum and momentum flux:

$$\rho^{eq} = \sum_i n_i^{eq} \ , \tag{3.5}$$

$$\mathbf{j}^{eq} = \sum_i n_i^{eq} \mathbf{c}_i = \rho \mathbf{u} \ , \tag{3.6}$$

$$\mathbf{\Pi}^{eq} = \sum_i n_i^{eq} \mathbf{c}_i \mathbf{c}_i = \rho c_s^2 \mathbf{I} + \rho \mathbf{u}\mathbf{u} \ . \tag{3.7}$$

In these equations $\mathbf{u}$ is the local gas velocity, c_s is the speed of sound and ρc_s^2 is equal to the pressure. The value for the speed of sound is restricted to prevent the simulations from becoming unstable, where an optimum value is $c_s^2 = 1/3$, which is used in this work. The equilibrium distribution for the D3Q19-lattice is (Ladd and Verberg, 2001):

$$n_i^{eq} = a^{c_i} \rho \left[1 + \frac{\mathbf{u} \cdot \mathbf{c}_i}{c_s^2} + \frac{(\mathbf{u} \cdot \mathbf{c}_i)^2}{2c_s^4} - \frac{u^2}{2c_s^2} \right] \ , \tag{3.8}$$

$$a^0 = \frac{1}{3}, \qquad a^1 = \frac{1}{18}, \qquad a^{\sqrt{2}} = \frac{1}{36} \ .$$

3.2.2 Relaxation

When the fluid arrives at the new site after propagation, a collision occurs, which is represented by a relaxation towards the equilibrium distribution. The speed at which this relaxation occurs is a measure for the viscosity. During the collision the total mass and momentum should be preserved for each lattice site.

There are two ways of programming the collision step. The first possibility is by using the Bhatnagar-Gross-Krook approach (Qian et al., 1992; Bhatnagar et al., 1954). This is a simple method to achieve relaxation towards equilibrium as shown in the following equation:

$$n_i' = n_i - \frac{1}{\tau}\left(n_i - n_i^{eq}\right) \ , \tag{3.9}$$

where n_i' is the distribution function immediately after the collision and n_i the distribution just before collision. In this approach the relaxation time τ is a measure for viscosity.

The second possibility, which is used in this work, is to use the stress tensor update (Ladd, 1994a). This method has the advantage that it is possible to choose a bulk viscosity in the simulation as well. The relaxation of the stress tensor is as follows:

$$\Pi'_{\alpha\beta} = \Pi^{eq}_{\alpha\beta} + (1+\lambda)\left(\overline{\Pi}_{\alpha\beta} - \overline{\Pi}^{eq}_{\alpha\beta}\right) + \frac{1}{3}(1+\lambda_B)\left(\Pi_{\gamma\gamma} - \Pi^{eq}_{\gamma\gamma}\right)\delta_{\alpha\beta} \ . \tag{3.10}$$

In this equation $\mathbf{\Pi}'$ is the stress tensor after collision, $\mathbf{\Pi}$ is the stress tensor before collision and $\overline{\mathbf{\Pi}}$ is the traceless stress tensor. Furthermore, λ is related to the viscosity, and λ_B determines the bulk viscosity of the fluid. For $c_s^2 = 1/3$ these are represented by:

$$\mu = -\frac{1}{6}\rho\left(\frac{2}{\lambda} + 1\right) \ , \tag{3.11}$$

$$\mu_B = -\frac{1}{3}\rho\left(\frac{2}{3\lambda_B} + \frac{1}{3}\right) \ . \tag{3.12}$$

The values of λ and λ_B are limited by $-2 < \lambda < 0$ to ensure a realistic value of the viscosity. The value of λ_B is set to -1 in this work (no contribution of bulk viscosity).

With the new stress tensor the distribution after collision is determined:

$$n_i + \Delta_i(n) = a^{c_i}\left(\rho + \frac{\mathbf{j}\cdot\mathbf{c}_i}{c_s^2} + \frac{(\rho\mathbf{u}\mathbf{u} + \mathbf{\Pi}^{neq\prime}) : (\mathbf{c}_i\mathbf{c}_i - c_s^2\mathbf{I})}{c_s^4}\right), \quad (3.13)$$

with $\mathbf{\Pi}^{neq} = \mathbf{\Pi} - \mathbf{\Pi}^{eq}$, and $\mathbf{I}$ the identity tensor.

3.2.3 Boundary conditions

The most straight-forward type of boundary condition in a lattice-Boltzmann simulation is the periodic boundary condition. This corresponds to a case where the system has no walls, and the simulation volume is infinitely repeated. Fluid that leaves the system on one side comes back in on the other side. This corresponds to a case where the system has no confining walls.

Solid boundaries (system walls or objects in the flow) can be chosen on the grid points or in the middle of two grid points. In this work the latter option is used. Bounce back boundary condition are used, where the fluid moves back in the direction from where it came:

$$n_i(\mathbf{r}, t+1) = n_{-i}(\mathbf{r}, t)\ , \quad (3.14)$$

with $-i$ being the link opposite to i. This results in a fluid velocity of zero in the middle of sites r and $r - c_i$ (thus at the boundary node), corresponding to no-slip conditions. When the boundary is moving, the bounce back method is adjusted in such a way that the velocity in between the sites equals the velocity of the boundary:

$$n_i(\mathbf{r}, t+1) = n_{-i}(\mathbf{r}, t) + 2a^{c_i}\rho\frac{\mathbf{u}_b\cdot\mathbf{c}_i}{c_s^2}\ . \quad (3.15)$$

3.2.4 Validity of simulation method

The lattice-Boltzmann method is a simplified model of a liquid or gas, and the validity of the results obtained from such a simple model is not evident.

Contrary to continuum simulations where a discretised version of the widely accepted Navier-Stokes equations for fluid flow is solved, or molecular dynamics simulations which are based on Newtonian equations of motion for each molecule, the lattice-Boltzmann method only simulates a 'real' gas or liquid flow when some special conditions are fulfilled. In particular, Chen et al. (1992) (among others) have shown that a Chapman-Enskog expansion of the lattice-Boltzmann results in the Navier-Stokes equations, provided that conditions on the lattice symmetry and Mach number are met. The first condition states that the lattice must be symmetric up to the fourth order tensor, which is the case for the D3Q19-model used in this work (Ladd and Verberg, 2001). The second condition requires the Mach number ($M = u/c_s$) in the simulations to be low ($M < 0.3$). At high Mach-numbers, the density in lattice-Boltzmann simulations can no longer be considered constant and unrealistic effects may occur.

The recovery of the Navier-Stokes equations from the lattice-Boltzmann equation proves that the model is capable of simulating actual flow phenomena.

3.3 Modelling large solid particles

Since space is discrete in lattice-Boltzmann simulations and boundary nodes are located only in the middle of links between fluid nodes, curved boundaries, such as the surface of large solid spheres, can only be modeled approximately. The boundaries are mapped on the grid by locating the boundary nodes that are closest to the actual boundaries. This is shown in figure 3.4. The interaction between fluid and solid is equal to the momentum change of the fluid at the boundary nodes. Summation of the interaction over all boundary nodes forming an object gives the total force on the object.

Due to this mapping the shape and diameter of the particle are clearly different from spherical. Therefore it is necessary to calibrate the effective diameter of the particle by simulating a single particle at low Reynolds number and measuring the drag force that the fluid exerts on it. The effective diameter of the particle is then that value for which the Stokes drag (or the Hasimoto drag (Hasimoto, 1959)) equals the drag on the simulated particle. The effective diameter of a particle depends on the original particle size d_0 and the viscosity of the fluid. Figure 3.5 shows the values for the effective radius that were provided with the code and two extra simulated values, all

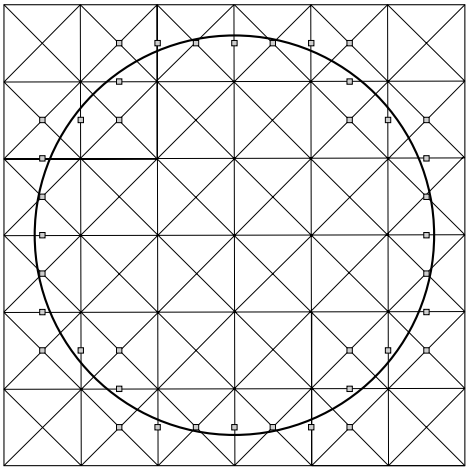

Figure 3.4: Mapping of a spherical particle on the lattice.

measured with a kinematic viscosity $\nu = 0.0008333$ (the value that we used in most of our simulations). The effective diameter of the particle for this viscosity fits the equation given by

$$\frac{d}{d_0} = \frac{1}{1.17 + 0.85 d_0} \,, \tag{3.16}$$

which is the line shown in figure 3.5. The effective diameter may also depend on system porosity and Reynolds number, although these last influences cannot be measured well since no exact theoretical correlations are available to compare the simulations to. Therefore it is assumed to be constant for all values of the porosity and Reynolds numbers.

As Nguyen and Ladd (2002) point out, the continuous relocating of boundary nodes for moving particles leads to small fluctuations in particle volume and thus drag force, which can be reduced by choosing optimal diameters d_0. Where possible, these diameters were used in this work, although it was not possible to find a good combination of diameters for all bi- and polydisperse systems. However, since the fluctuations are small, especially when large particles are involved ($d_0 > 4 - 6$ lattice sites), and since the results are averaged over multiple particles, several configurations and a large period of time, these fluctuations are not expected to influence the results described in this thesis.

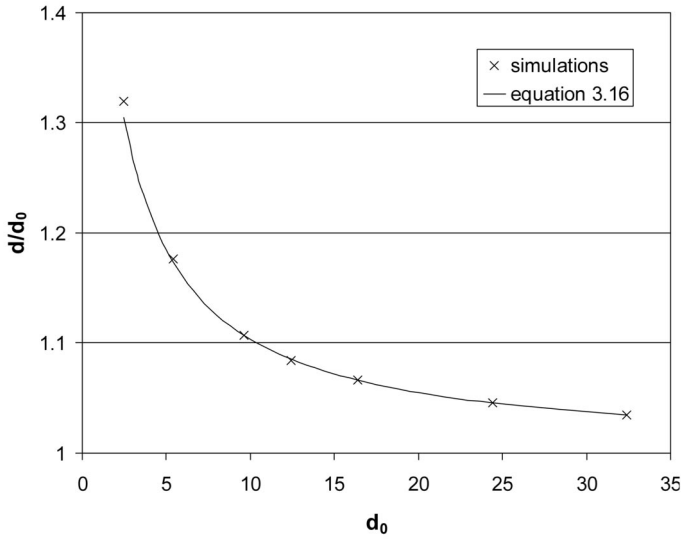

Figure 3.5: Effective diameter of particles in LBM-simulations for a viscosity of $\nu = 0.0008333$.

3.3.1 Finite size effects

The lattice-Boltzmann method is based on discretisation of time and space, and like with any other method that uses discretisation the resolution of the grid might influence the results. In case of low grid resolutions the number of lattice points in a pore is very low, resulting in a poor resolution of flow profiles and thus less accurate values for the drag force. The lattice-Boltzmann method is known to be second order with respect to the spatial discretisation, although for small particles this is not always observed due to the change in the shape of the particles with increasing grid resolution (Hill et al., 2001b). Figure 3.6 shows the simulation results for the drag force in a monodisperse system of porosity $\varepsilon = 0.5$. For these simulations particles with $d_0 = 9.6$, 12.4, 16.4, and 24.4 were used. The results scale indeed as $1/r_h^2$, and the line shows the extrapolation to $r_h = \infty$. Figure 3.7 shows similar results for the drag force in bidisperse systems at $\varepsilon = 0.5$. In this case, the drag force for both particle types scales linearly with $1/r_h^2$, as well as the average drag force calculated from the individual forces.

Even when the largest particles are used, the simulation results still show a deviation from the extrapolated drag force at $r_h = \infty$. Therefore, simulations with two different values of r_h were performed for each system, and

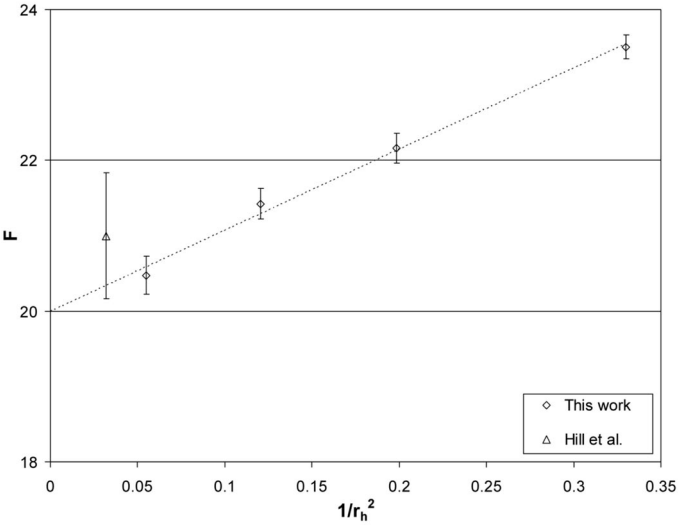

Figure 3.6: Finite size effects for the drag force in monodisperse systems with $\varepsilon = 0.5$.

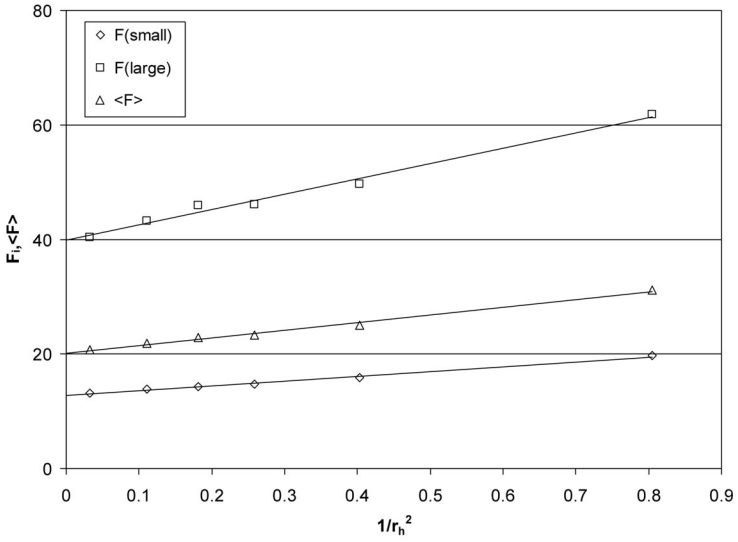

Figure 3.7: Finite size effects for the drag force in bidisperse systems with $\varepsilon = 0.5$.

the results were extrapolated. The dependency was found to be similar for other porosities and over a large range of Reynolds numbers, although for the highest Reynolds numbers some deviations were found, especially when very small particles were used. For this reason, these small particles were not used for the high Reynolds number simulations.

3.4 Simulation setup

3.4.1 Initial configurations

For the simulations systems of spheres that are packed randomly were used. Although this may look obvious, it should be noticed that there is no clear definition of a 'random system'. Several papers have appeared in literature that try to define a random porous system, based on e.g. the number of contact points with neighbouring particles or the distance to the neighbours (see e.g. To and Stachurski, 2004; Tewari and Gokhale, 2004). These methods are all based on statistical analysis of monodisperse systems that consist of many particles ($> 10^4$). The systems in this work do not contain enough particles to check randomness statistically. Moreover, for bi- and polydisperse mixtures no such tests are available. However, it is assumed that the Monte-Carlo method described below produces configurations that are sufficiently random for this work (i.e. no dominant orientation of pores, no formation of channels between particles). Averaging over several simulations with different initial configurations will minimize statistical fluctuations in the results caused by the low number of particles.

Randomisation procedure

Monodisperse systems are randomised using a standard Monte Carlo procedure (Frenkel and Smit, 2002). All particles are placed initially in an ordered configuration (simple cubic, body centred cubic or face centred cubic). Subsequently, each particle is moved randomly. Whether or not a move is accepted depends on the overlap: if there is any overlap with other particles at the new position, the move is rejected. In case of no overlap, the move is accepted and the coordinates of the particle are updated.

For bidisperse and polydisperse systems a slightly different algorithm is used, since the difference in radius between the particles and the composition of the

mixture sets extra limits on the porosity that can be reached in an ordered system without overlap. The desired number of particles is placed in an ordered position again, with the same options as for monodisperse systems. All diameters are set initially to the smallest diameter in the system. The large particles are chosen at random until the desired mixture composition is reached. When the diameters of the large particles are set to their actual size, overlap between neighbours may occur. This results in a potential energy E of the system, which is set to be equivalent to:

$$E = \left(\frac{|\mathbf{r}_1 - \mathbf{r}_2|}{R_1 + R_2} \right)^n \tag{3.17}$$

in case of overlapping particles and $E = 0$ otherwise. In equation (3.17), $\mathbf{r}_i$ stands for the particle position and R_i is its radius. The variable n is gradually increased during the process so that the interaction energy approaches that of hard spheres. The particles are moved at random, similar to the monodisperse case, but this time the acceptance of a move is determined by the potential energy of the system. If the potential energy decreases or stays equal, a move is always accepted. If the potential energy increases (more overlap in the new situation), a new random number is chosen. If this number is greater than a critical value, the move is rejected, otherwise it is accepted. The critical value is determined by the difference in energy between the old and new state:

$$c = \exp\left(k\left(E_{old} - E_{new}\right)\right) \ . \tag{3.18}$$

k is a constant and necessary to obtain reasonably small possibilities of acceptance. It is usually set to 50. It is clear that when the difference in energy between old and new state becomes larger (stronger overlap), the chance of acceptation of the move becomes smaller. In this way the energy of the system becomes smaller and smaller, until a final state is reached with very little overlap between the particles. All particle radii are then multiplied with a factor that eliminates all overlap between the particles, which will change the porosity slightly. When there is no overlap the scaling factor is equal to 1 and the porosity is not changed. Only when the change in porosity is less than 0.2 % the configuration is accepted as an initial state for the lattice-Boltzmann simulations.

3.4.2 Particle velocities

In the simulations all particles are given the same velocity, and a backflow flag is used that counteracts the force of the particles exerted on the fluid. However, the direction of the velocity has a strong influence on the path of the fluid through the voids, and thus on the drag force that the particles experience. Especially at high Reynolds numbers there may be a big difference between the interaction force of fluid being forced through a narrow pore, or fluid being able to move around the same pore. To prevent any effects of the direction of flow this is chosen at random and results from several simulations using different configurations and directions of flow are averaged.

3.4.3 Simulation procedure

An initial random configuration was made as described in section 3.4.1. All particles in this configuration were given the same velocity in a random direction. Variation in Reynolds number was obtained by varying the magnitude of the velocities. For very high Reynolds numbers it was necessary to adjust the particle sizes as well, as variation of only the velocity resulted in unstable simulations. A backflow flag was used, which applies a uniform force to the fluid that balances the drag force of the particles. The effect of this force is that the fluid moves in the opposite direction of the particles, thereby ensuring that the total momentum flux through the system is equal to zero. The resulting fluid velocity is then $\mathbf{u}_f = -\mathbf{u}_p \cdot (1-\varepsilon)/\varepsilon$. The superficial velocity is then exactly equal to the particle velocity: $\mathbf{U} = \varepsilon \cdot (\mathbf{u}_p - \mathbf{u}_f) = \mathbf{u}_p$. This value is used in the determination of the normalised drag forces from the simulations.

The velocity of the particles is not influenced by the drag force by setting their mass to infinity, and no other forces are acting on the particles. Thus, the configuration and velocity of the particles stay fixed, keeping the system well defined during the entire simulation.

Most monodisperse simulations were performed using diameters of 17.5 or 25.5 lattice sites. For binary systems mixtures were used with diameters ranging from 6.4 to 64.4 sites. High Reynolds numbers usually required large diameters to prevent the simulations from becoming unstable. Occasionally diameters of only 4.4 lattice sites were used at low Reynolds num-

bers for extrapolation purposes (see below and section 3.3.1). The viscosity that was used in nearly all simulations was $\mu = 1/1200$. This small value ensures that high Reynolds numbers can be achieved using velocities still within the stable region of low Mach numbers. Velocities used ranged from $1 \cdot 10^{-5}$ to 0.02, and occasionally 0.025 was used for extrapolation at high Reynolds numbers. With these values Reynolds numbers were varied from 0.2 to 1000 for monodisperse simulations, and for the binary mixtures the average Reynolds number varied from 0.1 to 500. Porosities were varied from 0.4 to 0.9 for monodisperse systems, and for binary systems a porosity of 0.35 was included in the simulations as well. In the bidisperse simulations, diameter ratios ($d_{\text{small}}/d_{\text{large}}$) between the particles ranged from 0.25 to 0.7, and several volume fractions of large and small particles were used. Simulations were run for $200 - 400$ cycles of each 1000 time steps. Forces on the particles were measured and averaged over each cycle.

The lattice-Boltzmann method suffers from some finite size effects, like all simulation methods that use discretisation. Larger particles have more boundary nodes, implying that the force can be calculated more precisely. To correct for this finite size effect all simulations were repeated using a smaller system, keeping the same simulation parameters like number of particles, porosity and Reynolds number. In the simulations of bi- and polydisperse systems the configurations were kept equal as well (all sizes were scaled down).

3.4.4 Analysis of results

The simulation program calculates the force exerted on each particle during each cycle. This is equal to $\mathbf{F}_{f\to s}$ in equation (2.1). This force is converted to the actual drag force $\mathbf{F}_d$ by multiplying with $1/\varepsilon$ and subsequently normalised with the Stokes-Einstein drag as described in equation (2.6). The normalised drag force is averaged over all particles in monodisperse simulations and over all particles of the same type in polydisperse simulations. After the simulation has reached steady state (usually after $50-150$ cycles), the forces are averaged over a longer period, e.g. $100 - 200$ cycles.

Figure 3.8 shows a typical example of the normalised drag force that was measured in simulations with the same porosity and Reynolds number, but with different configurations and flow directions. This figure illustrates that the drag force depends on the configuration of the particles, which is the

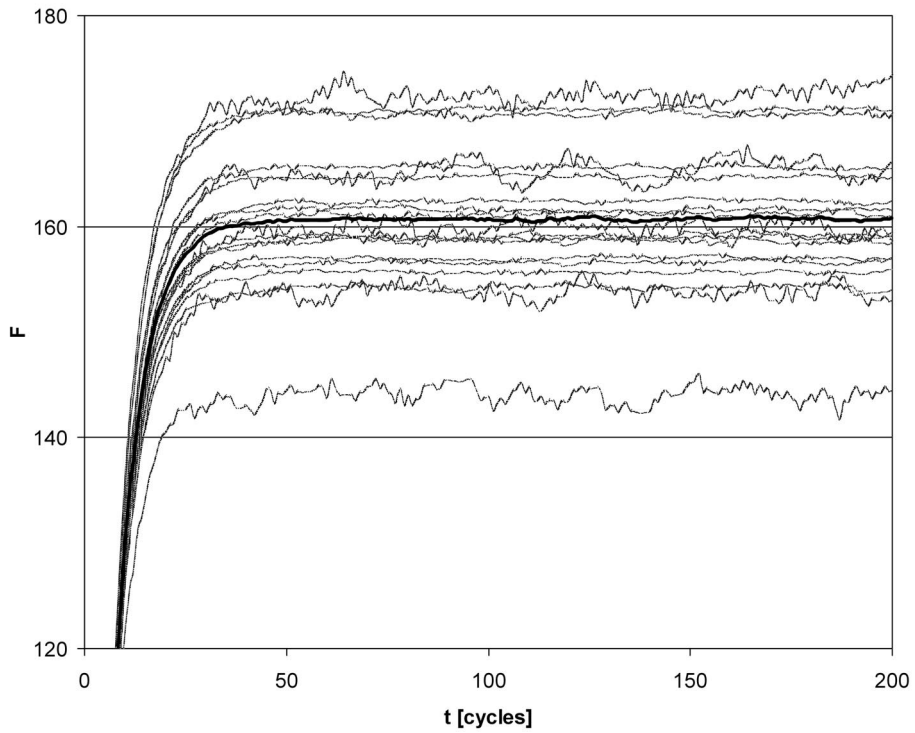

Figure 3.8: Normalised drag forces measured in simulations with identical porosity and Reynolds number, but different configurations and flow directions. The thick solid line is the average over all simulations.

reason why the data reported in this thesis are averaged over several simulations. The bold line is the average value over all configurations. It takes some time for the system to come to a steady state (in figure 3.8 on average 40 cycles), but even when this plateau is reached fluctuations in the drag force keep occurring, and for that reason the data were also averaged over a longer period (e.g. from $t = 100$ to $t = 200$ cycles). The fluctuations are stronger in some simulations than in others, which is presumably related to the direction of the velocity, as the effective volume of a particle is more influenced by movement in some directions than in other directions.

The number of configurations was up to 30 for monodisperse simulations. For bidisperse simulations usually only five configurations were used, as the parameter space is much larger and it would require too much CPU-time to use more configurations. Tests indicated that the difference between the

average drag force obtained from five configurations and a drag force from ten configurations was usually less than 2.5 %, although a difference of 4 % was occasionally observed in a simulation with very high Reynolds numbers ($\langle Re \rangle = 1000$). To prevent any influence of a small variation in porosity between the various configurations the drag forces were all extrapolated to the same porosity, by a second order Taylor approximation using some initial estimate for the functional form of F.

The drag force in the simulations is influenced by finite size effects, which are second order in grid resolution. Therefore, all simulations were repeated on a smaller scale, and the results of both simulations were plotted against $1/r_h^2$ with r_h defined in equation (2.29). Linear extrapolation to $1/r_h^2 = 0$ gave the result for infinitely large particles, which is the value that is given in the results section.

3.5 Discrete particle model (DPM)

The discrete particle model was originally developed by Hoomans et al. (1999). Below an overview of the main equations is given. A more extensive description can be found in Hoomans (1999) and van der Hoef et al. (2005).

In the discrete particle model the gas phase is described by the volume-averaged Navier-Stokes equations. The continuity equation for the gas phase is given by:

$$\frac{\partial (\varepsilon \rho)}{\partial t} + \nabla \cdot \varepsilon \rho \mathbf{u} = 0 \, , \tag{3.19}$$

where ε is the porosity of the system, ρ_g the density of the gas and $\mathbf{u}$ the gas velocity. The momentum equation for the gas phase is given by:

$$\frac{\partial (\varepsilon \rho \mathbf{u})}{\partial t} + \nabla \cdot \varepsilon \rho \mathbf{u}\mathbf{u} = -\varepsilon \nabla P - \mathbf{S}_p - \nabla \cdot \varepsilon \tau + \varepsilon \rho \mathbf{g} \, . \tag{3.20}$$

In this equation P is the pressure, τ the viscous stress tensor and $\mathbf{g}$ the acceleration due to gravity. $\mathbf{S}_p$ is a source term that is related to the two-way coupling which is important at high solids volume fractions typically used in this study.

The particle dynamics are based on Newton's equations of motion, which for particle p reads:

$$m_p \frac{d\mathbf{v}_p}{dt} = m_p \mathbf{g} + \frac{V_p \beta}{(1-\varepsilon)} (\mathbf{u} - \mathbf{v}_p) - V_p \nabla P \, , \tag{3.21}$$

where m_p, V_p and $\mathbf{v}_p$ are the mass, volume and velocity of the particle, respectively. The second term on the right hand side is the drag force, where β is the inter-phase momentum exchange coefficient, which is directly related to the dimensionless drag force (see next section).

Particle collisions can be handled in two ways. The first is a hard sphere approach, where collisions are assumed to be binary and instantaneous. Collision rules are derived from Newton's laws. Three parameters have influence on the collisional interaction: the restitution coefficient e $(0 < e < 1)$, the friction coefficient μ $(\mu > 0)$ and the tangential restitution coefficient β_0 $(\beta_0 > 0)$. These parameters determine the amount of energy that is lost during a collision and the velocities of the particles after the collision.

The other approach to account for collisions is the soft sphere model. This is a linear spring/dash-pot model where the force on a colliding particle is determined by the amount of (fictitious) overlap it has with other particles. Multiple collisions are possible in this model. Contrary to the hard-sphere model that is event-driven (the system evolves from collision to collision), the soft-sphere model uses a fixed time step. Therefore, the soft-sphere model is preferred in cases where many collisions occur, e.g. in very dense systems.

3.5.1 Drag force in DPM

The size of the computational cells in the discrete particle model typically exceeds the diameter of the particles. No direct interaction occurs on the surface as in the lattice-Boltzmann model, and therefore a closure model for the drag force has to be implemented. This is done via the inter-phase momentum exchange coefficient β, which is defined as:

$$\mathbf{F}_d = \frac{V_p \beta}{(1-\varepsilon)} \left(\mathbf{u} - \mathbf{v}_p\right) \ . \tag{3.22}$$

The local porosity and gas velocity necessary for the evaluation of this equation are obtained through a volume-weighted averaging procedure (Hoomans, 1999). The force of a particle on the gas phase is distributed to the surrounding cells by the same technique. The momentum exchange coefficient is related to the normalised drag force used in this work as follows:

$$\beta = \frac{18\mu}{d^2} \varepsilon \left(1-\varepsilon\right) F \ . \tag{3.23}$$

Most models use the empirical Ergun-equation (equation (2.32)) for porosities up to 0.8, combined with the Wen and Yu drag correlation (equation (2.35)) at higher porosities (see e.g. Enwald et al., 1996). Bokkers et al. (2004) compared results obtained with this equation to simulations using the drag relation that was derived from lattice-Boltzmann simulations by Hill et al. (2001b). The latter equation was shown to give results that agreed better with experiments than simulations where the empirical models were used. The drag relation that was derived in this work was also implemented in the discrete particle model, for which the results are presented in chapter 6.

Chapter 4

Simulation results: monodisperse systems

Abstract

This chapter presents the results of the lattice-Boltzmann simulations for the drag force on spherical particles in monodisperse systems of varying porosities ($\varepsilon = 0.4 - 0.9$). The Reynolds numbers in these simulations were varied from $Re < 1$ to $Re \approx 10^3$. The results are compared to other data and several correlations (both theoretical and empirical) from literature. A new correlation that fits the results better than the literature relations is introduced, which consists of a single equation for all porosities and Reynolds numbers. This is considered to be a great advantage over other relations, which are often valid for a limited range of porosities and/or Reynolds numbers only or consist of several equations for the various regimes.

4.1 Introduction

Due to the enormous increase in computer capacities in recent years, it is anticipated that CFD-models will become important tools in the design and optimisation of chemical reactors. The success of these models in simulations of large scale processes depends heavily on the availability of closure relations to accurately describe the micro-scale processes. One of these processes is the interaction between solid particles and the surrounding fluid (liquid or gas), e.g. in fluidised bed reactors. As reported in chapter 2 there is no comprehensive theoretical approach, especially when high packing fractions and/or high Reynolds numbers are involved. It is also difficult to measure the fluid-solid interaction experimentally. The drag force on single particles can be measured in very small and dilute systems only, whereas in larger systems information has to be obtained via indirect methods such as pressure drop measurements over an entire reactor or the terminal velocity of sedimenting particles. As mentioned in chapter 2, for this reason most correlations that are currently available were obtained from experimental data taken in a limited range of porosities (e.g. fixed and slightly expanded beds) and/or Reynolds numbers, which means that, in principle, their validity is also limited. In this work, lattice-Boltzmann simulations were used to calculate the drag force on spherical particles over a large range of porosities and Reynolds numbers. The fluid flow in this model is solved on a scale smaller than the particle diameter, which enables accurate calculation of the interaction force between fluid and particle. The method was described in section 3.2, and the simulation setup in section 3.4. The simulation method enables the study of well defined systems, in contrast to experiments where conditions in the reactor may vary in time and space.

Figure 4.1 shows an example of a porous system as studied in the computer experiments. This configuration consists of 54 spheres, each with a diameter of 17.5 lattice sites, with a system porosity equal to 0.5. The particle configuration was generated using the Monte Carlo method described in section 3.4.1. The simulation volume has periodic boundary conditions, which means that during a simulation all particles are surrounded by other particles and the flow is not influenced by wall effects. Figure 4.2 is a cross-section of the flow through this system after steady state has been reached. In this figure, the white spots are the particles while the arrows indicate the velocities on the lattice nodes. The velocities are adjusted in such a way that the particles are at rest while the fluid is flowing through the system. The arrows point in the direction of the flow, while their length and thickness

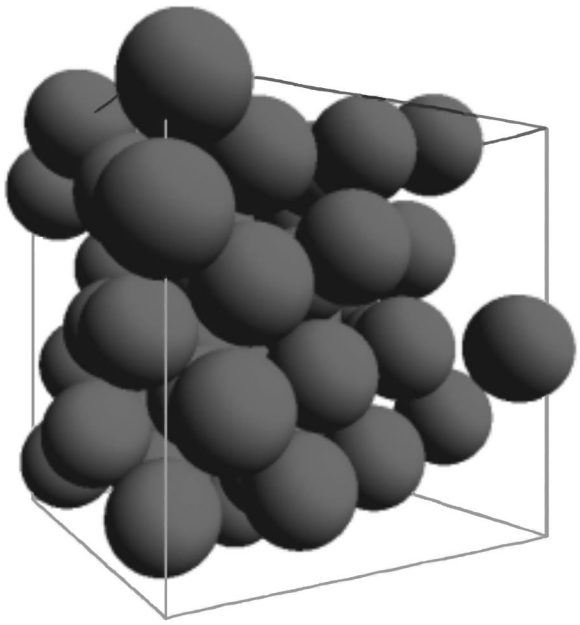

Figure 4.1: Example of a monodisperse system as studied in the LBM-simulations. $N = 54$, $d = 17.5$ lattice sites, $\varepsilon = 0.5$.

indicate the magnitude of the velocity. At the particle boundaries no-slip conditions apply, shown by the low fluid velocities near these boundaries. The fluid velocity reaches a maximum in large pores where it is not hindered by particles, as could be expected.

4.2 Low Reynolds numbers

Table A.1 in appendix A shows the averaged results from the lattice-Boltzmann simulations for the normalised drag force in a monodisperse random array of spheres at low Reynolds numbers. These data were obtained from the simulation results according to the method described in section 3.4.4. These results are also shown in figure 4.3, where they are compared to several drag relations and three other sets of simulation data. The data from Ladd (1990) and Mo and Sangani (1994) were obtained via a multipole expansion of the force density on the surface of the spheres, where the fluid motion is described by the Stokes equations. Hill et al. (2001a) used lattice-Boltzmann

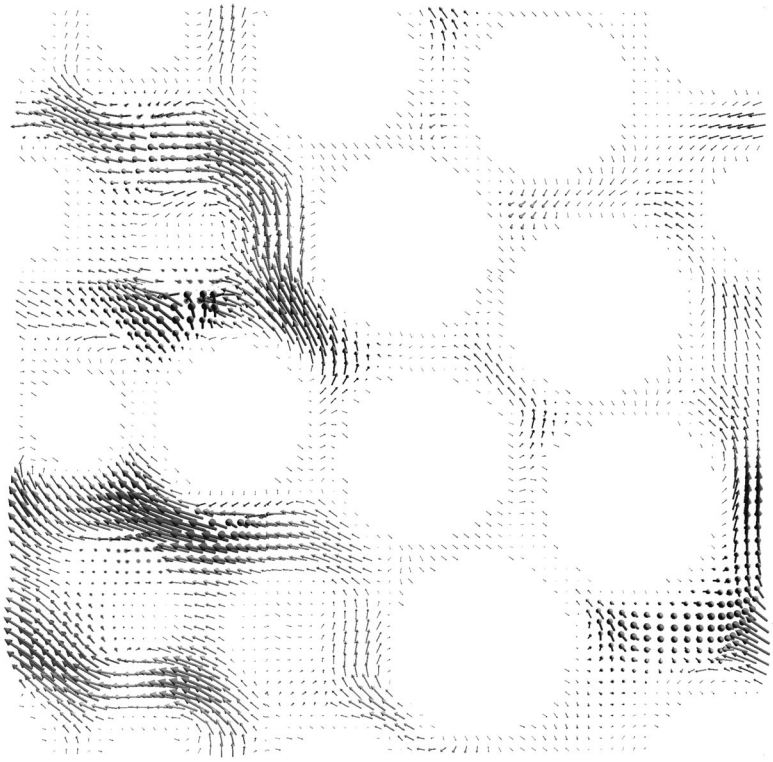

Figure 4.2: Cross-section of flow through the monodisperse system in figure 4.1 during lattice-Boltzmann simulation.

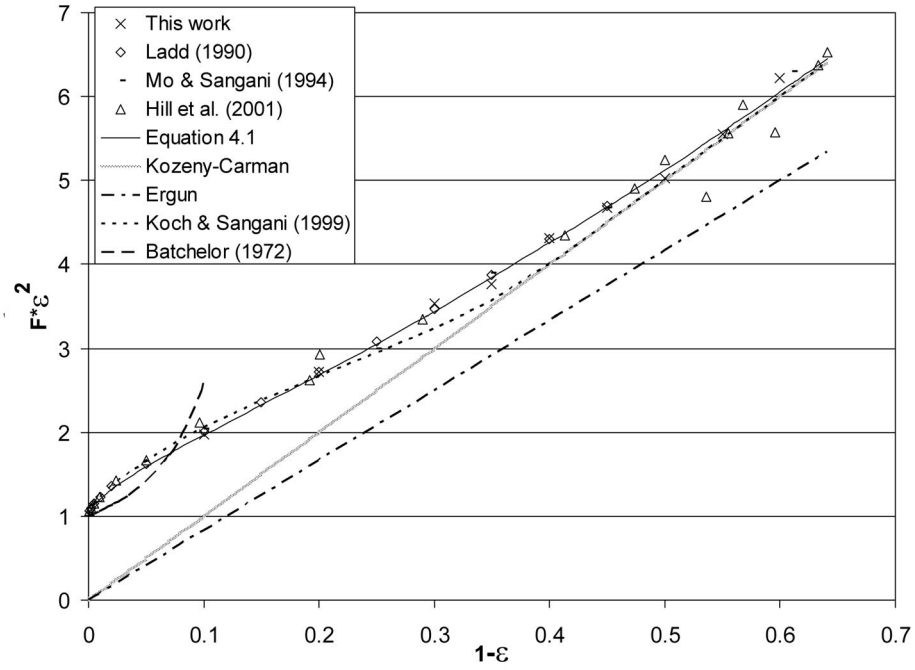

Figure 4.3: Normalised drag force in monodisperse systems as a function of packing fraction. Data from our simulations are compared to simulation data from literature. The solid line is the best fit to the data (equation (4.1)), other lines are drag relations from literature.

simulations in their calculation of the drag force. The simulation results are in very good agreement with the literature data, although the data from Hill et al. (2001a) suffer from somewhat more scattering, in particular for higher packing fractions, which could be caused by insufficient sampling. In the simulations, it was found that for densely packed systems, the individual results for each configuration can be very different, due to the limited number of particles. Rather than increasing the number of particles, it was decided to obtain data for more independent configurations and flow directions (up to 30 in total), and in the final average all data were omitted that were outside 2.5 times the standard deviation, as calculated from the initial average.

The solid line in figure 4.3 is the best fit to all simulation data, which takes the following simple form:

$$F(\varepsilon) = 10\frac{1-\varepsilon}{\varepsilon^2} + \varepsilon^2\left(1 + 1.5\sqrt{1-\varepsilon}\right) \ , \tag{4.1}$$

i.e. the Carman equation with a term added in order to have the correct limiting behaviour for $\varepsilon \to 1$. The largest deviation of this fit with either the present lattice-Boltzmann data and multipole expansion data from Ladd (1990) and Mo and Sangani (1994) is 3 percent. Since all these data sets are obtained by two completely independent simulation methods, it is claimed that equation (4.1) represents the true drag force for random arrays of monodisperse spheres to within 3 percent, and probably less. The Kozeny-Carman equation, the Ergun equation and the relation by Koch and Sangani (1999) are also shown in figure 4.3.

4.3 Intermediate and high Reynolds numbers

The simulation data for the normalised drag force in monodisperse systems at higher Reynolds numbers are presented in table A.2 in appendix A. Figure 4.4 shows the data as a function of the Reynolds number. Although many drag relations from literature, e.g. the Ergun equation, assume a linear dependency on the Reynolds number, these data suggest that this is not true over the entire range. This becomes more obvious when the variable α is plotted, defined as:

$$\alpha = \frac{F(\varepsilon, Re) - F(\varepsilon, 0)}{Re} , \tag{4.2}$$

as is shown in figure 4.5.

The lines in figures 4.4 and 4.5 represent the best fit to the simulation data, which is given by the equation:

$$\alpha = \frac{0.413}{24\varepsilon^2} \frac{\left(\frac{1}{\varepsilon} + 3\varepsilon(1-\varepsilon) + 8.4Re^{-0.343}\right)}{\left(1 + 10^{3(1-\varepsilon)}Re^{-\frac{1}{2}(1+4(1-\varepsilon))}\right)} . \tag{4.3}$$

The simulation results show the largest deviation from this equation in the intermediate Reynolds range. Part of this deviation may be caused by the magnitude of the Reynolds dependent part of the drag force in the region, which is quite low, and therefore minor fluctuations in the overall drag force result, within the error of the simulation method, form an important deviation when α is calculated from these results. The standard deviation in α at $Re = 21.0$ is often $5-6$ %, whereas for higher Reynolds numbers this is only $1-2$ %. It should be noted that in the same range of intermediate

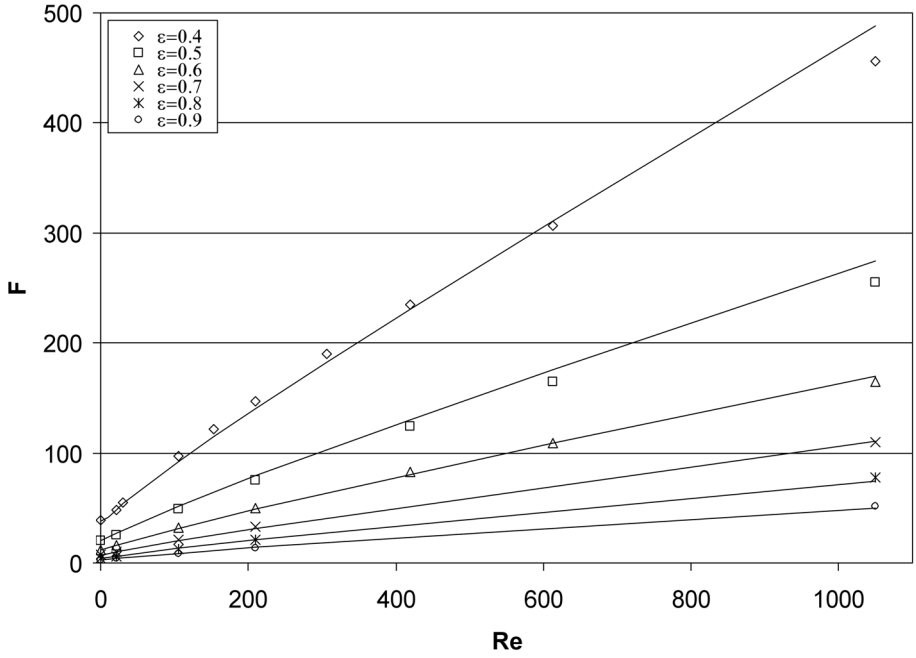

Figure 4.4: Normalised drag force in monodisperse systems as a function of Reynolds number for various packing fractions.

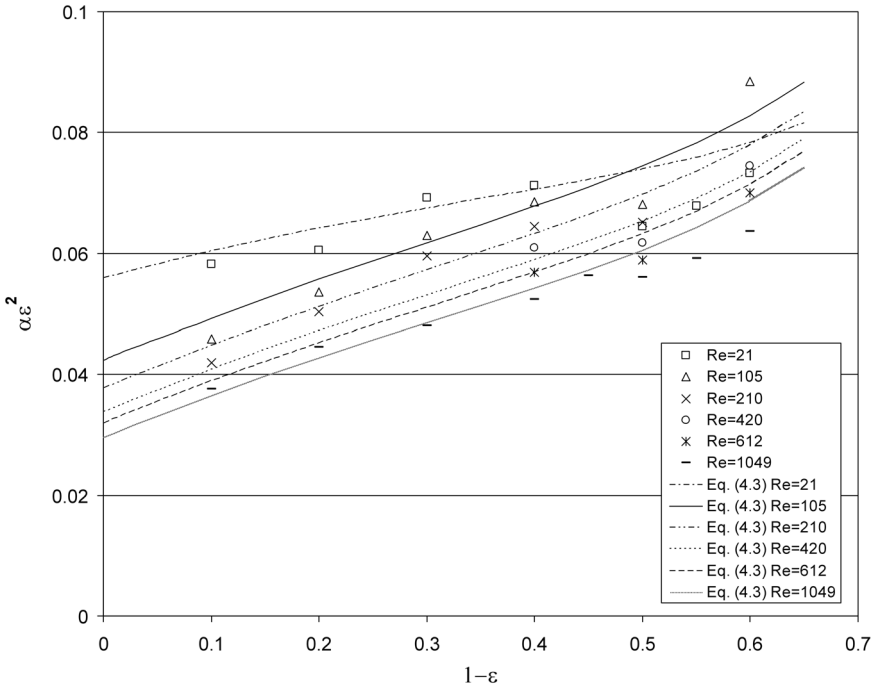

Figure 4.5: Reynolds dependent part of drag force in monodisperse systems as a function of packing fraction (α as defined in equation (4.2)).

Reynolds number several literature drag relations show a gap as well, e.g. Hill et al. (2001b) do not give a relation for $2 < Re < 40$, and Fand et al. (1987) found a transition regime in the range $80 < Re < 120$.

From equation (4.3) we arrive at the final expression for the normalised drag force at arbitrary Reynolds number (up to $Re = 1000$):

$$\begin{aligned} F(\varepsilon, Re) &= 10\frac{1-\varepsilon}{\varepsilon^2} + \varepsilon^2\left(1 + 1.5\sqrt{1-\varepsilon}\right) \\ &\quad + \frac{0.413Re}{24\varepsilon^2}\frac{\left(\frac{1}{\varepsilon} + 3\varepsilon(1-\varepsilon) + 8.4Re^{-0.343}\right)}{\left(1 + 10^{3(1-\varepsilon)}Re^{-\frac{1}{2}(1+4(1-\varepsilon))}\right)} . \end{aligned} \tag{4.4}$$

The lines in figure 4.4 show the predictions from equation (4.4) for the porosities that were used in the simulations. The average deviation of the simulation results from the prediction is 3.05 %, where the maximum deviations ($6.8 - 7.5$ %) are found for high Reynolds numbers and dense systems ($\varepsilon = 0.4 - 0.5$).

An important advantage of equation 4.4 over other drag relations (Ergun, Hill et al.) is its limiting behaviour for $\varepsilon \to 1$. For high Reynolds numbers, α approaches the value 0.413/24, which is equal to the limit of the Turton and Levenspiel-equation (equation (2.23)).

4.4 Discussion

Figures 4.6 to 4.9 compare our simulation data to various literature drag relations. In these figures, all lines are calculated for the same porostities that were used during the simulations, where the highest line always represents $\varepsilon = 0.4$, and the lowest $\varepsilon = 0.9$. One of the most striking results is that the Wen and Yu-relation is not a good approach in the high porosity regime, whereas this is the region where it is most often applied in CFD-simulations of gas-fluidised beds. At lower porosities the agreement with the simulation data is fair, where it should be noticed that the slope (α) at low Reynolds numbers is far too high. The Ergun relation performs reasonably well in dense beds, although at high Reynolds numbers the deviations from the current simulation results are considerable. In more dilute beds the predictions from the Ergun equation are a factor of 2.5 off, which is not surprising considering the fact that Ergun (1952) derived his equation

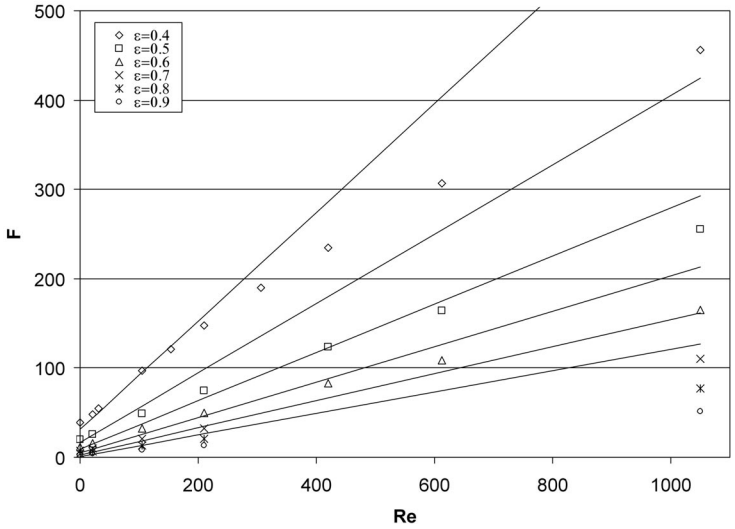

Figure 4.6: Simulation results for normalised drag force in monodisperse systems compared to Ergun relation (equation (2.32)).

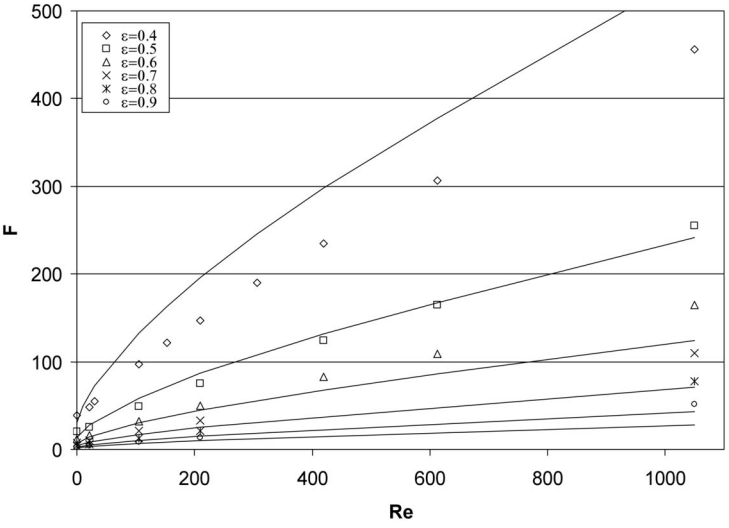

Figure 4.7: Simulation results for normalised drag force in monodisperse systems compared to Wen & Yu relation (equation (2.35)).

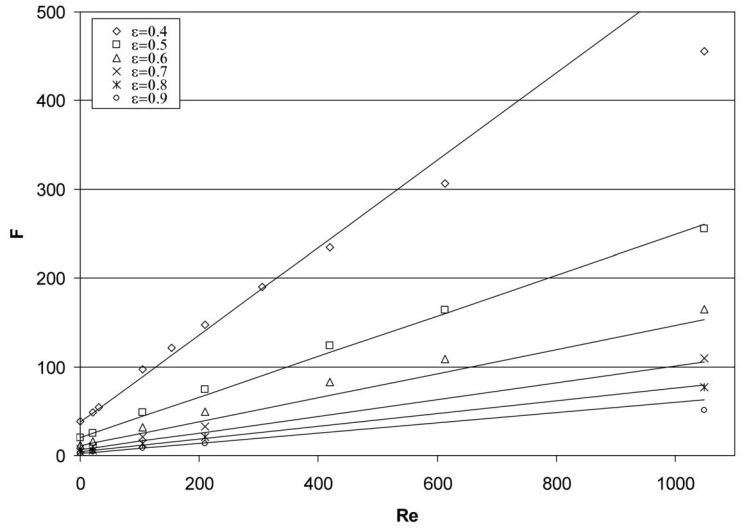

Figure 4.8: Simulation results for normalised drag force in monodisperse systems compared to relation of Hill et al. (2001b) (equation (2.42)).

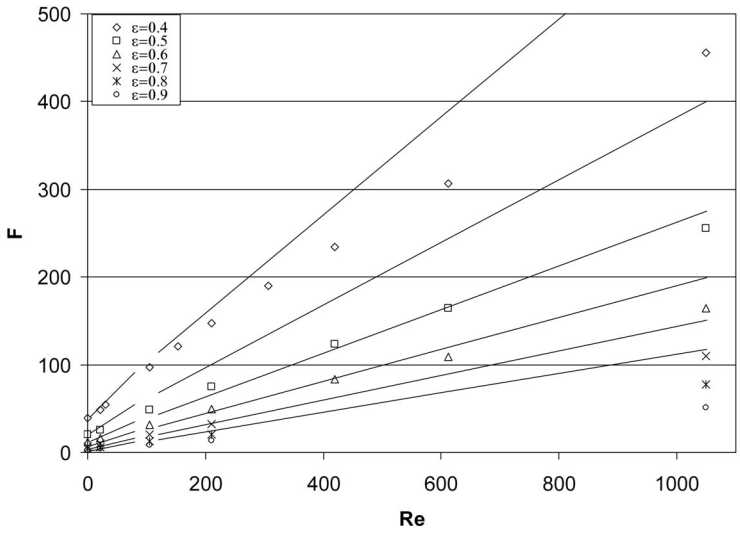

Figure 4.9: Simulation results for normalised drag force in monodisperse systems compared to relation of Fand et al. (1987) (equation (2.34)).

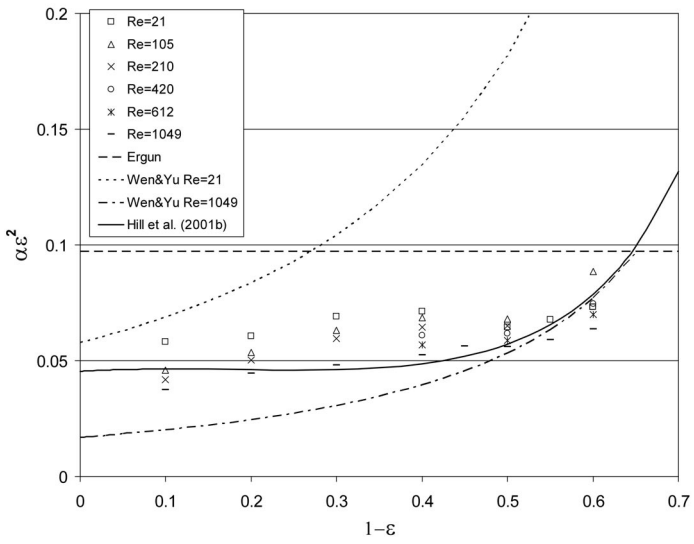

Figure 4.10: Reynolds dependent part of drag force (α as defined in equation (4.2)) compared to Ergun (equation (4.2)), Wen and Yu (equation (2.35)) and Hill et al. (2001b) (equation equation (2.42)).

from experiments in the range of $\varepsilon = 0.43 - 0.54$ only. For the drag forces calculated with the equations of Fand et al. (1987) more or less the same remarks apply as for the Ergun equation, which is not remarkable since the two are very similar. Fand et al. (1987) obtained their data in dense packed beds with a porosity of $\varepsilon = 0.34 - 0.36$. The relation of Hill et al. (2001b) gives a far better agreement with the lattice-Boltzmann results but deviates slightly at higher Reynolds numbers, which can be explained by the fact that they only used simulations with Reynolds numbers that did not exceed $Re = 150$.

Figure 4.10 compares the results for α from the simulations to several literature relations. Ergun (1952) predicts a fixed value for $\alpha\varepsilon^2 = 1.75/18$, independent of the Reynolds number. The relation of Hill et al. (2001b) does not depend on the Reynolds number either, but its predictions are in reasonable agreement with the simulation data. For the Wen and Yu equation two lines are shown that represent the highest (1049) and lowest (21.0) Reynolds number of the simulations, where the predictions for $21 < Re < 1049$ lie in between these lines.

Another comparison with the Wen and Yu-type of relations can be made via

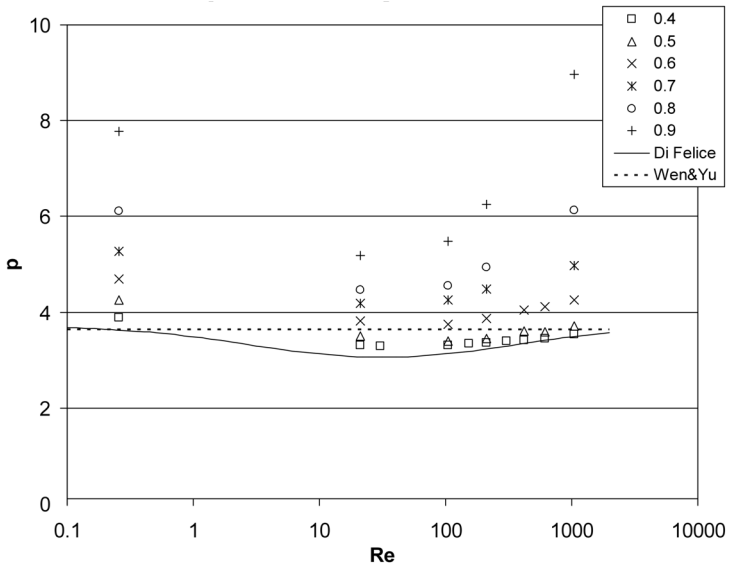

Figure 4.11: Exponent p in Wen & Yu type drag relations calculated from our simulation results for various porosities, compared to Wen & Yu equation and relation of Di Felice (1994).

the value for the exponent p, which can be calculated from our simulation results via $p = -^{\varepsilon} \log\left(F\left(\varepsilon, Re\right)/F\left(1, Re\right)\right)$, where the drag on a single particle is calculated with the equation of Turton and Levenspiel (1986). Figure 4.11 shows that the power p is by no means independent from ε and Re as assumed in the Wen and Yu-equation. Other equations of the same type take into account a dependency on the Reynolds number, e.g. the equation of Di Felice (1994) (equation (2.41)), which is a good approximation of the simulation data when $\varepsilon < 0.5$. However, the simulation results clearly suggest that at higher porosities there is a dependency of p on the porosity as well, raising serious doubts about the validity of this approach.

The simulation results that were presented here are the results for the *average* drag force on a single particle in a monodisperse system. The drag force on each individual particle may vary significantly: a factor 2 to 3 between the highest and lowest individual drag forces in a single simulation is not uncommon, and factors up to 6 have been noticed in cases of high Reynolds numbers. The variations are larger in systems with higher porosities, probably because the variations in pore size are larger in these situations. In systems with a low porosity there is not enough space available to form

large pores, ensuring a truly homogeneous system and thus homogeneous flow field, whereas in more dilute systems the freedom in positioning the particles is much larger, resulting in a larger range of interparticle distances and less homogeneous flow field (see also figure 4.2). A related effect is the blocking of some particles from the fluid flow by neighbouring particles: if a particle is in front of another particle with respect to the flow direction, the flow will try to find a way around the ensemble. In dense systems this is not always possible and the flow is forced to move along all particles, whereas in more dilute systems the fluid surrounding the second particle will be more at rest and thus this particle experiences a lower drag force. Experiments and simulations by Liang et al. (1996) confirm the influence of the orientation and distance of neighbouring particles on the drag force. Lattice-Boltzmann simulations on the drag force in clusters of particles (see chapter 7) illustrate the effect of shielding by other particles as well: a particle in the core of a cluster experiences a much lower drag force than a particle in the outer region because the flow in the pores of the cluster is much smaller than the flow around it. Further evidence that the differences are related to inhomogeneities in the spatial configuration rather than caused by other fluctuations is provided by the fact that the drag forces on individual particles in a simulation do not fluctuate much in time. However, it is not in the scope of this research to investigate the variation in local porosity. It is also not clear whether the use of a local porosity in the drag relation would result in a more accurate drag force on the individual spheres. In principle, this could be tested by lattice-Boltzmann simulations. Furthermore, when applying the drag relation in larger scale CFD-simulations the effect will usually be ignored, as the porosity is calculated at a scale of computational cells several particle diameters large, and it would be too expensive to calculate a porosity for each particle, which involves an evaluation of the local geometry of the neighbouring particles.

The systems with low porosities (notably $\varepsilon = 0.4$ and $\varepsilon = 0.45$) show some ordering in their structure: the particle configuration resembles a BCC-lattice. It is known that especially for higher Reynolds numbers this influences the drag force on the particles, in particular when the flow is in one of the main lattice directions (Hill et al., 2001b). However, since the results are averaged over different random flow directions and over several configurations (in each of which the particles are displaced slightly with respect to the BCC-configuration) it is expected that the results are not strongly influenced by the order. Furthermore, previous investigations have shown that in dense systems at low Reynolds numbers the differences in pressure

drop over ordered and random systems are minor when high packing fractions are involved. Zick and Homsy (1982) showed that for packing fractions greater than 0.5 the difference between the Kozeny-Carman drag for random systems and the drag in ordered arrays is usually less than 15 %, and slightly more when close to the maximum packing fraction (0.68 for BCC-lattices). Since such high packing fractions are not used in these simulations it is believed that the results presented here are a valid approximation of the drag force in random systems. Sangani and Acrivos (1982) mentioned that an estimation of the drag force in random dense systems, based on the drag in ordered dense systems, was in close agreement with the Blake-Kozeny equation. Furthermore, it should be noticed that some ordering seems to be inevitable in practical applications of low porosity systems as well. In systems with higher porosities there was no evidence of order in the configuration.

In this thesis only static beds of particles were investigated. In discrete particle simulations of fluidised beds however, the particle are moving about. The drag force is usually calculated with this individual particle velocity, an assumption that seems to be justified although its validity demands further research. Some preliminary lattice-Boltzmann simulations showed that in cases with a low granular temperature, where the mean square velocity was of the order of the flow velocity, the differences between the drag force in a static bed and the drag force based on the individual particle velocity are negligible, whereas in case of larger fluctuating velocities the results were not yet conclusive. High granular temperatures occur mainly in regions with high (fluid) velocity gradients, e.g. around a jet, or in regions with steep porosity gradients like the wake of a bubble.

4.5 Conclusions

The new relation for the drag force in porous systems of monodisperse spherical particles (equation (4.4)) was derived from lattice-Boltzmann simulations over a wide range of porosities ($\varepsilon = 0.4-0.9$) and Reynolds numbers ($Re < 1$ to $Re \approx 10^3$). It fits the LBM data better than the relations from literature, which often apply for a limited range of the porosity and/or Reynolds number only, even though they are often used outside of this range. Furthermore, a major advantage of the new relation is that it consists of a single simple equation for all porosities and Reynolds numbers, which means that

there are no undefined ranges for the drag force (like in the relations of Hill et al. (2001b) or Fand et al. (1987)) and no discontinuities occur in the drag force (like in the combination of the Ergun and Wen and Yu-equations).

The new relation may be implemented in larger scale CFD-models as discussed in section 1.5. The drag force in these models is often represented by an interphase momentum transfer coefficient β (see equation (2.8)), which for the drag relation in equation (4.4) corresponds to:

$$\begin{aligned}\beta &= 180\frac{\mu}{d^2}\frac{(1-\varepsilon)^2}{\varepsilon} + 18\frac{\mu}{d^2}\varepsilon^3(1-\varepsilon)\left(1+1.5\sqrt{1-\varepsilon}\right) \\ &\quad +0.31\frac{\left(\frac{1}{\varepsilon}+3\varepsilon(1-\varepsilon)+8.4Re^{-0.343}\right)}{\left(1+10^{3(1-\varepsilon)}Re^{-\frac{1}{2}(1+4(1-\varepsilon))}\right)} \,. \end{aligned} \tag{4.5}$$

The results of discrete particle simulations where this expression for β is used will be presented in chapter 6.

Finally, it should be noted that the lattice-Boltzmann simulations were all performed in homogeneous, static, monodisperse systems, where the average drag force was measured. Equation (4.4) does not take into account the effect of inhomogeneities like bubbles or clusters, variations in the local porosity, particle size distribution, or individual particle velocities. The drag force in bi- and polydisperse systems is investigated in the next chapter, and the effect of clustering in chapter 7. The other topics require further research, for which the lattice-Boltzmann method is also very well suited.

Chapter 5

Simulation results: bi- and polydisperse systems

Abstract

This chapter presents the results of lattice-Boltzmann simulations of the flow through mixtures of bidisperse spheres of varying porosity ($0.4 - 0.9$)*, diameter ratio* ($0.25 - 0.7$)*, mixture composition and Reynolds number (0.1-500). For low Reynolds numbers, the average drag force from these simulations agrees on average within* 5% *with the equation for the drag force in monodisperse systems. At higher Reynolds numbers the deviation is larger, especially in the simulations with an average Reynolds number* $\langle Re \rangle = 100$*. This is also the region where the largest deviation was found in the simulations of monodisperse systems.*

The drag force on individual particles was compared to equation (2.56) that was based on theoretical considerations, and matched this equation within 15 %*. A systematic deviation in the results was overcome by adding an extra term to this equation, leaving an average deviation of less than* 5 % *in* $F_i / \langle F \rangle$*. Literature values of Koo and Sangani (2002) confirm the validity of this equation. Simulation results are compared to the theory of Patwardhan and Tien (1985), which generates errors in the same order as the new equation. However, the new method is believed to be easier in the use.*

5.1 Introduction

The previous chapter presented a new relation for the drag force in systems consisting of monodisperse spherical particles, that was derived from lattice-Boltzmann simulations. In reality however, truly monodisperse systems are rarely encountered. Catalyst particles for example usually cover a certain range of diameters rather than a single size, and even then the particles may break due to attrition in the fluidised bed reactor. In other processes particles may change their size due to physical processes or chemical reactions, causing a wide range of sizes to be present in the reactor.

The influence of this polydispersity on the drag force is difficult to measure experimentally, in particular when the drag force on individual particles is considered. Literature data are usually limited to measurements of the overall pressure drop over a polydisperse system or indirect data such as measurements of the settling velocities in mixtures (see also section 2.6). Methods that are capable of measuring the drag force on individual particles have been developed but are limited to dilute systems consisting of very few particles (see e.g. Liang et al., 1996), that cannot form a good representation of a polydisperse system. Therefore, computer simulations such as the lattice-Boltzmann method are a very important tool in the study of bi- and polydisperse systems, since this is one of the only methods which can provide information on the drag force for individual particles in arbitrary systems, where the only limitation is the available computer capacity.

The parameter space in polydisperse systems is infinitely large, since the number of particle species, diameter ratios, distribution widths around an average diameter and mixture composition are all variables, apart from the porosity and Reynolds number. Therefore, this study is limited to bidisperse systems with a diameter ratio between 0.25 and 0.7. Lower diameter ratios are not often encountered in industrial applications. In section 5.5 the results of simulations of one polydisperse system, consisting of four particle species, will be presented.

5.2 Bidisperse systems

In the bidisperse simulations the number of particles ranged from 64 to 1000, depending on the diameter ratio and the mixture composition. In the case

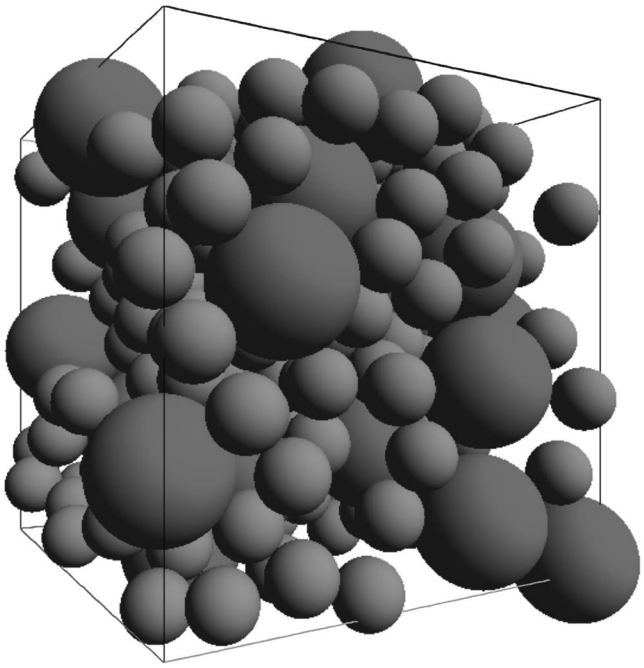

Figure 5.1: Example of a bidisperse system as studied in the LBM-simulations. $N_1 = 192$, $N_2 = 24$, $d_1/d_2 = 0.5$ lattice sites, $\varepsilon = 0.5$, $\phi_1 = \phi_2$.

of extreme diameter ratios (e.g. 1:4), the number of large particles becomes very low if the total number of particles is not sufficiently large. A minimum of 12 large particles was used for each system. Another problem was that the diameter of the small particles in some cases had to be very small (in some cases as low as 6.4 lattice sites) in order to keep the total system volume and thus the calculation time within reasonable limits. Therefore it is essential to use the extrapolation to correct for the finite size effect, as described in section 3.4.4.

All particle configurations were obtained through a Monte Carlo procedure as described in section 3.4.1. Figure 5.1 shows a typical example of the systems that were studied. The system shown here consists of 216 particles, of which 192 are small and 24 larger with a diameter ratio of 1:2. The volume fractions of both particle types are thus equal, and the overall porosity is $\varepsilon = 0.5$.

Figure 5.2 is a cross-section of the flow through the same system. Like in

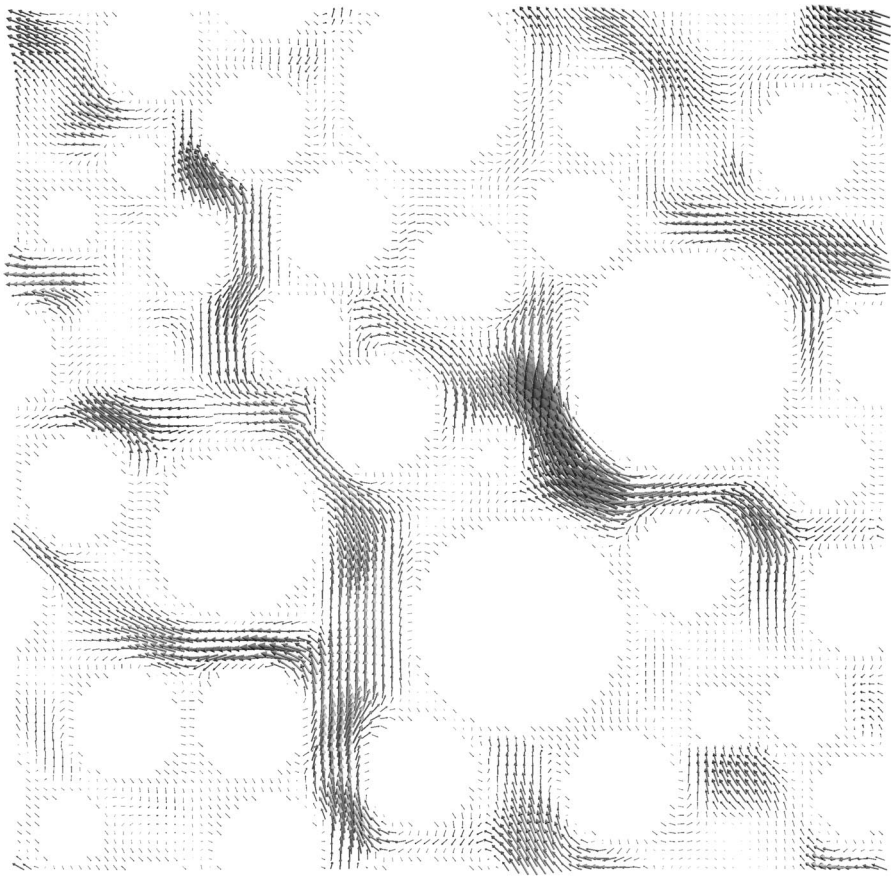

Figure 5.2: Cross-section of flow through the bidisperse system in figure 5.1 during lattice-Boltzmann simulation.

figure 4.2 the arrows point in the direction of the flow, while their length and thickness indicate the magnitude of the flow. Similar to the flow through a monodisperse system (see figure 4.2), no-slip conditions apply at the particle boundaries and larger fluid velocities prevail in regions with a high local porosity (large pores).

5.3 Low Reynolds numbers

In section 4.2 we found a new relation for the drag force in monodisperse systems at low Reynolds numbers, as a function of the porosity. Section 2.6 showed that this relation might also be valid to determine the overall pressure drop over a bi- or polydisperse system when the average particle diameter $\langle d \rangle$ (see equation (2.16)) is used instead of the diameter d, at least in the porosity range where the Kozeny-Carman equation is valid ($\varepsilon < 0.6$). In section 2.6.3 a new relation for the drag force on individual particles in polydisperse systems was derived in the form of a correction factor on the drag force in monodisperse systems (equation (2.56)), which results in the correct form of the Kozeny-Carman equation when the pressure drop over the entire system is calculated. The Kozeny-Carman relation is valid only at low Reynolds numbers and at low porosities; equation (2.56) is not necessarily valid under other circumstances. Therefore, we will check the validity of this equation first for low Reynolds numbers.

The results from the lattice-Boltzmann simulations for the drag force on individual particles (averaged over all particles of the same type) and the average drag force at low Reynolds numbers, calculated according to the method described in section 3.4.4, are given in table A.3 in appendix A. In figure 5.3 the results for the average drag force $\langle F \rangle$ are plotted together with the results for the drag force F in monodisperse systems (see section 4.2 and table A.1) and compared to equation (4.1). The agreement is excellent, which proves that the average drag force and thus the overall pressure drop over a bidisperse system can indeed be calculated with equation (4.1), replacing d with $\langle d \rangle$, for all porosities in the low Reynolds number regime.

The scatter in the data from binary systems is larger than the scatter in the monodisperse data, which is probably due to the lower number of configurations over which the data were averaged due to the limited computational resources (in most cases only five configurations were used, where this was up to thirty for the monodisperse simulations). Apart from this, the number

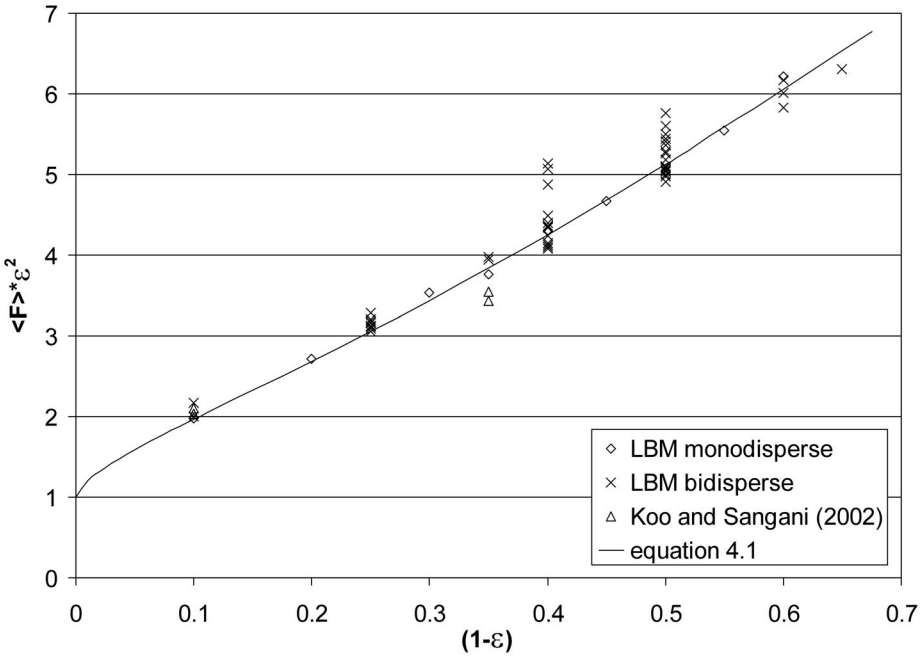

Figure 5.3: Average normalised drag force in bidisperse systems as a function of packing fraction, compared to monodisperse simulation data and equation (4.1).

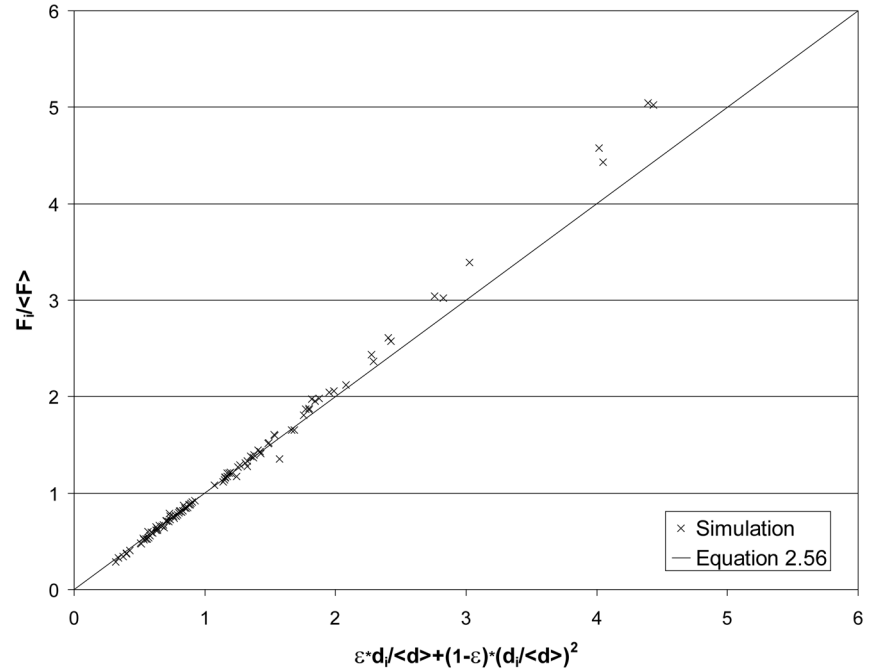

Figure 5.4: Normalised drag force on individual particles in bidisperse systems at low Reynolds numbers from LBM-simulations, compared to equation (2.56).

of large particles in each configuration was often (much) smaller than the number of particles in a monodisperse simulation, although the total number of particles was larger in all cases. The largest deviations were found for the most extreme diameter ratio ($d_1/d_2 = 0.25$), where the maximum deviation from equation (4.1) reached a value of almost 21%. In cases with less extreme diameter ratios (i.e. $d_1/d_2 \geq 0.5$) the maximum deviation from equation (4.1) of the simulation results was only 5.4%.

Equation (2.56) presented a relation for the ratio of the drag force acting on an individual particle in a mixture to the drag force on the same particle in a monodisperse system with equal porosity and Reynolds number, F_i/F_{mono}. From figure 5.3 it can be seen that expression (4.1) for the drag force in a monodisperse system is close to the average drag force in the simulation $\langle F \rangle$. Normalisation by this latter value has the advantage that the comparison to equation (2.56) is not influenced by deviations of the average drag force

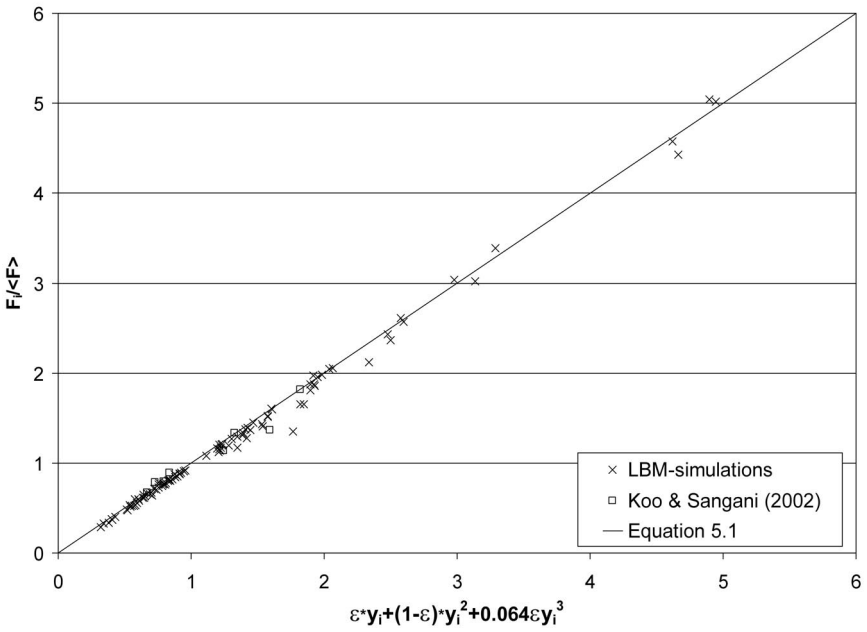

Figure 5.5: Normalised drag force on individual particles in bidisperse systems at low Reynolds numbers from LBM-simulations, compared to equation (5.1).

from equation (4.4). Apart from this, the correction factor is not limited to the drag model of equation (4.4) only.

The drag forces on individual particles in a binary mixture, normalised by the average drag in a simulation, are compared to equation (2.56) in figure 5.4. The results match equation (2.56) very well when $y_i < 1.4$ (remember that y_i is defined as $d_i / \langle d \rangle$). When y_i is outside of this range the deviation is larger but systematic. To correct for this an extra term was added to equation (2.56), giving:

$$F_i = \left(\varepsilon y_i + (1-\varepsilon)\, y_i^2 + 0.064 \varepsilon y_i^3 \right) F_{\text{mono}} \,, \tag{5.1}$$

for which the average deviation in all simulations becomes 4.4 %. The maximum deviation of 23 % occurs only in a simulation with a very high porosity, $\varepsilon = 0.9$. If simulations with this high porosity are ignored, the average deviation is only 4.2 %. These results are shown in figure 5.5.

5.4 High Reynolds numbers

The drag force obtained from lattice-Boltzmann simulations in bidisperse media at intermediate and high Reynolds numbers is presented in table A.4 in appendix A. Simulations were done for three values for the average Reynolds number (i.e. the Reynolds number based on the average diameter, $\langle Re \rangle = \rho U \langle d \rangle / \mu$), namely $\langle Re \rangle = 10$, 100 and 500. The average drag forces are plotted as a function of the average Reynolds number in figure 5.6, where they are compared to the drag force in monodisperse media and equation (4.4). The deviation of the results from this equation is on average 4.8 %. Figure 5.6b provides a closer look into the intermediate Reynolds regime. The largest deviations from equation (4.4), which can be up to 24 % in case of extreme diameter ratios ($d_1/d_2 = 0.25$), are found in this range. In most simulations however the errors are less than 5 %.

In figure 5.7 the single particle drag forces from all high Reynolds number simulations are presented. The ratio of the individual drag forces to the average drag force in the simulation is shown as a function of the correction factor $\left(\varepsilon y_i + (1-\varepsilon)\, y_i^2 + 0.064\varepsilon y_i^3\right)$. We find that also for these Reynolds numbers the data points collapse onto the straight line with slope equal to one, which leads to the conclusion that equation (5.1) is equally valid at intermediate and high Reynolds numbers as in the low Reynolds number regime. This is to some extent remarkable, since equation (5.1) was derived within the framework of the Darcy- and Kozeny-Carman equations, which are only valid for low Reynolds numbers. It is stressed that the average drag force $\langle F \rangle$ should be calculated using the *average* Reynolds number $\langle Re \rangle$ and not the Reynolds number of the individual particle Re.

5.5 Polydisperse system

The previous sections revealed that equation (2.56), that was derived from theoretical considerations, forms a good approximation of the drag force on individual particles in bidisperse systems. The best fit to the simulation results is given by the same equation with an extra term as shown in equation (5.1), where the extra term in all cases is less than 15 % of the total correction factor to the monodisperse drag force. However, the form of equation (2.56) as well as its derivation suggest that it is valid for polydisperse systems as well. To test this assumption a limited study of the

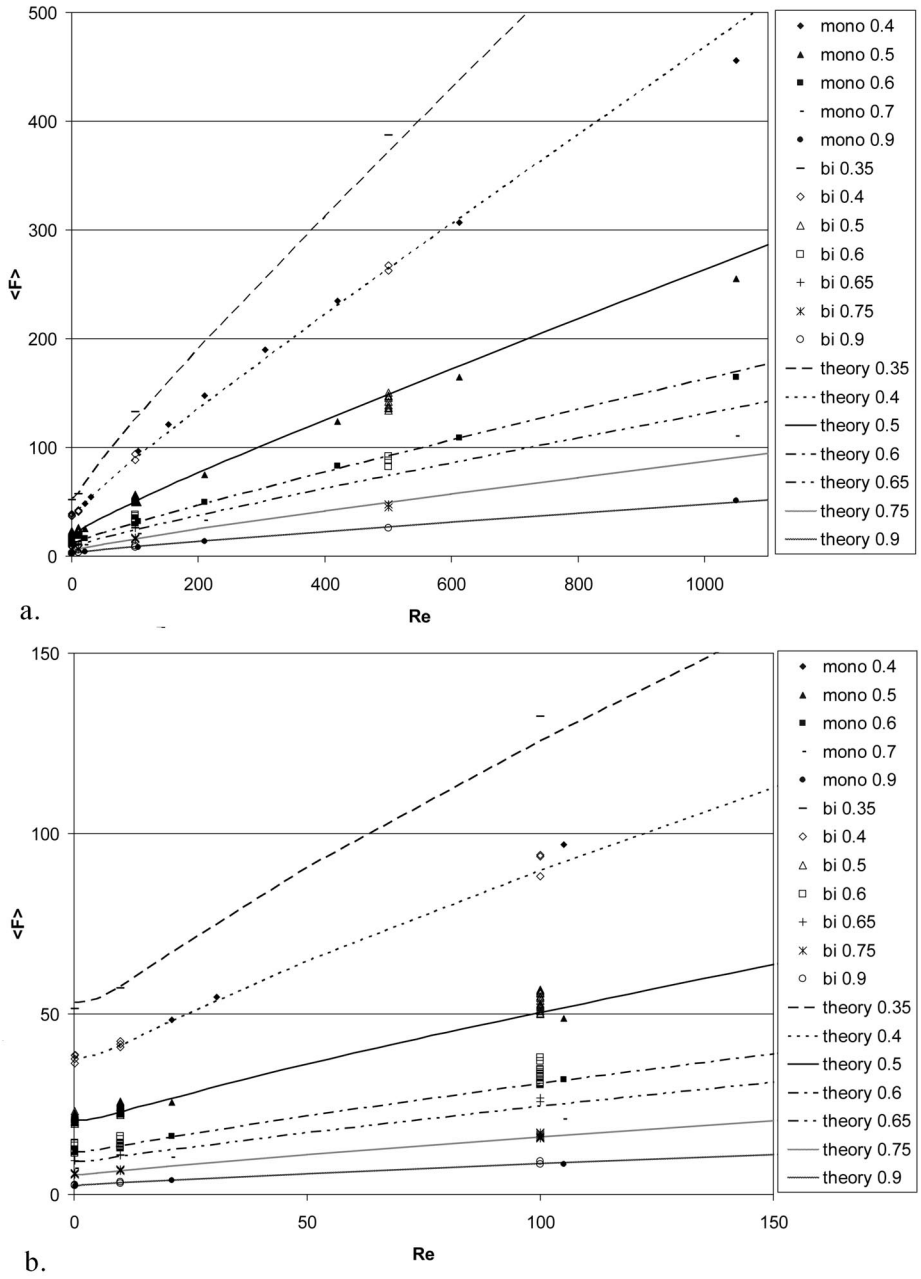

Figure 5.6: a. Average normalised drag force in bidisperse systems as a function of Reynolds number, compared to monodisperse simulation data and equation (4.4). b. Close up of the intermediate Reynolds number area.

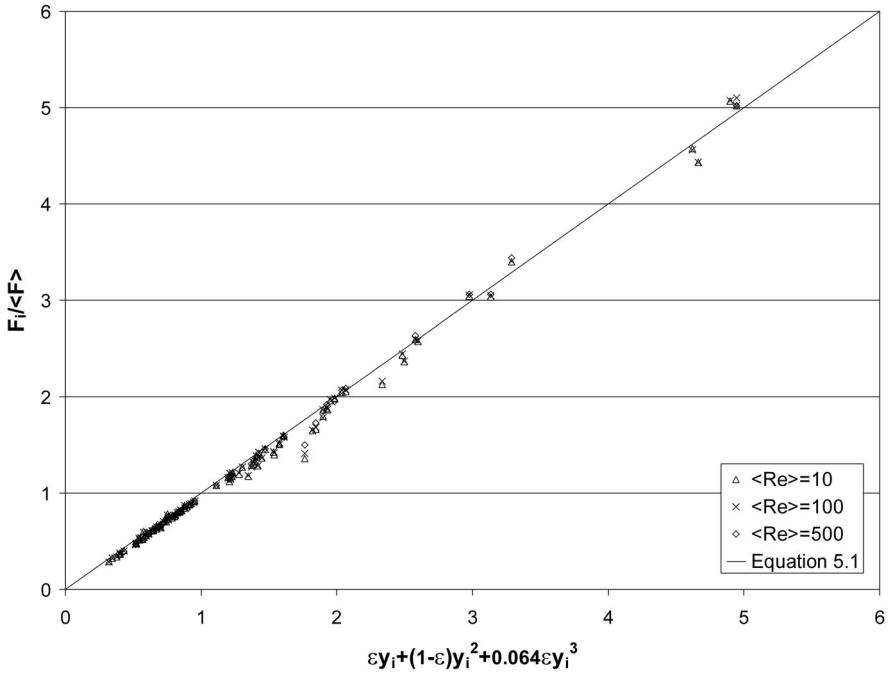

Figure 5.7: Normalised individual drag force in bidisperse systems at high and intermediate Reynolds numbers compared to equation (5.1).

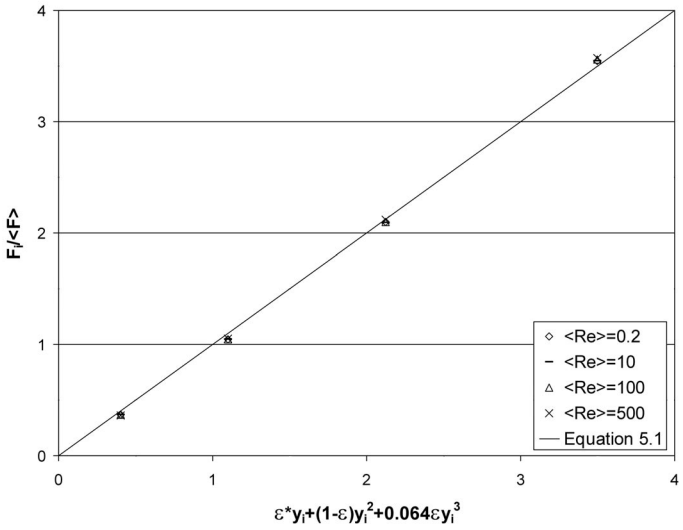

Figure 5.8: Normalised drag force on individual particles in a polydisperse system, compared to equation (2.56).

drag force in polydisperse systems was performed. As the parameter space in polydisperse systems is infinitely large, the simulations were limited to a single mixture, which consisted of four particle species with diameter ratios $1 : 2 : 3 : 4$, present in equal volumes at an overall porosity of $\varepsilon = 0.5$. The simulation setup and analysis of the results were similar to those in simulations of bidisperse systems and are described in section 3.4.

The results for the individual and average drag forces are presented in table A.5. The average drag forces agree reasonably well with the expected values from equation (4.4), with a maximum deviation of 6.2 %. The individual drag forces, normalised by the average drag force, are compared to equation (5.1) in figure 5.8. Again, a good agreement is found, with an average deviation of 4.0 % and it is therefore expected that that the correction factor given by equation (5.1) is indeed valid in polydisperse systems as well, although more elaborate simulations are required before any definite conclusions can be drawn.

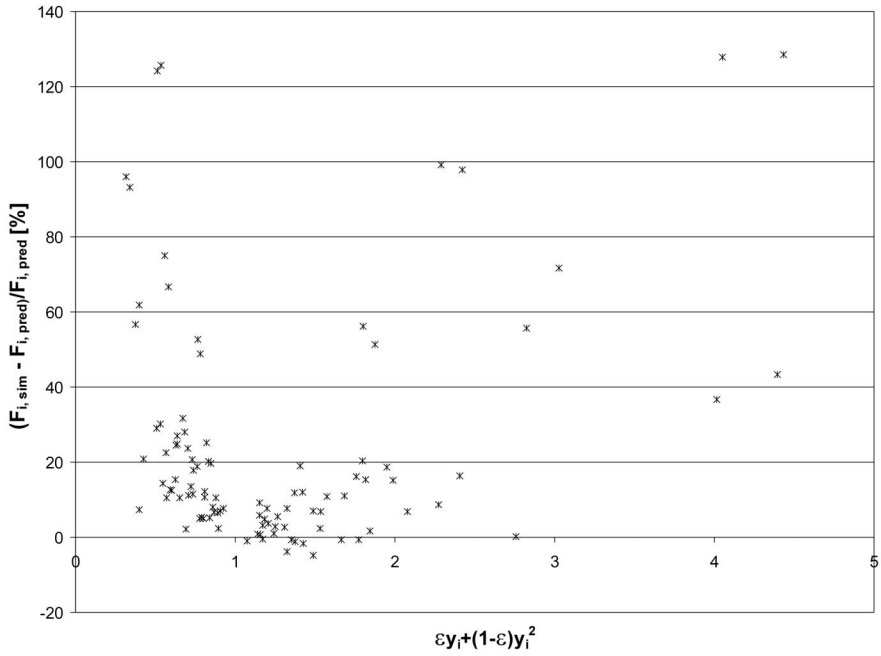

Figure 5.9: Relative deviation between the simulation values for F_1 and F_2 and the predictions with the Patwardhan and Tien model in combination with equation (4.4).

5.6 Discussion

In figures 5.3 and 5.5 the simulation results of Koo and Sangani (2002), obtained from multipole expansion simulations for two porosities ($\varepsilon = 0.65$ and 0.9) and two size ratios ($d_1/d_2 = 0.5$ and 0.7), are also shown. This is to the author's knowledge the only data for the drag force on individual particles in binary mixtures that were measured directly in simulations. The average drag force is somewhat too low in the simulations with $\varepsilon = 0.65$ compared to equation (4.1). The ratio of the individual particle drag forces to the average drag force matches the lattice-Boltzmann data and equation (5.1) very well.

The simulation results are also compared to the theory of Patwardhan and Tien (1985) for the drag force on particles in a mixture, that was described in section 2.6. The individual particle porosity is calculated according to equation (2.51) and subsequently used in equation (4.4). Figure 5.9 shows

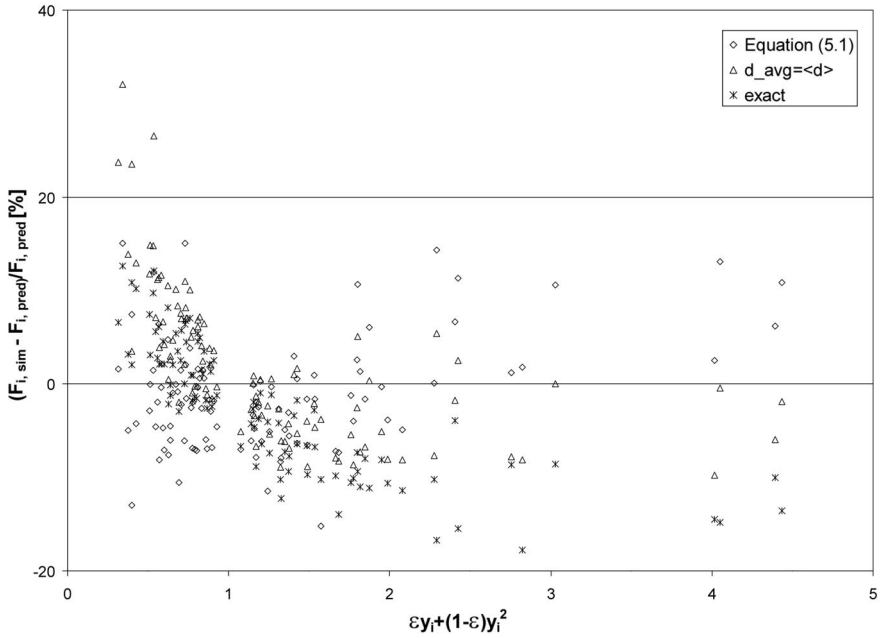

Figure 5.10: Relative deviation between the simulation values for F_1 and F_2 and the predictions with equation (5.1) and the adjusted Patwardhan and Tien models in combination with equation (4.4). The triangles represent predictions where the average diameter in the calculation of δ is presumed to be equal to $\langle d \rangle$, the stars show the deviations when the cubic equation for δ is solved exactly.

the relative deviation of the simulation results at low Reynolds numbers from predictions made with this theory. The original model as it was proposed by Patwardhan and Tien (1985), where the average diameter in the calculation of δ is defined as $d_{avg} = \sum \chi_i d_i$, results in errors of more than 100 %, especially in situations with extreme diameter ratios or low porosities. This is significantly improved when using $d_{avg} = \langle d \rangle$, and even more so with the exact value for δ as shown in figure 5.10. This figure also shows values for the deviation of the simulation results from predictions that are calculated using the new drag model (equation (4.1)) with the correction factor (equation (5.1)). For simulations at high Reynolds numbers the Patwardhan and Tien model performs well if the average Reynolds number $\langle Re \rangle$ is used in equation (4.4) and not the particle Reynolds number Re_i, which is shown in figure 5.11 for the simulations with $\langle Re \rangle = 500$. The exact solution for δ was used to calculate the values in this figure. The performance of the Patwardhan and Tien model in this case is comparable to that of equation (5.1).

In the lattice-Boltzmann simulations the same value was used for the difference between d_0 and the effective hydrodynamic diameter for all particles in a simulation, whereas in principle this should have a different value for different diameters (see section 3.3). The value that was used was the average value of $d_{\text{eff}} - d_0$ of all the particles in the system, which introduces a minor error in all particle diameters in the simulation, and thus in the system porosity. The deviation in the porosity could reach a deviation of about 1% from the desired value, which could partly explain the large deviations of the average drag force in binary simulations from equation (4.4). For one of the most severe cases test simulations were performed where the particles were initialised using d_0 instead of d_{eff}. The results obtained revealed that the deviations from equation (4.4) decreased from 9.1 to 5.9 % in the low Reynolds regime, and from 12.7 to 10.2 % for $\langle Re \rangle = 100$. The ratios $F_i / \langle F \rangle$ were not influenced by the new definition.

For the comparison of the individual particle drag forces to equations (2.56) and (5.1) $F_{\text{mono}} = \langle F \rangle$ was used with $\langle F \rangle$ calculated from the simulation results. This was chosen because it gives the most objective view about the validity of the correction factor for polydispersity. However, when using the new equation in CFD-simulations or other calculations, the average drag force is obviously not known a priori, and has to be calculated from equation (4.4). The error in this calculation will then add to the error introduced by equation (5.1). The average deviation from equation (5.1) increases slightly when the calculated value of $\langle F \rangle$ is used, in general less than 1 %, although

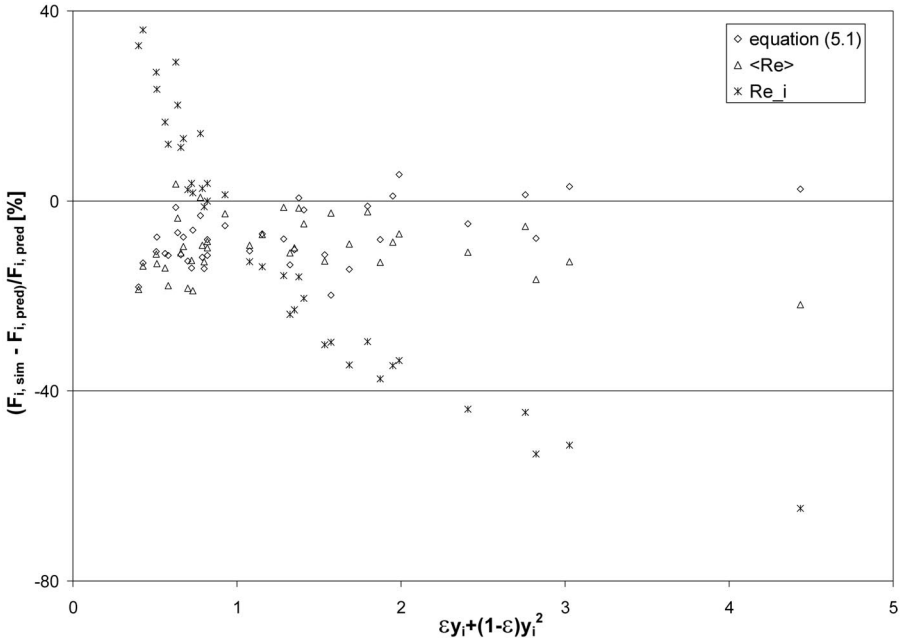

Figure 5.11: Relative deviation between the simulation values for F_1 and F_2 and the predictions with equation (5.1) (diamonds) and the adjusted Patwardhan and Tien models in combination with equation (4.4) for the simulations at $\langle Re \rangle = 500$. The triangles and stars represent the PT-model using the average Reynolds number and the particle Reynolds number, respectively.

for $\langle Re \rangle = 500$ the average deviation was doubled from 4.1 % to 8.4 %.

In the derivation of equation (2.56) it was stated that the Kozeny-Carman relation for the overall pressure drop is retrieved when F_i/F_{mono} is first or second order in y_i. The extra term in equation (5.1) however, is third order in y_i. This influences the pressure drop over a polydisperse system compared to the pressure drop for a monodisperse system with the same porosity, Reynolds number and $d = \langle Re \rangle$ as follows:

$$\nabla P_{\text{poly}} = \nabla P_{\text{mono}} \frac{d^2}{\langle d \rangle^2} \left(1 + 0.064(1-\phi) \sum_i \chi_i y_i \right) . \tag{5.2}$$

The pressure drop over a polydisperse system is thus predicted to be slightly higher than the pressure drop over a monodisperse system with $d = \langle d \rangle$. Figures 5.3 and 5.6 are not conclusive about this.

It is also possible to find a correction term to equation (2.56) that consists only of first and second order terms and thus does not effect the overall pressure drop compared to monodisperse systems. An equation that gives very good results is:

$$F_i = \left(\varepsilon y_i + (1-\varepsilon)\, y_i^2 + 0.22\,(1-\varepsilon) \left(y_i^2 - y_i \right) \right) F_{mono} . \tag{5.3}$$

The average deviation of $F_i / \langle F \rangle_{\text{sim}}$ from this equation is less than 2 %. The deviations in F_i/F_{mono} are slightly larger, on average $5-6$ %. The differences are most pronounced for low values of y_i, where the simulation values are often lower than the values predicted by equation (2.56). With equation (5.1) this deviation becomes stronger, whereas the extra term in equation (5.3) actually decreases the difference.

An interesting observation can be made when examining the effect of equation (2.56) in a mixture with a Gaussian-type size distribution of the diameters. When the diameter distribution has a width σ around $\bar{d}$, the average diameter $\langle d \rangle$ is readily evaluated as:

$$\langle d \rangle = \frac{3\sigma^2 \bar{d} + \bar{d}^3}{\sigma^2 + \bar{d}^2} . \tag{5.4}$$

Inserting this equation into equation (2.15) for the pressure drop shows that:

$$\nabla P_{poly} = \nabla P_{mono} \left(\frac{(\sigma/d)^2 + 1}{3\,(\sigma/d)^2 + 1} \right)^2 , \tag{5.5}$$

where the correction term of equation (5.1) is neglected. Equation (5.5) thus shows that the pressure drop decreases when the polydispersity increases. This could be one of the causes of the discrepancy in the low Reynolds number regime between the Ergun equation ($k = 150/18$) and the Kozeny-Carman equation ($k = 180/18$), as Ergun (1952) performed his experiments using crushed porous solids of a certain diameter range, instead of truly monodisperse particles. The pressure gradient is reduced by a factor 0.833 (150/180) when $\sigma/\delta = 0.22$, which is probably more than in the experimental systems of Ergun. However, there may be other factors in the experimental system which could cause a deviation with the drag force measured in the simulations. Typically one would think of non-homogeneity of the system and non-sphericity of the particles.

5.7 Conclusions

The lattice-Boltzmann simulations showed that equation (4.1) predicts the average drag force over a bi- or polydisperse bed at low Reynolds numbers with an average deviation of less than 5 %, where higher deviations were found in cases with extreme diameter ratios or very high porosities. At higher Reynolds numbers, equation (4.4) provides a good estimate.

The simulation data for the drag forces experienced by individual particles are substantially different from the drag forces that these particles would experience in a monodisperse bed of the same porosity and Reynolds number. The simulation results showed that the difference may be up to a factor of 5 in case of a diameter ratio $d_1 : d_2 = 1 : 4$. The data were compared to equation (2.56) that was derived on purely theoretical grounds in the Kozeny-Carman regime, and that proved to be a reasonable approximation at all porosities and Reynolds numbers with maximum errors up to 15 %. To obtain the best fit through the simulation data an extra term was added in equation (5.1). With this equation, the deviations between $F_i/\langle F \rangle$ in the simulations and the predicted values are on average less than 5 %.

The model of Patwardhan and Tien (1985) performs as good as the new relation when the average diameter in the original simulation is replaced by the exact solution of the cubic equation for δ. However, solving a cubic equation during every calculation requires much more effort than using equation (5.1), and therefore the latter equation may be preferred over the Patwardhan and Tien model. A good compromise is the use of $\langle d \rangle$ for the average

diameter in the Patwardhan and Tien model, in which case the deviations are only slightly larger than with the exact δ.

Chapter 6

Validation

Abstract

Pressure drop measurements were performed in a packed bed, filled with monodisperse or bidisperse spherical particles, to validate the drag relations that were derived in the previous chapters. For monodisperse systems at low Reynolds numbers, the differences between the experimental pressure drop and the theoretical predictions are on average 5.5 %. *The average deviation from theory in bidisperse experiments is of the same order,* 5.2 %. *At intermediate Reynolds numbers the deviations from theory are considerably larger, on average* 24 %, *and seem to be systematic. It seems likely that a systematic error was made in either the porosity or the viscosity in the experiments. At higher Reynolds numbers the deviations from theory decrease, for* $Re > 325$ *they are all less than* 5 %. *The drag force on individual particles could not be measured, and the validity of the new relation in dilute systems has not been tested either.*

Discrete Particle Simulations of (i) *a single bubble injected into an incipiently fluidised bed and* (ii) *a segregating mixture were performed with different drag models, grid sizes and boundary conditions. All computational results were compared to experiments. The single bubble simulations revealed that a fine grid gives more realistic results. Furthermore, usage of the Ergun drag closure leads to an overprediction of the bubble size, although no definite conclusion as to what is the best drag model could be drawn. The segregation simulations showed that the new drag relation with*

the correction for bidispersity predicts the experimentally observed segregation rate most accurately.

Calculation of the inversion velocity of mixtures showed that the new drag model with the correction for polydispersity gives reasonable values and also the correct trend when the composition of the mixture is changed, this in contrast to several models that have been proposed previously in literature.

6.1 Introduction

In chapter 4 a new drag force relation was presented (equation (4.4)), that was derived from lattice-Boltzmann simulations of fluid flow through random arrays of monodisperse spheres. In chapter 5 two main observations were made: (*i*) the average normalised drag force in bi- and polydisperse arrays can be described by the same equation as for a monodisperse system at the same porosity; (*ii*) the normalised drag force on individual particles differs markedly from drag formulations in monodisperse systems, which are currently used in CFD-modelling and engineering applications. In this chapter a partial experimental validation of the LBM-generated drag closures will be presented. In section 6.2 the results of pressure drop experiments are presented to validate the first observation, since the pressure drop is directly related to the average drag force in a packing. The drag force on a single particle however is difficult to measure experimentally, and the methods that do exist are very laborious and limited to single particles or particles with very few surrounding particles (see e.g. Liang et al., 1996; Zhu et al., 2003; Katoshevski et al., 2001). These systems are not representative of a random (bidisperse) system of certain porosity and are therefore not suited to validate equation (5.1). However, an indirect validation of the prediction for the individual drag force can be obtained by comparing simulation data for segregating fluidised beds with experiments. This will be presented in section 6.3.

The validity of equations (4.1) and (4.4) in dilute systems has not yet been verified experimentally. Major difficulty with experiments in dilute systems is that the particles have to be fixed to their (random) position. This will be the subject of future research.

6.2 Experimental validation: pressure drop in a random close packed bed

6.2.1 Experimental setup

A schematic representation of the experimental setup is shown in figure 6.1, and a photograph in figure 6.2. The setup consists of a cylindrical column of inner diameter $D = 80.0$ mm and length $L = 300.0$ mm, placed in a

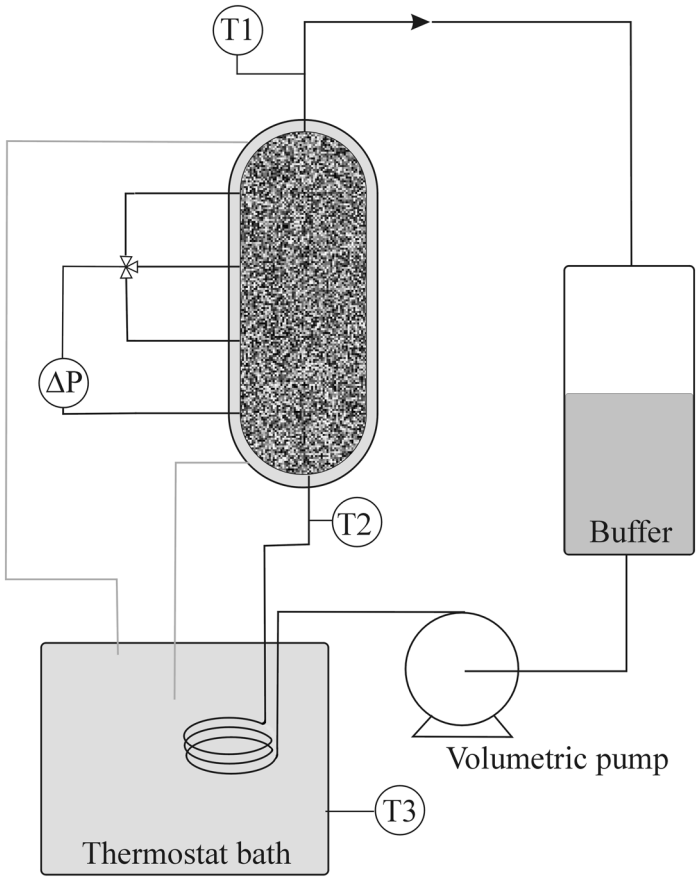

Figure 6.1: Schematic representation of the experimental setup.

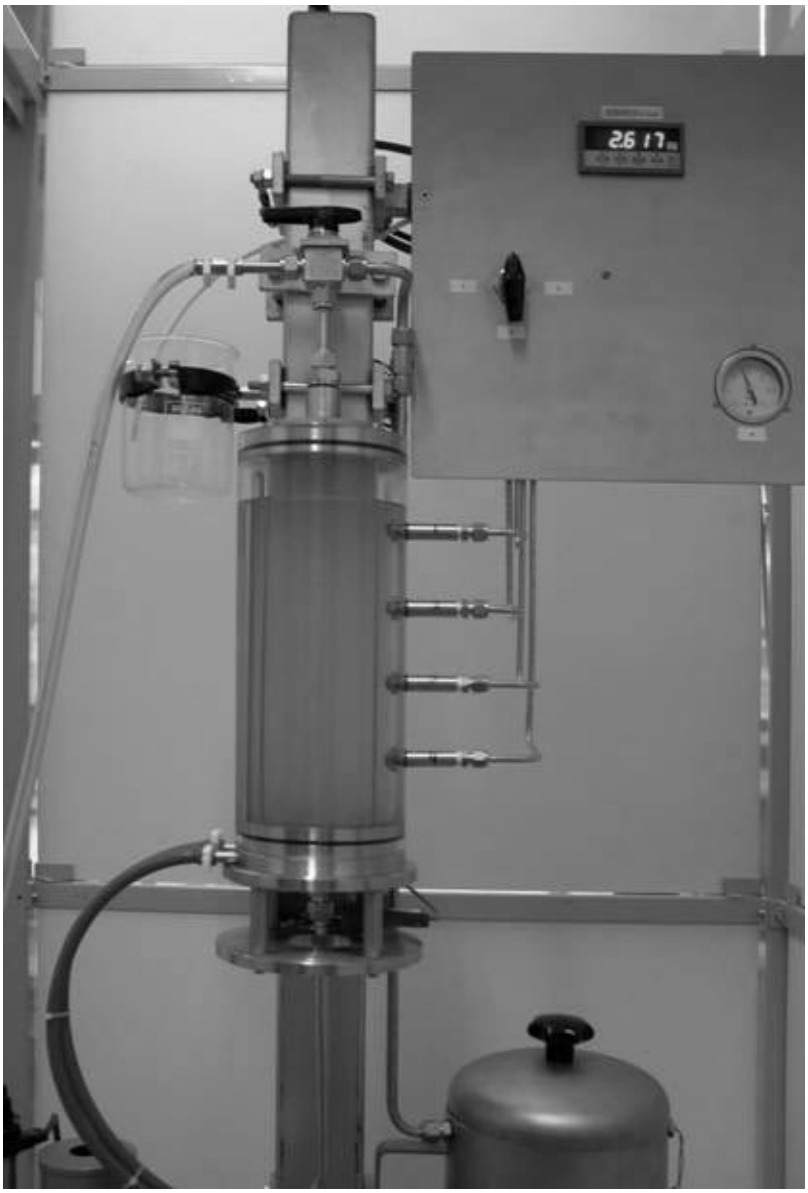

Figure 6.2: Photo of (part of) the experimental setup.

jacket through which water was flowing in order to keep the temperature (which strongly effects the viscosity of the percolating liquid) constant. A gear pump was connected to the column that circulated liquid through the system with an accurately adjustable pump frequency. In the experiments for low Reynolds numbers glycerin was used, whereas for the higher Reynolds number experiments water was used. The liquid was preheated to the desired temperature of the reactor in a thermostat bath. At four different heights in the wall tubes were placed that were connected to a pressure differential sensor to measure the pressure difference between the lowest measuring point and any of the other three points, which could be selected through a switch. Two pressure differential sensors were used: one with a maximum pressure drop of 5 bar, and a second one with a maximum pressure drop of 175 mbar. Both sensors had an error of 0.04 % of the full scale, thus the errors in the measurements were typically less than 1 % if minimum pressure drops of 200 mbar and 7 mbar were encountered respectively.

The column was filled with monodisperse or bidisperse random packings of spherical glass particles, for which five different diameters were available: 1.0, 1.5, 2.0, 2.5 and 4.0 mm, with standard deviations of less than 2 % for all diameters. The porosity of the packing was determined from the mass of the particles. The viscosity of the glycerin was measured in a capillary and that of the water was calculated from the temperature (test measurements agreed very well with theory). The measured pressure drops were corrected for the static pressure drop.

All experiments were performed two or three times, where the bed was emptied and refilled for each separate measurement, which brought about minor changes in porosity and viscosity for the different sets of data. The averaged data that are presented in the results section were corrected for these differences by use of equation (4.4). The variations in the porosity were less than 0.5 %, which result in corrections to the drag force (by extrapolation) of up to 4 %. The fluctuations in the viscosity were larger as glycerin is very hygroscopic and a small amount of water influences the viscosity strongly. However, this is not expected to form a problem as in the low Reynolds number experiments (for which glycerin was used) the drag force is linearly dependent on the viscosity. The normalised drag force is not influenced by uncertainties in the viscosity in this case, and thus no extra correction is necessary. At higher Reynolds numbers, where the normalised drag force does depend on the viscosity (via the Reynolds number), the uncertainty in the viscosity was less since water was used.

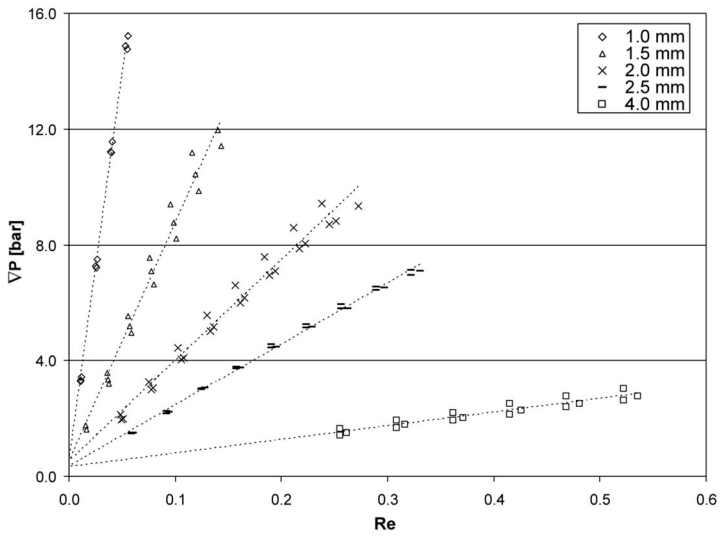

Figure 6.3: Measured pressure drops in experiments with monodisperse beds.

6.2.2 Low Reynolds numbers

Monodisperse systems

Figure 6.3 shows the measured pressure drops over monodisperse systems as a function of the particle Reynolds number. It can be seen that the data obeys Darcy's law very well, that is, the pressure drop is a linear function of the Reynolds number in the low Reynolds number range ($0 < Re < 0.6$), as is predicted by this theory. The intersection with the axis is the static pressure, for which in the remains of this section will be corrected. The standard deviation between measurements with the same particle type is 4.1 % on average, with a maximum deviation of 8.1 %. Part of this deviation can be explained by the variations in porosity and viscosity: when corrected for these effects, the standard deviation in the experiments with the same particle type is reduced to an average value of 2.9 %, with a maximum of 6.0 %. Figure 6.4 shows the average values for the normalised drag forces calculated from the measured pressure drops by use of equation (2.7). Note that in the limit of low Reynolds numbers, the normalised drag force depends only on the packing fraction, and hence not on the particle diameter. The variation in the theoretical values as shown in figure 6.4 is thus

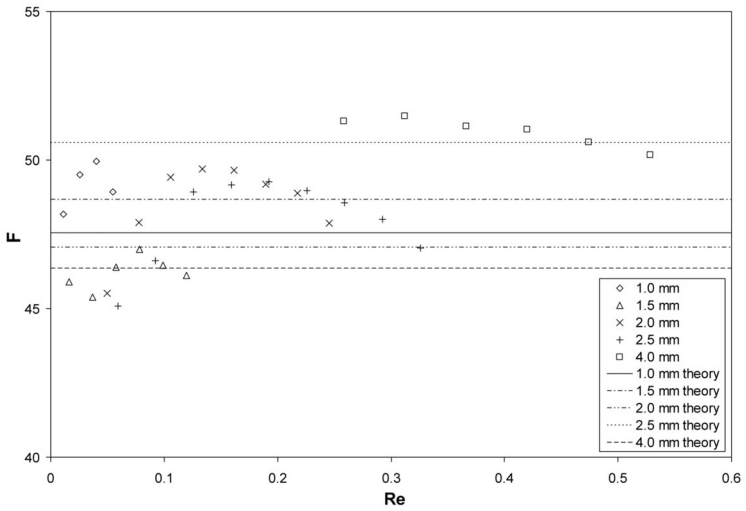

Figure 6.4: Normalised drag forces in experiments with monodisperse beds. The lines are theoretical values calculated from equation 4.1.

entirely due to differences in the packing fraction between the various particle species. Specifically, the packing fractions for the 1.0, 1.5, 2.0, 2.5 and 4.0 mm particles are 0.6338, 0.6371, 0.6323, 0.6426 and 0.6301 respectively. Deviations between the experimental drag force and the theoretical values are on average 5.5 %, where the maximum deviation is 11.1 %. This is within the experimental error, which is about 15 % (see for this calculation appendix B). Deviations on the negative side are found as often as deviations on the positive side, which suggests that the errors encountered here are due to random fluctuations. It can be concluded that the experiments confirm the validity of equation (4.1) for low Reynolds number flow through monodisperse packed beds.

Bidisperse systems

Bidisperse packings were composed from particle mixtures with various diameter ratios ($d_1/d_2 = 0.25$, 0.375, 0.50, 0.625 and 0.75) and compositions, resulting in a total of 17 mixtures with average diameters varying from 1.2 mm to 3.7 mm. Similar to the monodisperse systems, the pressure drops were a linear function of the Reynolds number as shown in figure 6.5. This figure shows typical results for the pressure drops averaged from three mea-

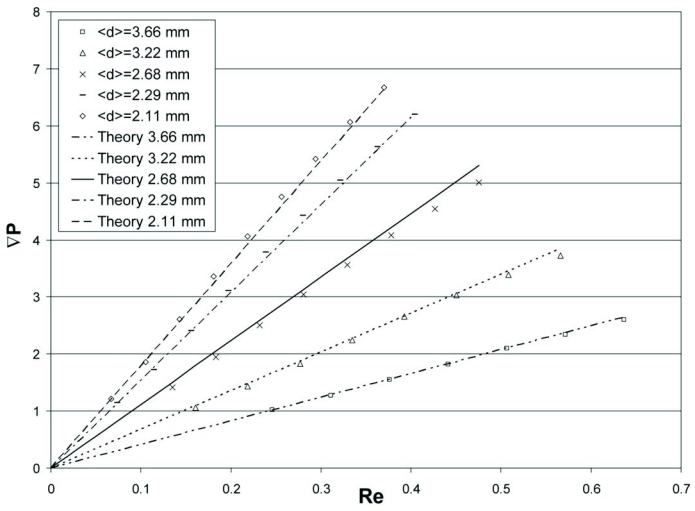

Figure 6.5: Typical example of pressure drop in over a bidisperse packing for mixtures composed from the same particle species (2 and 4 mm) with different compositions.

surements, corrected for static pressure and for small differences in porosity, mixture composition and viscosity. The predictions for the pressure drop, calculated with equation (4.1), over a monodisperse system with the same diameter as the average diameter in the binary system are also shown. The match is excellent, which confirms the results from the simulation that equation (4.1) is valid in bidisperse systems when d is replaced by $\langle d \rangle$, with $\langle d \rangle$ as defined in equation (2.16).

The average standard deviation in all bidisperse experiments at low Reynolds numbers is 3.6 %, with a maximum deviation of 9.0 %. Not surprisingly, this high standard deviation is found in a system with the most extreme diameter ratio, $d_1/d_2 = 0.25$, and a small fraction of the smaller particles, $\chi_1 = 0.25$. The homogeneity of the packing is easily effected in this case.

Figure 6.6 shows the average drag forces calculated from the pressure drop data from figure 6.5. Figure 6.7 shows the same data for mixtures composed of particles with varying diameter ratios but equal volume fractions $\phi_1 = \phi_2$. The average deviation in all experiments (including those not shown here) from the theoretical predictions is 5.2 %, with a maximum of almost 19 %. The highest deviations were found in experiments where a mixture of 1.5 and 4.0 mm particles were used, which suffered from static electricity (when

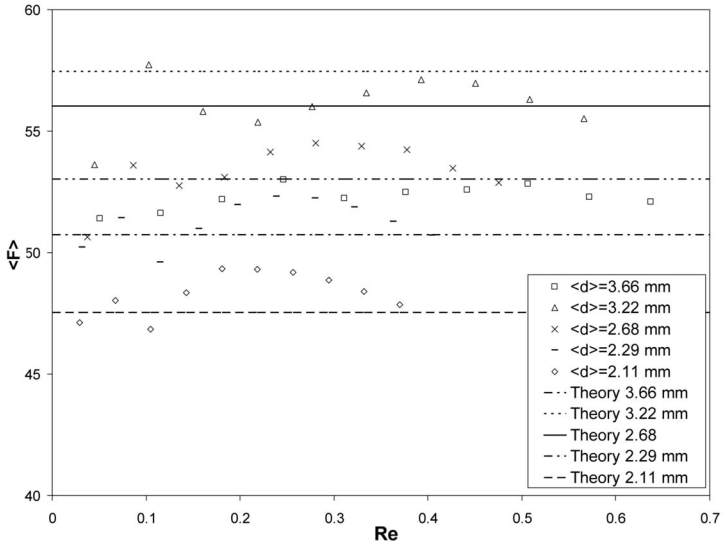

Figure 6.6: Average normalised drag forces in experiments with mixtures of 2 and 4 mm particles in different comppositions. The lines are theoretical values calculated from equation (4.1).

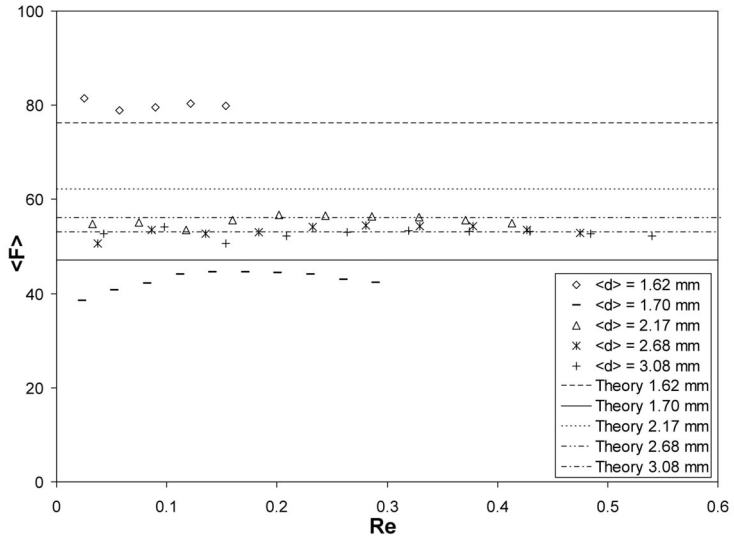

Figure 6.7: Average normalised drag forces in experiments with mixtures composed of different particle species. The lines are theoretical values calculated from equation (4.1).

filling the column) between the plexiglass cilinder and the (coated) small particles, which disturbed the homogeneity severely as the majority of the small particles was found in the wall region. The pressure drop found in these experiments was lower than the theoretical values, which can indeed be expected when the packing is disturbed in the radial direction.

Note that the packing fractions in binary systems are higher than in monodisperse systems, which also explains why the values for the average normalised drag force are much higher. The maximum packing fraction for a random bidisperse system depends on the diameter ratio of the particles and the fraction of the small particles. The packing fractions in the measurements varied from $0.63-0.71$, where this was $0.63-0.64$ for the monodisperse systems. The highest packing fractions that were used in the simulations were 0.6 for monodisperse systems and 0.65 for bidisperse systems.

As shown in equation (5.2) the overall pressure drop in bidisperse systems is slightly different from monodisperse systems when equation (5.1) is used to calculate the drag force on individual particles. However, the effect is less than 1 %, and since the random errors in the experiments are much larger, it is impossible to test this effect with the current drag measurements.

6.2.3 Intermediate and high Reynolds numbers

Figure 6.8 shows that the measured pressure gradients at high Reynolds numbers are no longer a linear function of this Reynolds number, in agreement with equation (4.4).

Figure 6.9 shows the average experimental values for the normalised drag force at intermediate Reynolds numbers. The simulation values in this figure have been corrected for minor differences in porosity and viscosity, as well as for the static pressure drop. The deviation between the experiment and equation 4.4 is on average 24 % for these experiments. These deviations cannot be attributed to random errors in the measurements only (which could add up to 15 % as shown before), since there is clearly a systematic deviation: the measured values are always higher than the theoretical values. There are two possible explanations for this systematic deviation: firstly, they could be due to an error in the fit to the simulation data (equation (4.4)). The simulation data showed a clear deviation from a linear dependence on the Reynolds number in the range $10 < Re < 100$, which proved difficult to capture in the fit. Nevertheless, the deviations in the

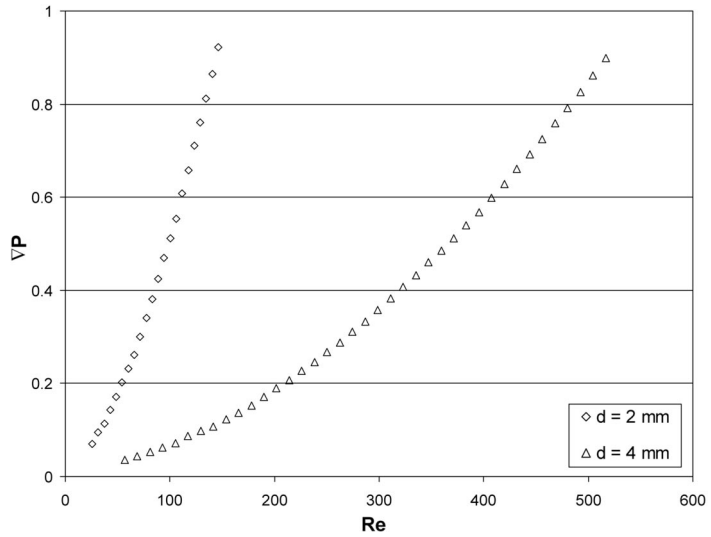

Figure 6.8: Measured pressure gradients in monodisperse experiments at high Reynolds numbers.

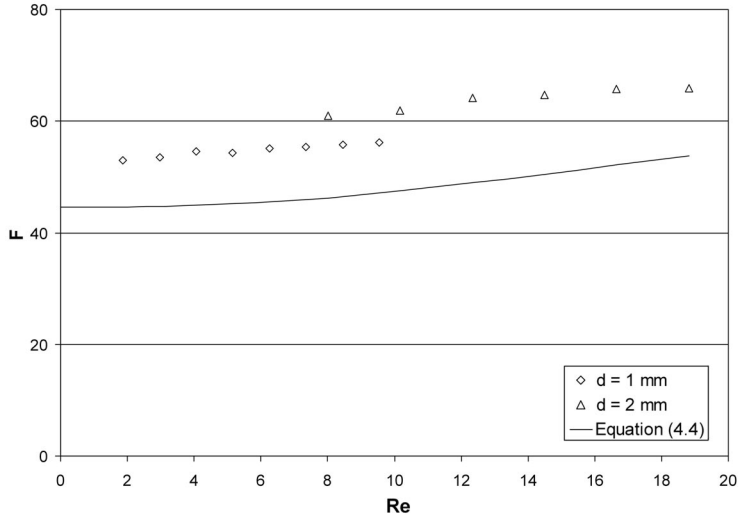

Figure 6.9: Normalised drag forces from pressure drop measurements with monodisperse packings of 1 and 2 mm particles at intermediate Reynolds numbers. The line is the prediction for the drag force from equation (4.4).

simulations from the fit were at most 7.5 %, and never amount to the 24 % found in the experiments. The second possible cause is a systematic error in the experiments, which could be found in two of the variables, namely the porosity or the viscosity. The porosity was determined based on the particle mass in the column. However, the packing fraction in the experiments in figure 6.9 is somewhat lower than that in the low Reynolds number experiments where the same particles are used. It is thus possible that the system had not reached the densest random packing initially and compacted to a lower porosity due to the flow, which would result in a higher pressure gradient. The deviation of the porosity in the monodisperse systems with respect to the low Reynolds number experiments is around 0.0085, which could cause a deviation in the drag force of 12 %. The other variable that could have a systematic error in the measurements is the viscosity. For the measurements with water the viscosity was calculated from the temperature instead of via direct measurement afterwards; this because preliminary measurements agreed with the theoretical values within the accuracy of the measurement. However, if the water was polluted during the measurements, e.g. due to some left-over glycerine in the pump or tubing (although the system was washed several times), the viscosity in the experiments might have been higher than expected. This would also result in a higher experimental value of the pressure drop. Figure 6.10 shows that experiments in bidisperse systems at intermediate Reynolds numbers show the same deviations.

Figure 6.11 shows the experimental results at high Reynolds numbers, compared to equation (4.4). Only monodisperse measurements were done in this regime, with various particle diameters to obtain a larger range for the Reynolds numbers. For intermediate Reynolds numbers the deviations from the theoretical prediction are again considerable; for $Re < 150$ almost all deviations are larger than 12 %, and only at $Re > 325$ they become less than 5 %. In these experiments, the packing fractions were higher than in the intermediate Reynolds number measurements. It is therefore not likely that the deviations from theory in the intermediate Reynolds-regime are caused exclusively by fluctuations in the porosity. An error in the calculated viscosity could still explain the difference with the simulations.

Figure 6.12 compares the experimental results to the expression suggested by Fand et al. (1987), equation (2.34). In the intermediate Reynolds number regime, this forms a better fit to the data than equation (4.4). However, in the high Reynolds-regime the deviation increases, reaching values of up to 17 %. This is remarkable, since the experiments by Fand et al. (1987) are

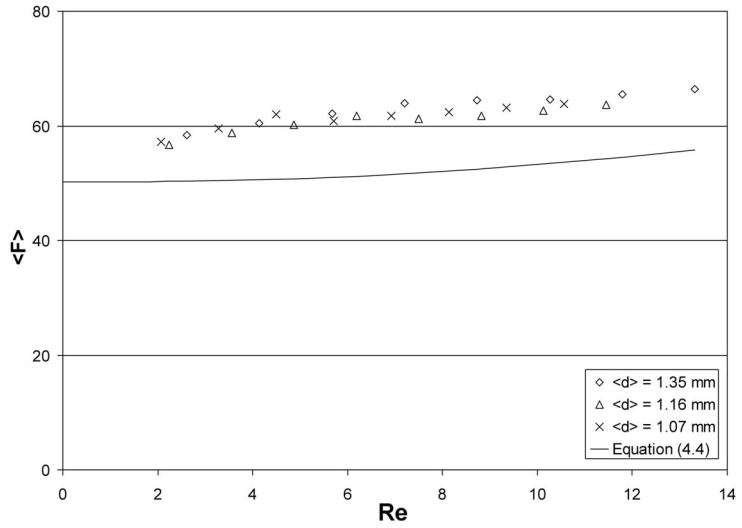

Figure 6.10: Normalised drag forces from pressure drop measurements with bidisperse packings composed of 1 and 2 mm particles in various volume fractions at intermediate Reynolds numbers. The line is the prediction for the drag force from equation (4.4).

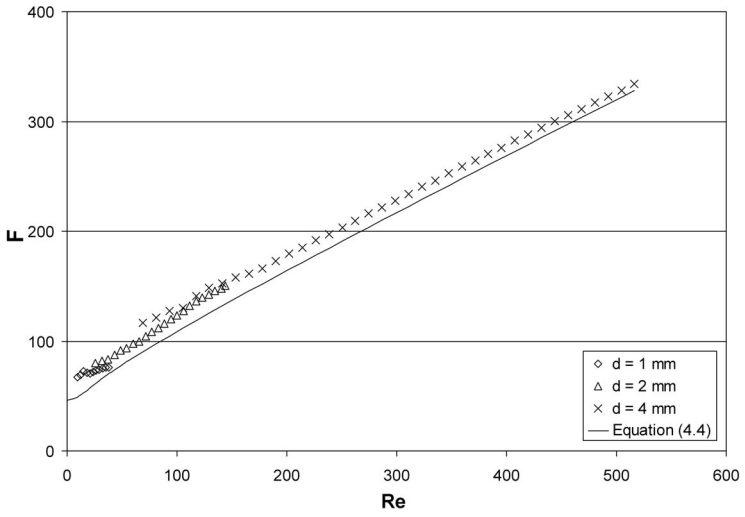

Figure 6.11: Normalised drag forces from pressure drop measurements with monodisperse packings of 1 and 2 mm particles at intermediate Reynolds numbers. The line is the prediction for the drag force from equation (4.4).

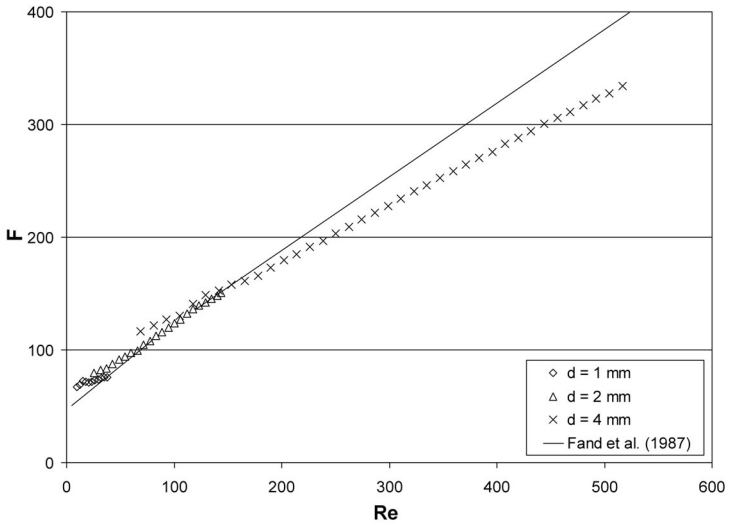

Figure 6.12: Experimental results for high Reynolds numbers compared to the expression by Fand et al. (1987).

very similar to the experiments presented here, and their expression showed very little deviation from their experiments.

6.3 DPM-simulations

One of the reasons to derive the new drag relation, apart from the intrinsic scientific interest, is that drag force closures are a prerequisite in larger scale CFD-models of fluidised beds, like the discrete particle model (DPM) or the continuum model. In this section we present some simulations with the discrete particle model where the effect of the drag model is studied. To this end we performed simulations where the new closures from chapter 4 and 5 are used and simulations using the standard drag models, both of which are compared to experimental results. Two types of experiments were studied: (*i*) the forced formation of a single bubble by injecting a jet in a monodisperse bed that is initially fluidised at minimum fluidisation velocity, and (*ii*) the segregation of a binary mixture in a freely bubbling bed. The first experiment has the advantage that its reproducibility is very high and that random fluctuations in initial particle positions have almost no influence on the results. The second experiment is a very good test case

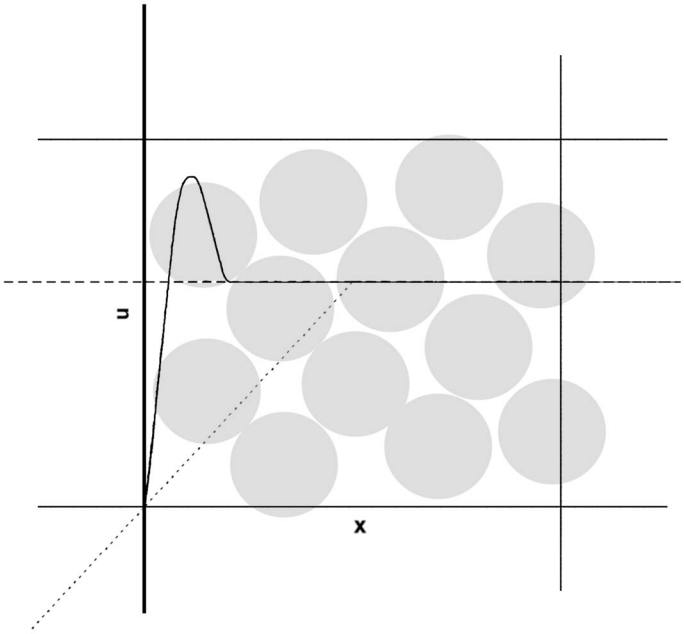

Figure 6.13: Qualitative representation of the gas velocity profile in a computational cell next to the wall in a dense bed. The solid line is the realistic situation; the dotted and dashed lines represent the no-slip and free-slip approximations in the discrete particle model, respectively.

to study the influence of the correction for polydispersity. Previous studies (see e.g. Goldschmidt, 2001a; Bokkers et al., 2004) have shown that it is very difficult to predict segregation rates accurately with CFD-simulations.

Besides the influence of the drag relation, the influence of boundary conditions imposed in the simulations is studied as well. Near a solid wall, the friction with that wall will usually be so large that the fluid acquires the same velocity as the wall. This is called a no-slip boundary condition, which for our situation means that the gas velocity at the bed walls will be zero. Another possibility is that the fluid experiences no friction from a boundary and is thus allowed to move freely along this boundary, which is called free-slip boundary condition. This applies e.g. at a liquid-gas interface, and the velocity gradient at the interface will be zero at equilibrium. In an experimental fluidised bed the gas flow near the walls shows no-slip behaviour. However, this does not mean that this is the obvious choice for

the boundary conditions to be imposed in a DPM-simulation. The boundary layer thickness is typically of the order of one particle diameter, while a computational cell in the discrete particle model usually measures at least 4-10 particle diameters. Besides, wall-channelling prevails in the packed bed which especially becomes important in systems with a relatively small number of particles fitting in the tube in the radial direction (the packing is disturbed by the walls). A qualitative representation of the gas velocity profile near a solid wall is given in figure 6.13. Also shown are the free-slip approximation and no-slip approximation. The best choice of boundary conditions in each simulation will depend on variables like the cell size in relation to particle diameter and the porosity.

6.3.1 Single bubble simulations

An experiment with a very high degree of reproducibility is the formation of a single bubble induced by a gas jet in a bed that is initially fluidised at minimum fluidisation velocity. Bokkers (2005) performed these experiments in a bed with glass particles of 2.5 mm diameter, where a jet with a velocity of 20 m/s was injected from $t = 0$ s until $t = 0.15$ s. The snapshots from our simulations for an identical system will be compared to pictures taken during these experiments. Apart from this, Bokkers (2005) used Particle Image Velocimetry (PIV) to characterise the flow in the experiments; however, the resolution of these measurements is unfortunately not high enough to differentiate between the simulation runs with different drag relations, grid sizes and boundary conditions. In the simulations the same settings were used as in the experiment, where the particle properties such as the coefficient of restitution and friction coefficient were determined experimentally as well. A soft-sphere approach was used for the particle collisions (Hoomans, 1999; Bokkers, 2005), and the gas flow was solved two-dimensionally as the bed has a very small depth. A particle configuration at incipient fluidisation conditions was generated by mixing the particles for a short time at high fluidisation velocity, followed by a relaxation period under minimum fluidisation conditions. The resulting system was subsequently used as the initial configuration in the single-bubble simulations. Details about the experiment and simulations are given in table 6.1.

We performed simulations of this system with three different drag models: firstly, a combination of the Ergun ($\varepsilon < 0.8$) and Wen and Yu ($\varepsilon > 0.8$) equations, as often utilised in literature; secondly, the relation derived from

Table 6.1: Settings in the single bubble experiment and simulations.

Width	0.15 m	
Depth	0.015 m	
Height	0.45 m	
Initial bed height	0.18 m	
Background velocity	1.25 m/s	
Jet velocity	20 m/s	
Jet operation time	$0 - 0.15$ s	
	Coarse grid:	**Fine grid:**
Cells in x-direction	15	30
Cells in y-direction	1	1
Cells in z-direction	45	90
Particle properties		
Diameter	2.5 mm	
Density	2525 kg/m^3	
Coeff. of normal restitution	0.97	
Coeff. of friction	0.10	
Coeff. of tangential restitution	0.33	

Table 6.2: Drag models and boundary conditions in the single bubble simulations.

Run	Drag model	Grid	Boundary
1	Equation (4.4)	coarse	free-slip
2	Equation (4.4)	coarse	no-slip
3	Equation (4.4)	fine	free-slip
4	Equation (4.4)	fine	no-slip
5	Ergun/Wen & Yu	coarse	free-slip
6	Ergun/Wen & Yu	coarse	no-slip
7	Ergun/Wen & Yu	fine	no-slip
8	Hill et al.	coarse	free-slip
9	Hill et al.	coarse	no-slip
10	Hill et al.	fine	no-slip

lattice-Boltzmann simulations by Hill et al. (2001b), and thirdly, equation (4.4). The simulations were done with both no-slip and free-slip boundaries, and two different grid sizes were used. The boundary conditions on the front and back wall were free-slip in all cases, as the gas is solved in two dimensions only.

Results: grid and boundary conditions

Figures 6.14 to 6.18 show snapshots from the experiment and simulations with various boundary conditions and grid sizes. In the beginning of the bubble formation ($t = 0.1$ s) the simulations that use a fine grid seem to produce a bubble that is more spherical, especially near the bubble nose, which agrees better with the experiment. There is no visible difference between free-slip and no-slip conditions. When the bubble starts to collapse, the distinction between the simulations with different grid sizes is even more obvious. The figures show that in the case with small grid cells ($\Delta x = \Delta z = 0.5$ cm) more patterns in the particle configuration can be distinguished and the bubble seems to have broken up into several smaller bubbles (see

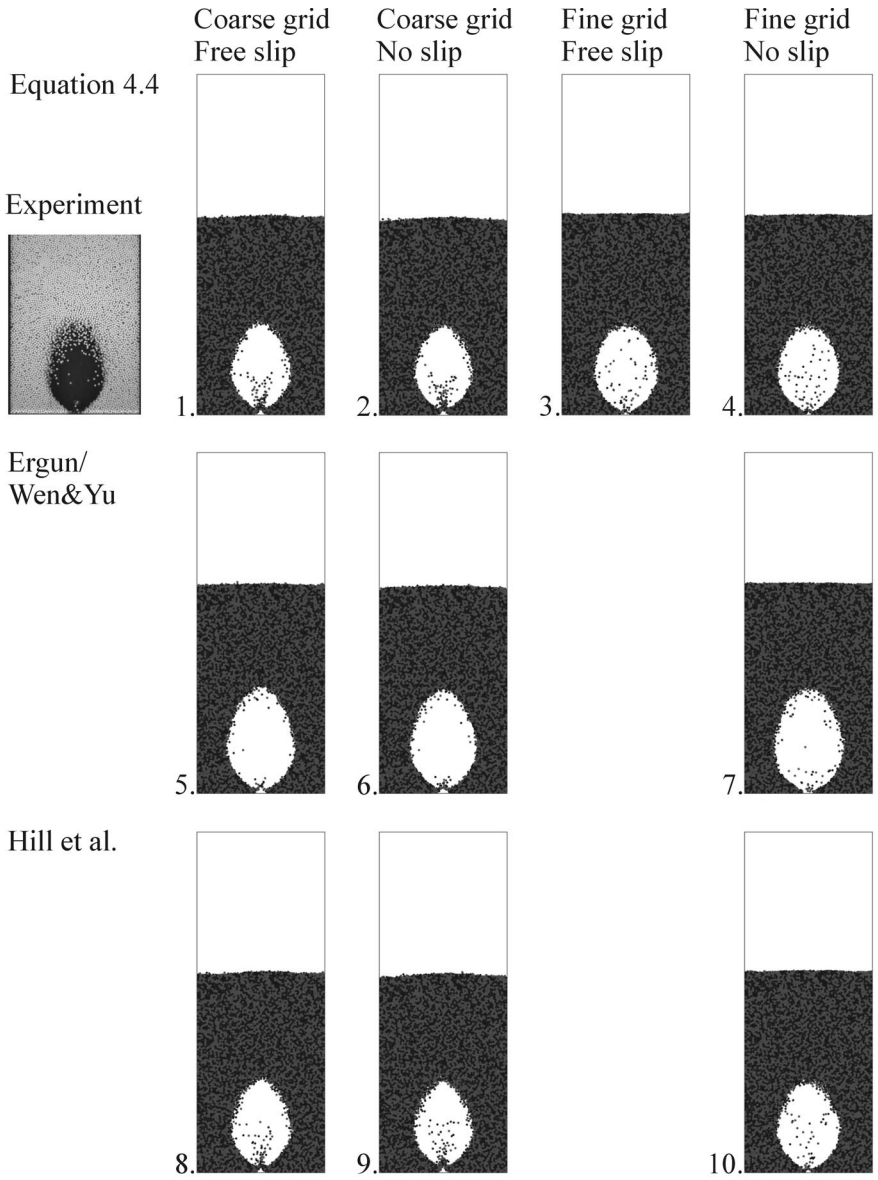

Figure 6.14: Snapshots from single bubble experiment and simulations at $t = 0.1$ s. Numbers refer to table 6.2.

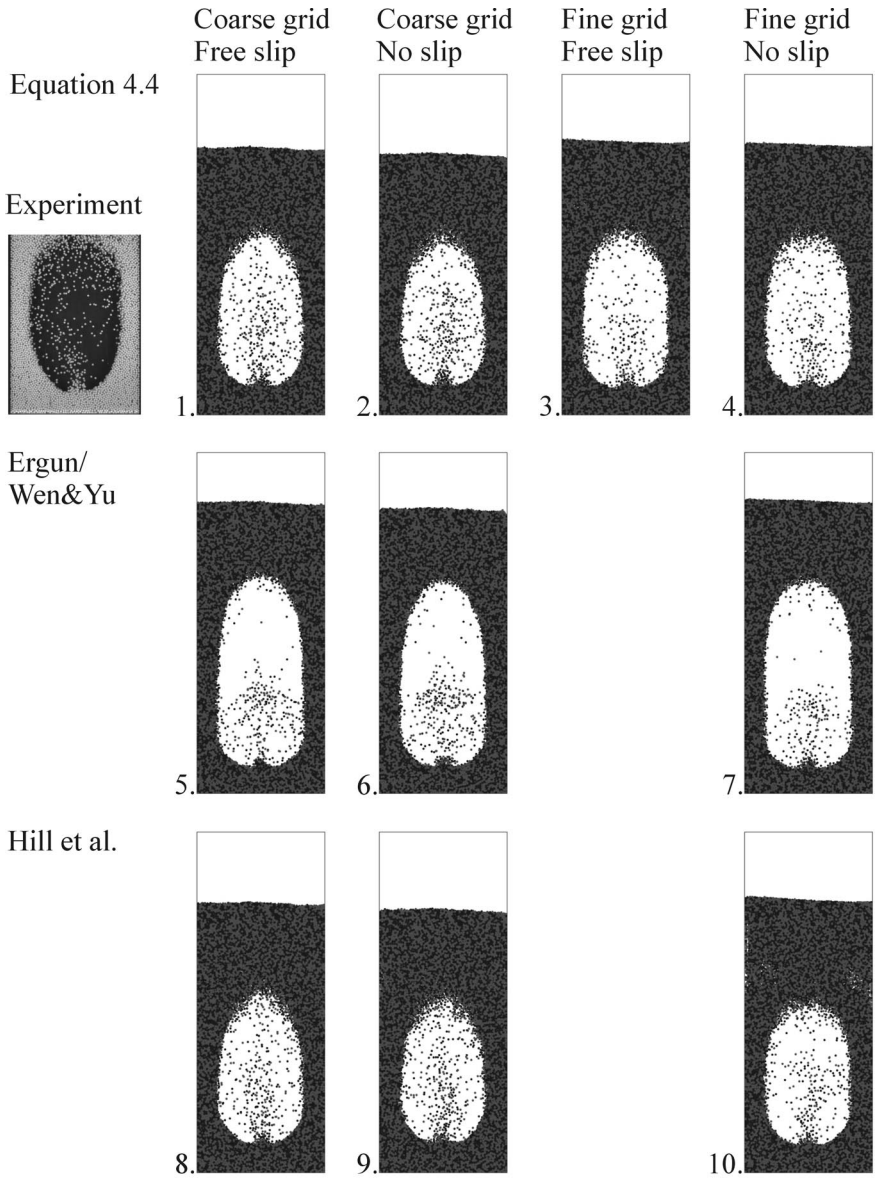

Figure 6.15: Snapshots from single bubble experiment and simulations at $t = 0.2$ s. Numbers refer to table 6.2.

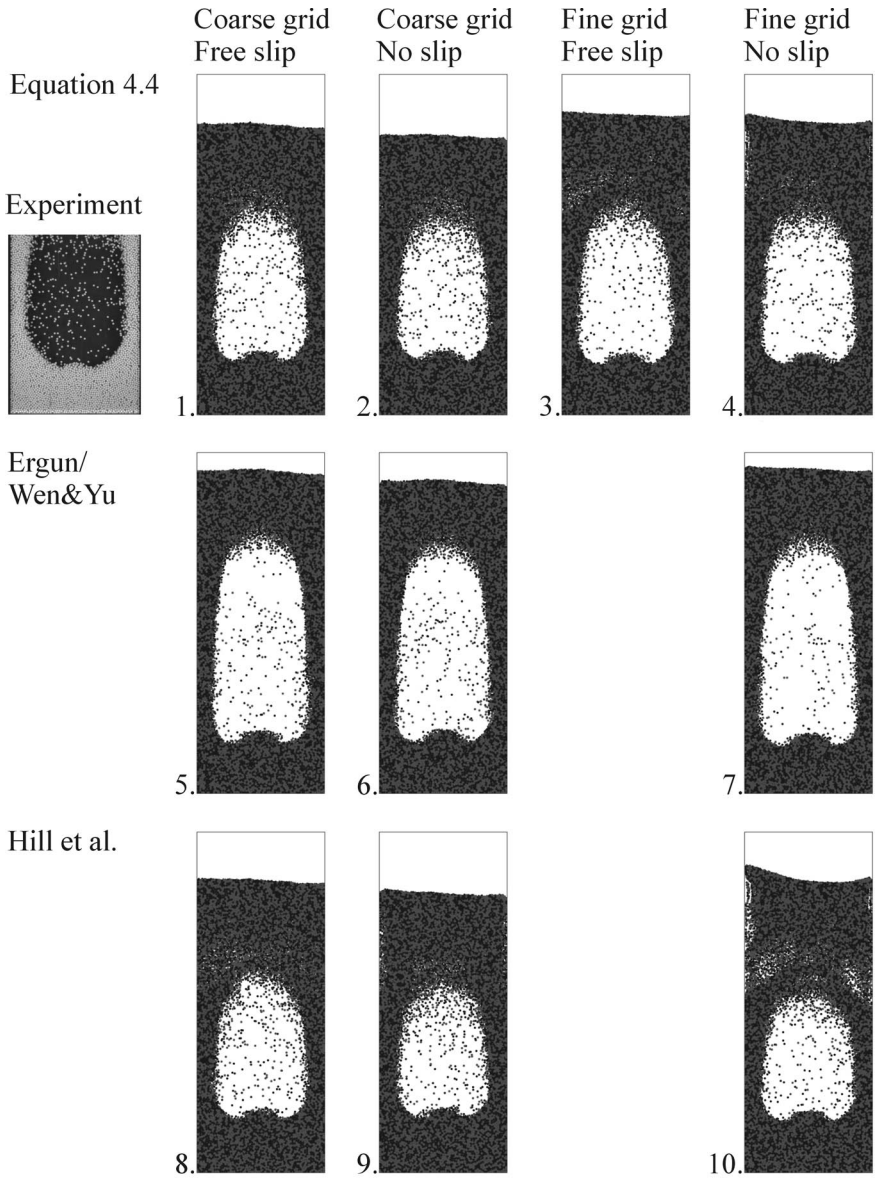

Figure 6.16: Snapshots from single bubble experiment and simulations at $t = 0.3$ s. Numbers refer to table 6.2.

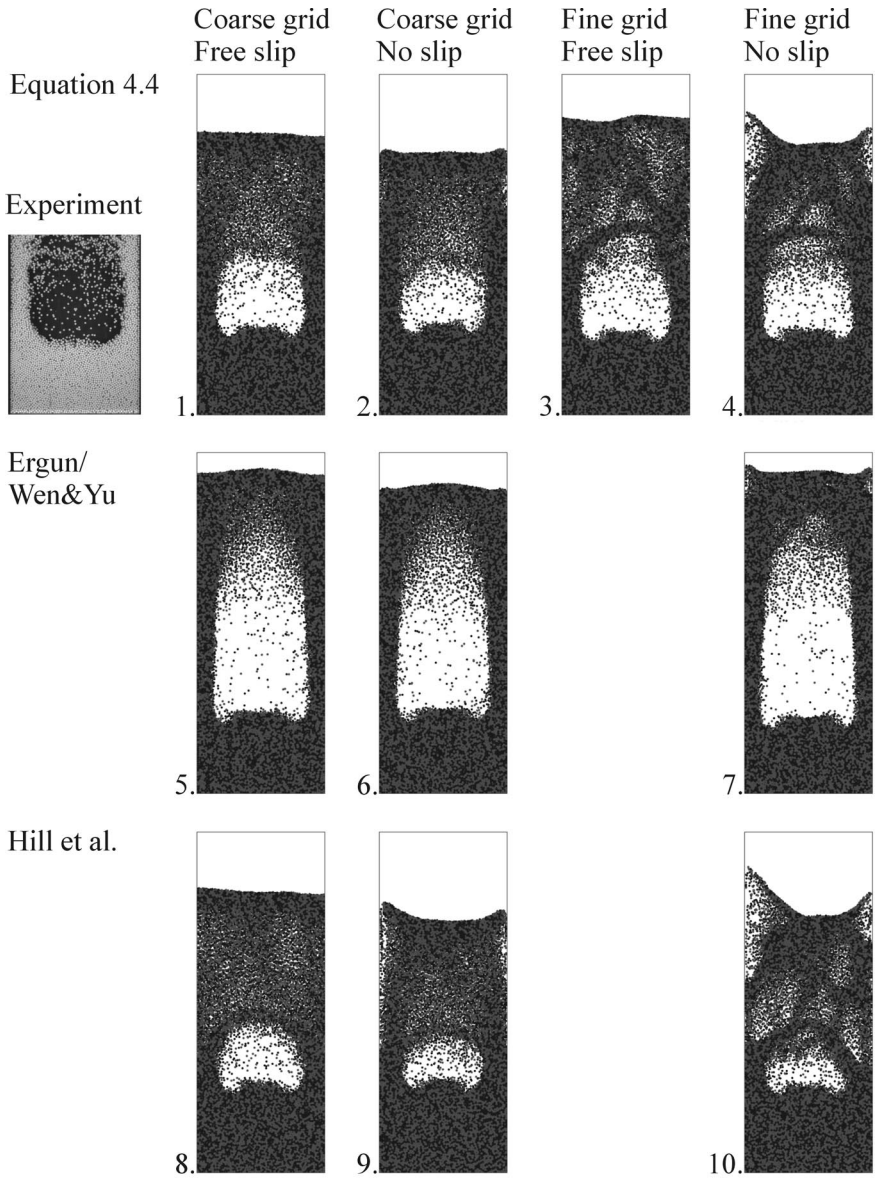

Figure 6.17: Snapshots from single bubble experiment and simulations at $t = 0.4$ s. Numbers refer to table 6.2.

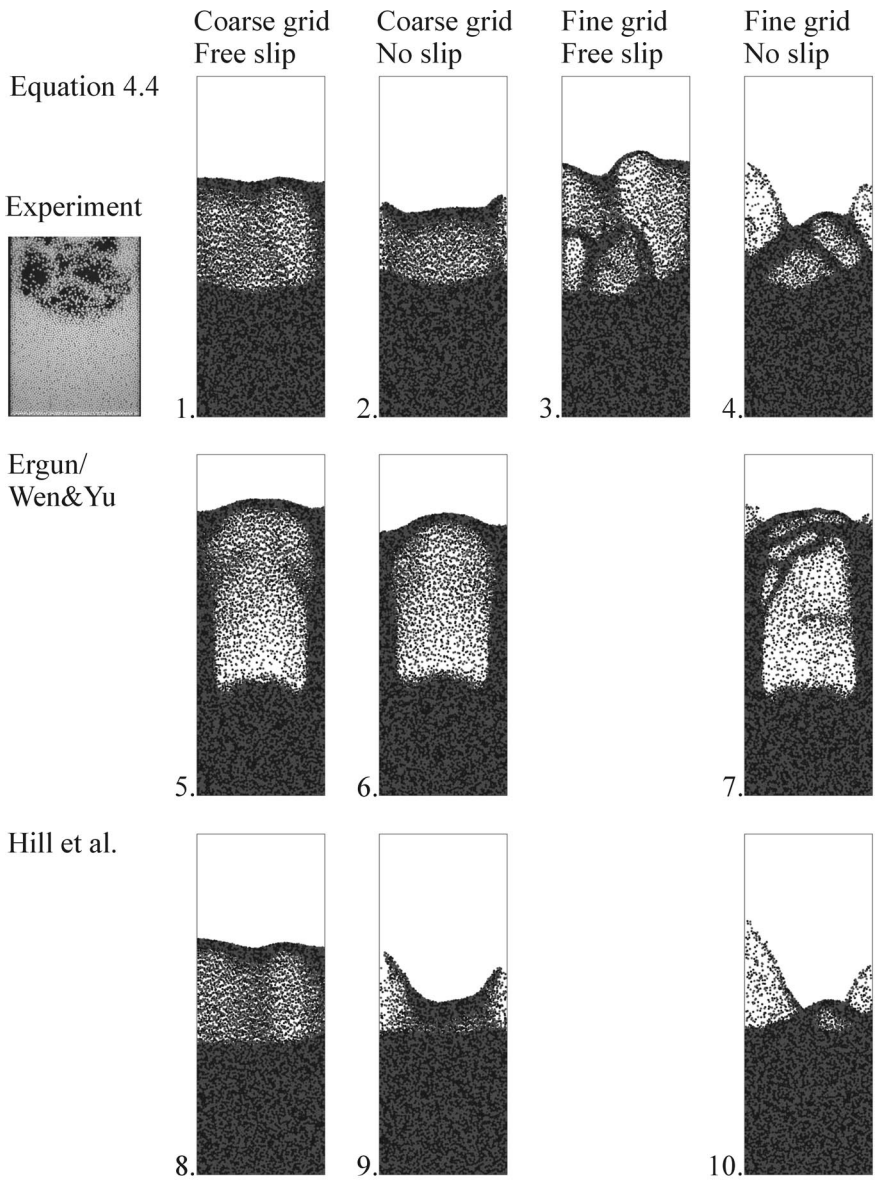

Figure 6.18: Snapshots from single bubble experiment and simulations at $t = 0.5$ s. Numbers refer to table 6.2.

figure 6.17). Since these structures are also found in the snapshots of the actual exeriment, it may be concluded that the increased grid refinement is necessary for a realistic simulation. Furthermore, in the simulations with no-slip boundary conditions larger voids are formed near the walls of the bed in the top zone, which is clearly visible at $t = 0.4$ s. The particles at the sides of the bed are pushed upward and to the center when the bubble collapses in these simulations, resulting in an almost v-shaped pattern of the top of the bed during these moments. Unfortunately, the images of Bokkers (2005) do not show the top section of the bed, thus no definite conclusion can be drawn about the best boundary conditions (free-slip or no-slip) so far.

When we refer to boundary conditions used for these simulations it should be borne in mind that these only concern the left and right walls, and not the entire bed (i.e., not the front and back walls). However, the depth of the pseudo-2D bed is too small to contain a sufficient number of cells in the y-dimension to vary the conditions of the front and back wall with the present DPM-code. Since the left and right walls are relatively small compared to the front and back wall, one could argue that the search for the most appropriate boundary conditions for the left and right wall is perhaps a bit futile as long as only a single cell is used in the z-dimension. It is expected that the simulations will improve even more when smaller grid cells (of the order of the particle diameter) are used and the gas phase is solved in three dimensions. However, this will put stronger demands on simulation time and computer capacity, and it could also be argued that for many applications any grid size or boundary condition that produces correct statistics in the long term is sufficient.

Results: drag model

In the simulations that use the Ergun and Wen and Yu equations the size of the bubble is overpredicted, as was already shown by Bokkers (2005). The bubble sizes in the simulations with the Hill, Koch and Ladd-relation and equation 4.4 the bubble sizes are more or less equal and compare well to the experiments (see figure 6.15). In figure 4.6 it could be seen that the Ergun equation severely overestimates the drag at high Reynolds numbers, with the effect that the particles are blown away from the jet much too fast, so that the bubble grows bigger than in the experiment. The simulations with the new relation (equation (4.4)) and the Hill, Koch and Ladd-relation are not

very different, which is not surprising as the Hill, Koch and Ladd-relation forms a reasonable fit to our data as well (see figure 4.8).

At the end of the simulations there is a large difference in the bubble size predicted from the various drag models, and also in the moment when the bubbles collapse completely. At $t = 0.5$ s (figure 6.18), the bubbles in the Ergun-simulations are still large, while in the simulations using the Hill, Koch and Ladd-drag the bubbles have almost collapsed completely for the no slip conditions, with the exception of a few particles near the walls. The new model is somewhere in the middle of these extremes. Unfortunately the top zone is not visible in the experimental picture so care should be taken in drawing conclusions from this, but at present it seems that the new drag closure from chapter 4 gives the best results.

6.3.2 Segregation simulations

When the particles in a fluidised bed differ in size and/or density, segregation may occur. This phenomenon is caused by a difference in drag force and/or gravity, with the result that one type of particles fluidises more easily than the other type. The particles that are easily fluidised (small or light particles) will move to the top section of the bed (flotsam), while the other particles settle in the bottom region (jetsam). In gas fluidised beds segregation usually occurs only at fluidisation velocities not far from the minimum fluidisation velocity of the larger or heavier particles. At higher gas velocities bubbles cause a more thorough mixing in the bed, thereby disturbing segregation patterns. Liquid fluidisation is usually more homogeneous than gas fluidisation, which is the reason why segregation can occur at higher velocities as well in this type of processes.

In practical applications segregation can be important, as particles are almost never monodisperse. In polymerisation or granulation processes high diameter ratios may occur, which strongly influences the hydrodynamic behaviour and mixing in the reactor. On the other hand, it is essential to control the size distribution of the end product and to prevent clogging of the reactor. Therefore, a model that is able to predict segregation accurately will be a very useful tool in industrial applications.

Hoomans (1999), Goldschmidt (2001a) and Bokkers et al. (2004) have shown that it is very difficult to predict segregation processes in fluidised suspensions accurately with the current CFD-models, especially when the rate of

this segregation is used as a criterion and not merely the final state. This suggests that the drag models require some modification for use in binary or polydisperse systems.

In chapter 5 it was shown that the drag force on a particle in a binary or polydisperse mixture can be substantially different from the drag force on the same particle in a monodisperse system with equal porosity and at equal Reynolds number. A relation was presented to correct for the effect of polydispersity, which depends on the porosity, diameter ratio and composition of the mixture. It is to be expected that this correction will influence the behaviour in DPM-simulations of polydisperse mixtures noticeably.

The segregation simulations presented here are based on the experiments performed by Goldschmidt et al. (2003), where glass particles with diameters of 1.5 and 2.5 mm were fluidised with air in a pseudo-2D column. The mixture consists of 25 % small particles and 75 % large particles, and the fluidisation velocity is 1.30 m/s. Details of the experiments and simulation are given in table 6.3.

The degree of segregation in the experiment was determined with an optical method (Goldschmidt et al., 2003): pictures that were taken during the experiment were divided in cells, and the intensities of red (large particles) and yellow (small particles) were determined for each cell. From the fraction of large and small particles in the cell the degree of segregation could then be determined. This degree of segregation is defined as:

$$s = \frac{S - 1}{S_{max} - 1} \,, \tag{6.1}$$

where $S = \langle h_{small} \rangle \,/\, \langle h_{large} \rangle$ and $S_{max} = (x_{large} + 1) \,/ x_{large}$, $\langle h_i \rangle$ being the average height of particles of type i and x_{large} the volume fraction of large particles. Thus, for a completely mixed system $s = 0$, and for a completely segregated system $s = 1$. In the simulations the same quantitative measure for segregation is determined via the z-coordinates of all particles.

The experiments were repeated three times, which differed slightly in the degree of segregation. Values for the degree of segregation that are shown in the figures in this section are the average of these three experiments. The simulation was performed with several drag models and boundary conditions. An overview of the various combinations is shown in table 6.4. Note that we also performed simulations with the Ergun and Hill, Koch and Ladd-drag models with the new correction for polydispersity, since this correction factor can in principle be coupled with any monodisperse drag relation.

Table 6.3: Settings in the segregation simulations.

Width	0.15 m	
Depth	0.015 m	
Height	0.45 m	
Gas velocity	1.3 m/s	
	Coarse grid:	**Fine grid:**
Cells in x-direction	15	30
Cells in y-direction	1	1
Cells in z-direction	45	90
Particles	**Large:**	**Small:**
Number	17940	27720
Diameter	2.5 mm	1.5 mm
Density	2525 kg/m^3	2525 kg/m^3
Coeff. of normal restitution	0.97	0.97
Coeff. of friction	0.10	0.10
Coeff. of tangential restitution	0.33	0.33

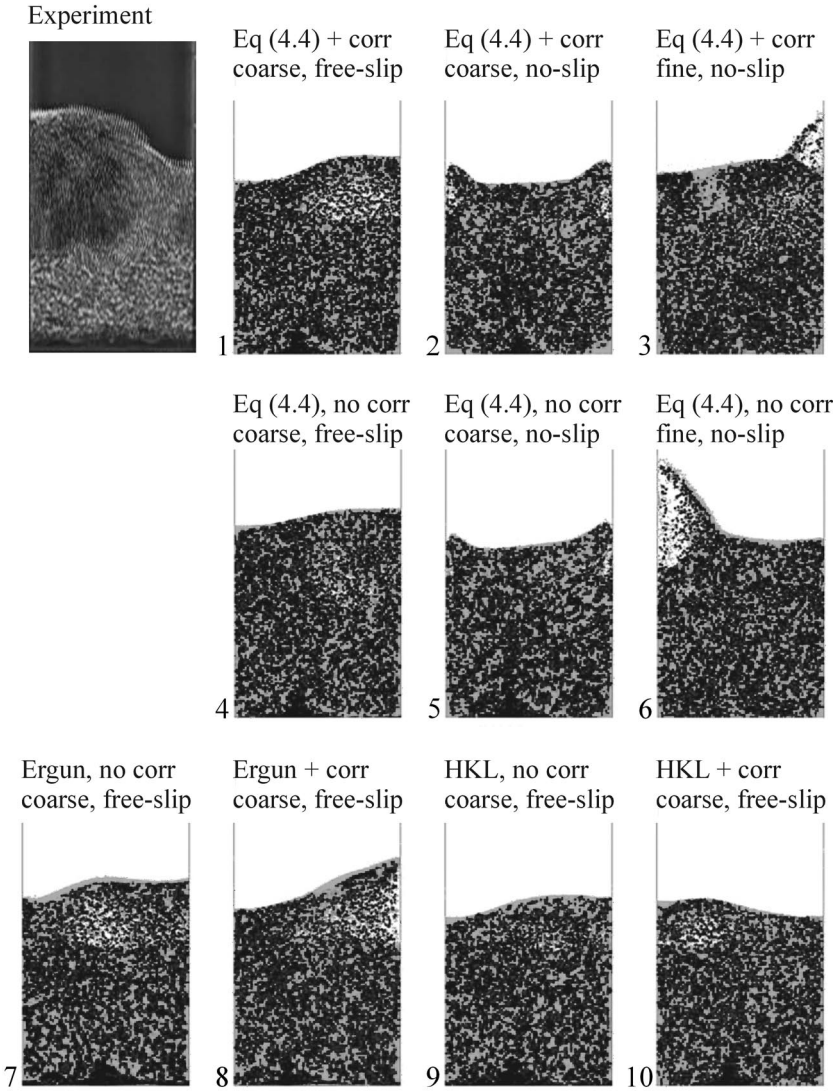

Figure 6.19: Snapshots from segregation experiment and simulations showing typical bubble patterns. All snapshots are taken shortly after start-up ($t = 2 - 6$ s). Numbers refer to table 6.4.

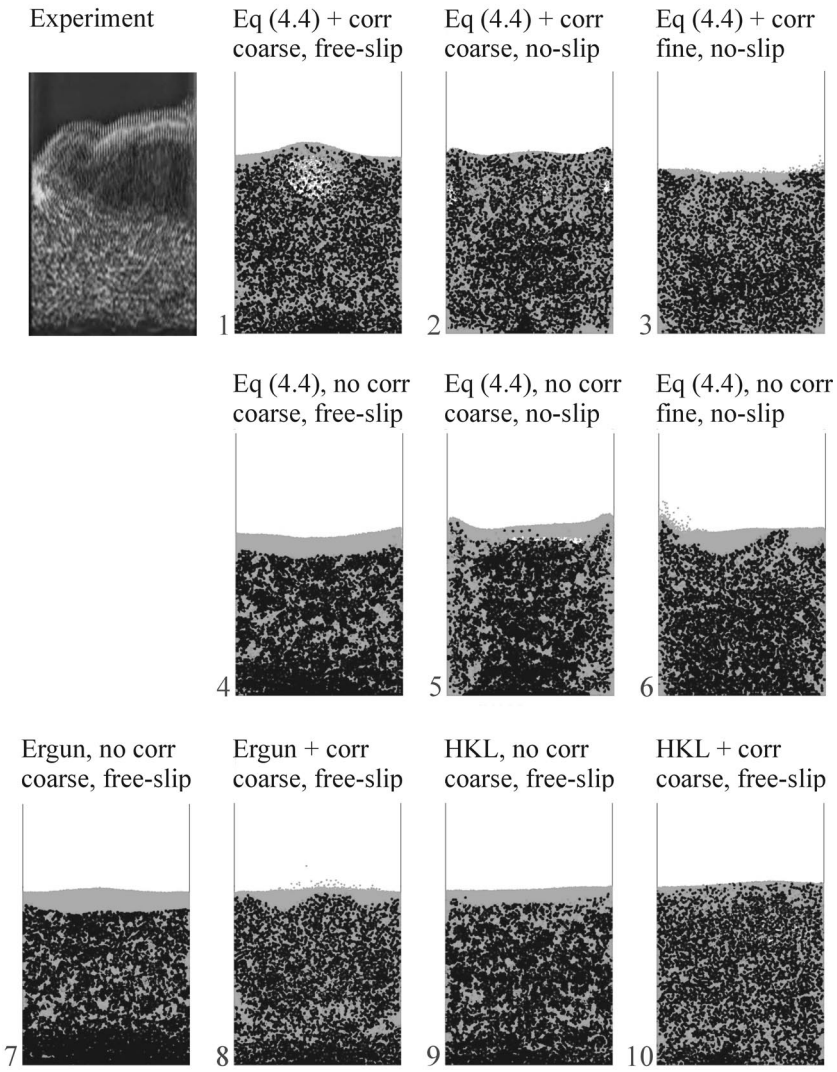

Figure 6.20: Snapshots from segregation experiment and simulations at $t = 10$ s. Numbers refer to table 6.4.

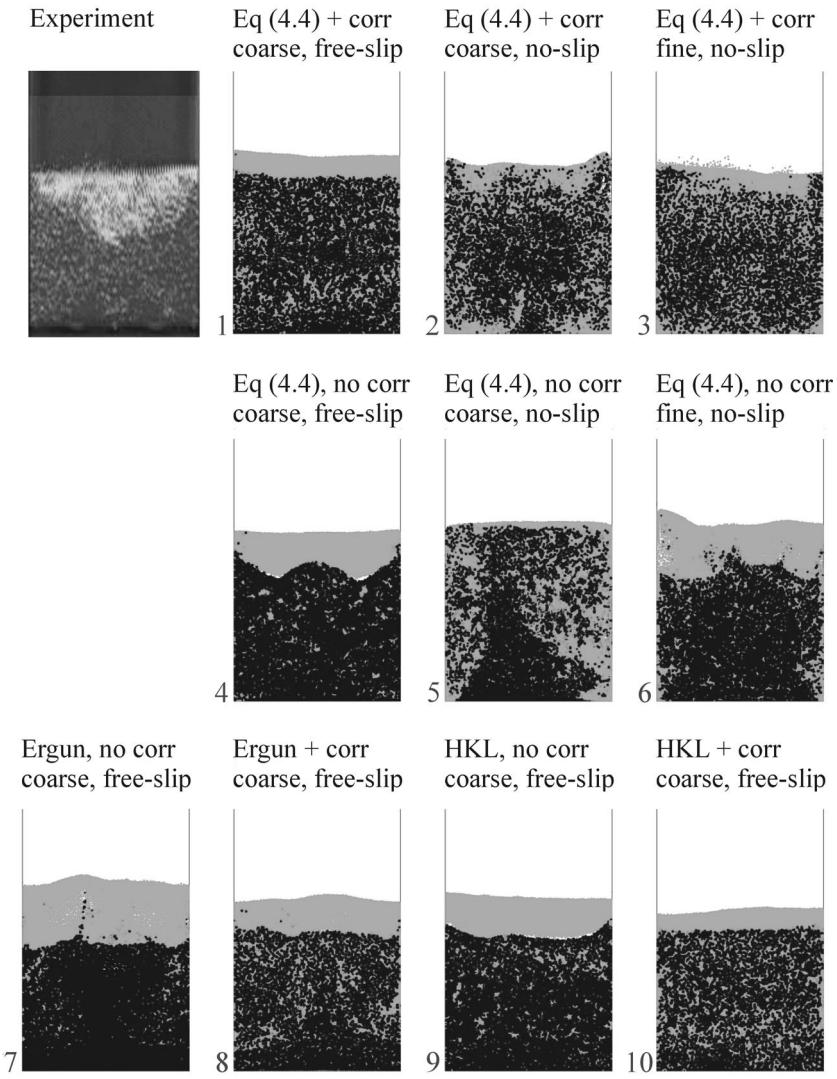

Figure 6.21: Snapshots from segregation experiment and simulations at $t =$ 30 s. Numbers refer to table 6.4.

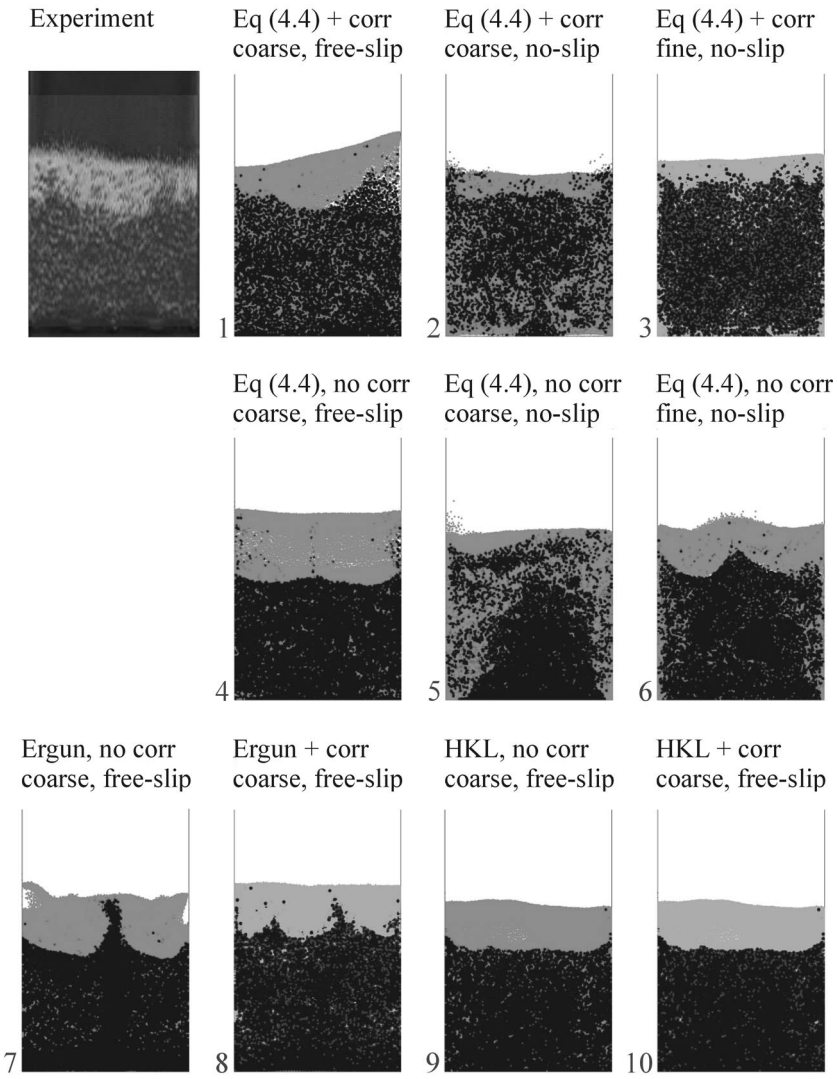

Figure 6.22: Snapshots from segregation experiment and simulations at $t =$ 50 s. Numbers refer to table 6.4.

Table 6.4: Drag models and boundary conditions in the segregation simulations.

Run	Drag model	Correction	Grid	Boundary
1	Equation (4.4)	yes	coarse	free-slip
2	Equation (4.4)	yes	coarse	no-slip
3	Equation (4.4)	yes	fine	no-slip
4	Equation (4.4)	no	coarse	free-slip
5	Equation (4.4)	no	coarse	no-slip
6	Equation (4.4)	no	fine	no-slip
7	Ergun/Wen & Yu	no	coarse	free-slip
8	Ergun/Wen & Yu	yes	coarse	free-slip
9	Hill et al.	no	coarse	free-slip
10	Hill et al.	yes	coarse	free-slip

Figures 6.19 to 6.22 show snapshots of the experiment and simulations. Figure 6.19 shows typical bubble patterns that occur in each simulation, the others illustrate the evolution of the segregation in time. A qualitative comparison shows that the bubble patterns in the experiment and the simulations are very different, where the bubbles in the simulations are much smaller. In the no-slip simulations all bubbles move towards the side walls of the bed, whereas in the experiment and free-slip simulations they also pass through the centre. The size of the bubbles has a strong influence on the particle dynamics, most notably in the top layer. The top layer in the simulation stays more or less at its place, whereas in the experiments it is moving vigorously with every new eruption of a bubble. A more quantitative comparison reveals that the bubble frequency (measured from bed expansion characteristics) is higher in the simulations, ranging from $2.5 - 3.1$ Hz, where this was 1.9 Hz in the experiments (Goldschmidt et al., 2003). In simulation number 4 an even higher frequency of 3.7 Hz was observed for some period of time, which was mainly due to some vigorous motions in the segregated top layer.

In the simulations with no-slip boundary conditions and a coarse grid, many

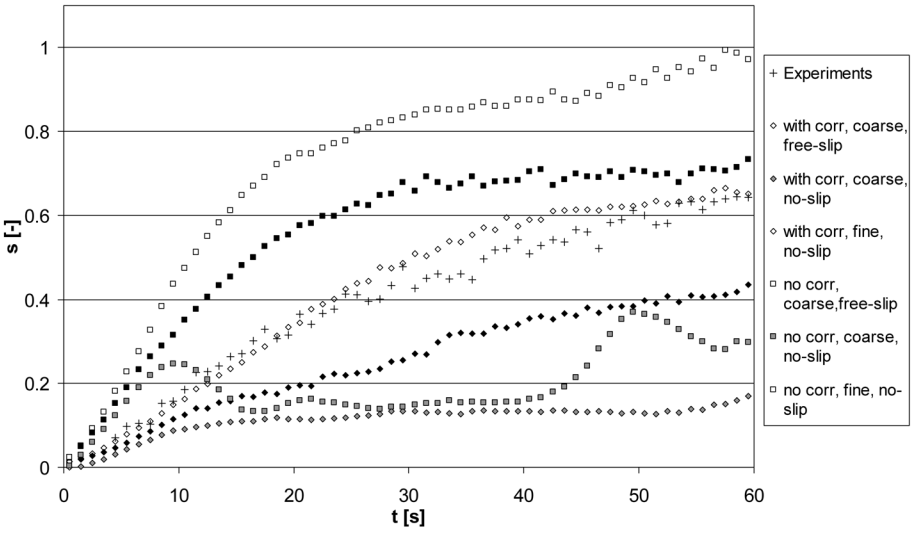

Figure 6.23: Degree of segregation as a function of time in experiments and simulations with various boundary conditions. The drag force is calculated from equation (4.4) in all simulations, the legend gives the other settings.

small particles are located in the vicinity of the side walls of the bed. A movie of the simulation reveals a flow pattern of (small) particles moving up through the center of the bed in the wake of bubbles, followed by a downwards motion from the segregated layer along the sides of the bed, a phenomenon which does not appear as such in the experiments. This is related to the bubble pattern that was discussed previously: in the experiment large bubbles disturb circulation patterns that are formed, so that the particles have no chance to move downwards near the walls. A closer look into this phenomenon will be taken in the next section.

Results: grid and boundary conditions

The degree of segregation as a function of time in simulations with various boundary conditions is shown in figure 6.23, and compared to the experimental value (average of three experiments). The segregation rate is much higher in simulations with free-slip conditions than in simulations with no-slip conditions. The reason is that in the no-slip simulations the fluid velocity near the walls is smaller, so that the drag in the cells near the wall is also

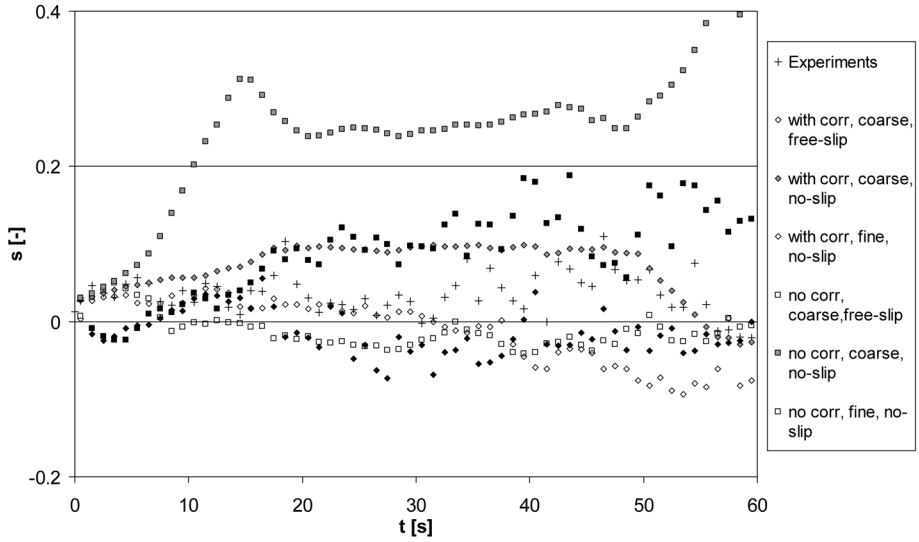

Figure 6.24: Degree of segregation in the lateral direction as a function of time in experiments and simulations using various types of boundary conditions. he drag force is calculated from equation (4.4) in all simulations, the legend gives the other settings.

lower than in the rest of the bed. As a result, the drag force acting on particles close to these walls will not balance gravity anymore, so particles that have reached the top layer move down again along the sides with a lower segregation rate as a result.

Figure 6.24 shows the degree of segregation in the lateral direction (x-dimension) s_{lat}, which is defined in the same way as the degree of axial segregation s, where instead of the average height of the particles of type i the average x-position relative to the center of the bed is taken. The difference between the simulations is obvious: in the simulations with no-slip boundary conditions the lateral segregation is much larger than in the experiments and the free-slip simulations. This effect is even more pronounced in simulations using the Ergun and Hill drag models and no-slip boundaries that are not shown here. The simulations with no-slip conditions performed on a finer grid produce better results than the coarse grid simulations, which can be explained by the fact that the zone near the wall with a reduced gas velocity is smaller. The simulations with the new model with correction for polydispersity show less lateral segregation than simulations without this correction, the reason of which is not completely evident. The change in

the drag force may also bring about subtle changes in the size and path of the bubbles, that are not large enough to observe in the snapshots. These changes could disturb the circulation patterns of the bed. A more thorough investigation into porosity and particle velocities in the bed is clearly required to confirm this.

The same remark about the front and back walls as in the single bubble simulations applies: the boundary conditions at these walls were not varied because of the small y-dimension and are assumed to be free-slip. Therefore, one could wonder in this case as well if it is very useful to model the smaller left and right walls as accurately as possible.

Concluding, no-slip boundary conditions in segregation simulations on a coarse grid do not agree well with the realistic situation as observed in the experiments. It is probably best to model these systems with free-slip boundary conditions, as the bed in this case feels no influence from the walls and no unrealistic circulation patterns are formed.

Results: drag model and polydispersity factor

When the correction factor for polydispersity, equation (2.56) or (5.1), is taken into account, the drag on the small particles in the system becomes smaller while the larger particles experience a larger drag than in a simulation without this correction factor. Thus, the smaller particles move to the top zone at a slower rate, while the larger particles have a lower downward velocity, which means that the segregation rate becomes slower. Figure 6.25 clearly illustrates this effect for the free-slip simulations: for all drag models the segregation becomes much slower with this correction (open symbols) than without it (closed symbols). In figure 6.23 it can be seen that this is also valid with other boundary conditions.

When we look at figure 6.25 we see that in the simulations without the correction factor the systems are almost completely segregated after one minute of simulation time, whereas the segregation in the experiment is 64 % after the same period of time. The degree of segregation in the simulation with the new drag relation with polydispersity correction has a value of 65 % at this time, and the rate at which the segregation occurs in the same simulation also compares very well with the trend observed in the experiment. The rate is better predicted with the new model than with the combination of Ergun and Wen and Yu equations with correction, while the

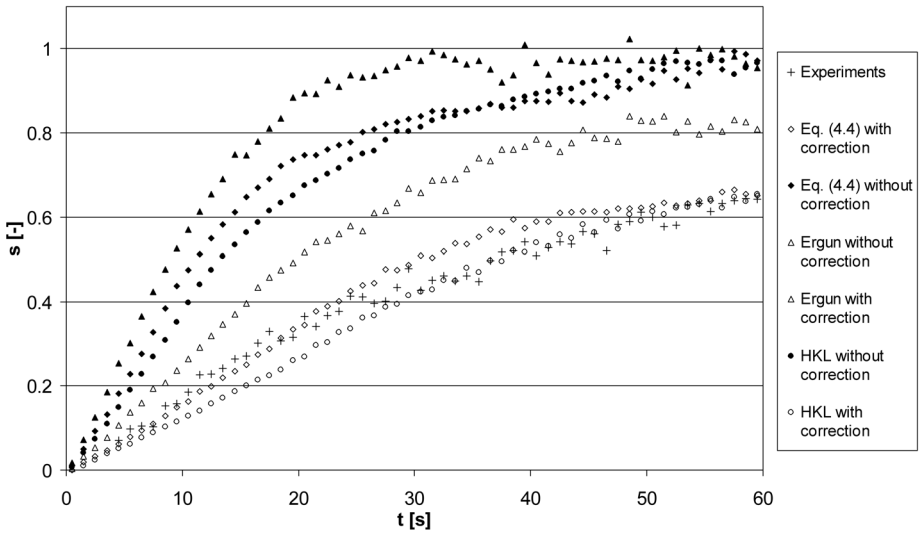

Figure 6.25: Degree of segregation as a function of time in experiments and simulations with various drag models. All simulations were performed on a course grid with free-slip boundaries. The drag force is shown in the legend.

performance of the model of Hill et al. (2001b) is comparable to the new drag model obtained from this study.

It can be concluded that in segregation simulations, the correction factor for polydispersity gives a significant improvement over drag models without this correction. The effect of the drag model itself is less pronounced, where the Ergun/Wen and Yu correlation gives the worst agreement with the experiments.

6.4 Inversion

Layer inversion is a phenomenon that may occur when a system contains two (or more) particle species differing in both size and density, where the smaller particles have a larger density. At low liquid velocities gravity dominates the drag force, and the small but heavy particles will reside in the bottom section of the column. By raising the liquid velocity the drag force will increase, which results in a better mixing of the two phases. At the inversion velocity, the two phases are completely mixed. When the velocity is increased even

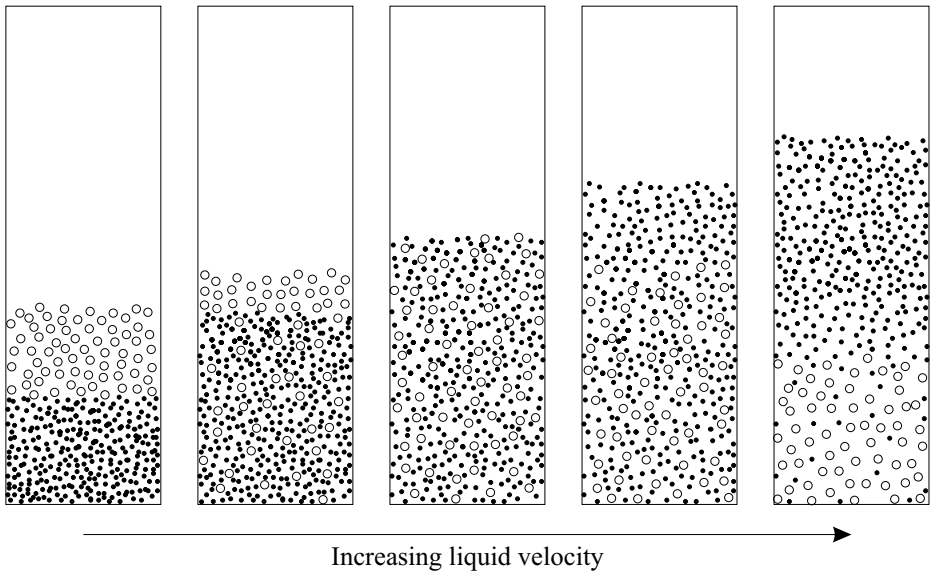

Figure 6.26: Schematic representation of layer inversion in liquid fluidised beds, where the small particles have a higher density than the larger particles. The velocity is increased from left to right while the mixture composition is kept constant.

further the drag forces dominate over gravity and the smaller particles will occupy the top section of the column. Thus, effectively the order of the layers is inversed, as is illustrated in figure 6.26. The velocity at which the particles are mixed completely depends on the physical properties of both species and the composition of the mixture. Layer inversion occurs in mixtures containing three or more particle species as well, although in this case there is usually not a single inversion point (see e.g. Berres et al., 2005).

The phenomenon has only been observed in liquid fluidisation, as this is usually more homogeneous than gas fluidisation. Although in theory inversion might occur in gas-fluidised beds, in practice the vigorous mixing due to bubbling action disturbs the segregation in layers, especially at high gas velocities.

The inversion phenomenon has been a topic of research interest for some years now. Moritomi et al. (1982, 1986) studied the inversion for a mixture of hollow char and glass particles as a function of mixture composition and diameter ratio. Their data have been used by other researchers to test the validity of their drag relations (see e.g. Patwardhan and Tien, 1985; Galvin et al., 1999; Biesheuvel, 2000). The systems that are used for the comparison of different drag models are composed of glass particles with a diameter of $d_g = 0.163$ mm and char particles of $d_c = 0.775$ mm, with densities of 2450 and 2450 kg/m^3 respectively. The amount of glass particles in the column was fixed at 100 g, while the amount of coal was varied from 10 to 70 g in order to change the equilibrium composition of the mixture and thus its inversion velocity.

6.4.1 Calculation of the inversion velocity

The inversion point of a particle mixture is found by calculating the porosity and liquid velocity at which an ideally mixed system of that composition is exactly in equilibrium, meaning that the forces originating from the fluid flow balance gravity for both particle species.

Figure 6.27 shows the inversion velocity of mixtures calculated from the new drag model, equation (4.1), in combination with the correction for bidispersity, equation (5.1). The experimental results of Moritomi et al. (1986) are also shown, as well as the results from calculations using several literature models. It can be seen that the values calculated from the model of Masliyah (1979) are wide from the mark, where the other models, of Patwardhan and

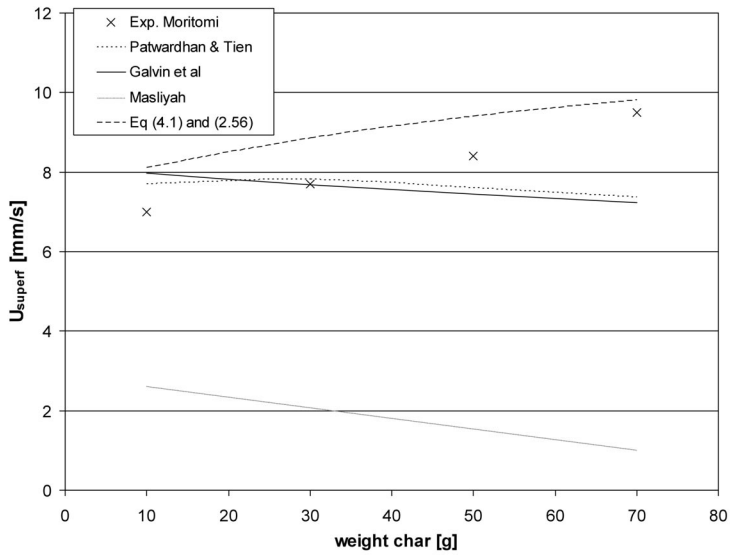

Figure 6.27: Inversion velocity as a function of mixture composition calculated from various drag models, compared to the experiments of Moritomi et al. (1982).

Tien (1985) and Galvin et al. (1999), predict more realistic values for the inversion velocity. However, they do not show the correct trend when the mixture composition is changed. The combination of equations (4.1) and (5.1) shows the correct trend, although the inversion velocity in mixtures with a low amount of coal is overpredicted by about 16 %.

6.5 Conclusions

The pressure drop experiments confirm the validity of equation (4.1) to calculate the drag force in both mono- and bidisperse random packed beds at low Reynolds numbers. For intermediate Reynolds numbers however, a systematic deviation from theoretical predictions from equation (4.4) was found. This could be due to the fact that the drag force in this regime is difficult to capture by a relatively simple functional form such as equation (4.4), where the latice-Boltzmann data is not accurate enough to allow for a more refined fit. Another cause could be the uncertainty in the values for porosity and viscosity, in particular since the same deviation was not

observed in the low Reynolds number experiments with glycerine.

The drag model from chapters 4 and 5 was implemented in the discrete particle model, with which the formation of a single bubble by a jet, as well as the segregation of a binary mixture were studied. The results from simulations using various drag models, grid sizes and boundary conditions were compared to experimental data. The single bubble simulations showed that a fine grid is required to obtain realistic structures in the particle behaviour. However, they were not fully conclusive as to what drag relation gives the most realistic bubble behaviour. In the segregation simulations, the segregation rates were predicted very well by the new drag model (equation (4.4)) in combination with the correction for bidispersity (equation (5.1)). Free-slip boundary conditions produced more realistic results than no-slip boundaries. It can be concluded that with the new drag relation and the correction for polydispersity a significant improvement can be made in the CFD models.

Finally, the calculation of the inversion velocity of mixtures of varying compositions showed that also in this case better results are obtained with the new model, in combination with the correction factor for polydispersity, than with several literature models.

Chapter 7

Drag force in clusters of spheres

Abstract

Drag coefficients of irregularly shaped particles, constructed from spheres, were measured in lattice-Boltzmann simulations and compared to experimental data from literature. The agreement is very well. The distance between the spheres was increased to study the influence of inter-particle distance on the drag force in clusters. The drag coefficient of the clusters was found to increase with inter-particle distance. The drag force on an individual particle in a cluster is, as expected, lower when that particle is shielded from the flow by other particles.

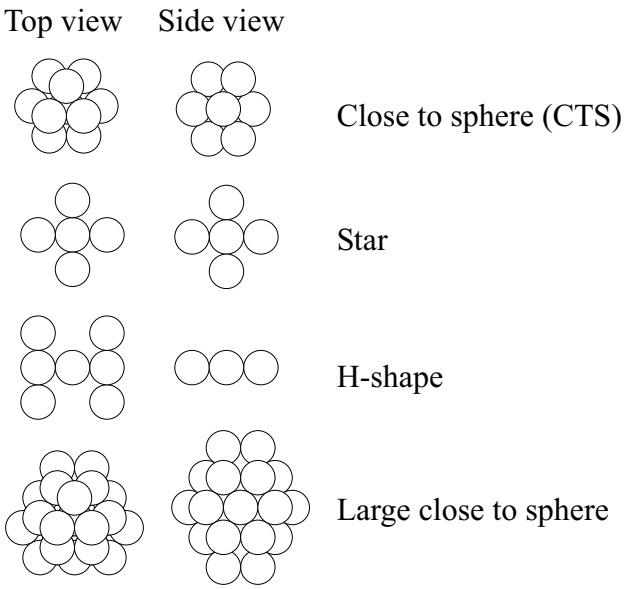

Figure 7.1: The cluster shapes studied in the simulations. The distance between the particles was varied.

7.1 Introduction

Most drag relations that are used in CFD modelling were derived for ideal systems, that are monodisperse and homogeneous. However, in practical applications these ideal circumstances almost never occur. Moreover in processes such as spray granulation granules are formed, which consist of a certain number of primary (spherical) particles, with a rather complex shape. In chapter 5 we showed that the drag force on a particle in a bi- or polydisperse mixture can differ substantially from the drag force on the same particle in a monodisperse system with otherwise equal parameters. This chapter focuses on the drag force in clusters, which can be seen as a different type of non-ideality.

In a recent paper Tran-Cong et al. (2004) report on experiments in which the drag coefficients of irregularly shaped particles are measured. They constructed six configurations by gluing together up to fourteen spheres and determined the terminal velocity of these shapes. The drag coefficient calculated from this velocity was compared to the drag coefficient of spheres having equal volumes or equal projected surface area. The irregular shapes

that were studied by Tran-Cong et al. (2004) can be considered as clusters of spheres where the particles are very close together. Their experiments form a good starting point for simulations of the drag force on clusters, since they provide data that can be compared directly to the simulation results. Moreover, the configurations are made from spheres and can thus be easily implemented in a lattice-Boltzmann code.

Simulations were performed for three of the configurations that were studied by Tran-Cong et al. (2004), namely a nearly spherical configuration, a star and an H-shaped particle (see figure 7.1). A close-to-spherical configuration that was made up of more particles was also simulated in order to study the influence of cluster size.

7.1.1 Drag force of irregularly shaped particles

As discussed in chapter 2, the drag force for a single spherical particle is often presented in the form of a drag coefficient C_d, which was defined in equation (2.9) as

$$F_d = C_d\,(Re)\,\frac{\pi d^2}{4}\frac{\rho U^2}{2}\ .$$

Note that the factor $\pi d^2/4$ in this equation is equal to the projected surface of the particle perpendicular to the direction of the flow. For the case of irregularly shaped particles two drag coefficients are defined, since there are several options to determine the diameter of such a particle. The 'normal' drag coefficient C_d is calculated from the drag force using the volume equivalent diameter d_n (i.e. the diameter of a sphere with equal volume as the irregular shape), and is defined as

$$F_d = C_d\,(Re)\,\frac{\pi d_n^2}{4}\frac{\rho U^2}{2}\ . \tag{7.1}$$

$C_{d,A}$ is the drag coefficient based on the projected surface of the particle:

$$F_d = C_{d,A}\,(Re)\,A_p\frac{\rho U^2}{2} = C_{d,A}\,(Re)\,\frac{\pi d_A^2}{4}\frac{\rho U^2}{2}\ , \tag{7.2}$$

where d_A is the diameter of a sphere with equal projected surface as the irregular shape and A_p is the projected surface area of the particle normal to the direction of flow. The two drag coefficients are obviously related by

a factor $(d_A/d_n)^2$. Similar considerations apply to the Reynolds number of these particles: Re is used for the Reynolds number based on d_n, whereas Re_A is the Reynolds number based on d_A.

Tran-Cong et al. (2004) measured the drag coefficients of irregularly shaped particles and compared their results to the expression for the drag coefficient of a spherical particle that was originally proposed by Clift et al. (1978), which is valid for Reynolds numbers up to $3 \cdot 10^5$:

$$C_d = \frac{24}{Re}\left[1 + 0.15Re^{0.687}\right] + \frac{0.42}{1 + 4.25 \cdot 10^4 Re^{-1.16}} \,. \tag{7.3}$$

Tran-Cong et al. (2004) found it sufficient to characterize the shape of a particle by two parameters: the ratio of the volume equivalent sphere diameter to the projected surface equivalent sphere diameter d_n/d_A, and the 'circularity' c of the projected surface, which is defined as the ratio of the perimeter of a sphere with equal projected surface area to the perimeter of the projected surface of the actual particle. With these two parameters they modified the equation of Clift et al. (1978) for the drag coefficient of a single particle in the following way:

$$C_d = \frac{24}{Re}\frac{d_A}{d_n}\left[1 + \frac{0.15}{\sqrt{c}}\left(\frac{d_A}{d_n}Re\right)^{0.687}\right] + \frac{0.42\left(\frac{d_A}{d_n}\right)^2}{\sqrt{c}\left[1 + 4.25 \cdot 10^4\left(\left(\frac{d_A}{d_n}\right)Re\right)^{-1.16}\right]} \,. \tag{7.4}$$

The modified correlation describes the experimental results very well. Values for d_n/d_A and c for the shapes that were used in our lattice-Boltzmann simulations are shown in table 7.1.

7.2 Simulations setup

For the simulations the same setup procedure was used as described in section 3.4, where instead of random configurations of spheres a single cluster was used as shown in figure 7.1. Periodic boundary conditions were used in all dimensions, so that effectively a regular array of clusters is simulated.

The diameter of the particles from which the clusters were formed was usually 9.6 lattice spacings, and the width and depth of the simulation volume

Table 7.1: Number of constituting spheres, ratio of the volume equivalent sphere diameter to the projected surface equivalent sphere diameter d_n/d_A, and circularity c of the projected surface for the irregular particles that were used in the simulations.

Shape	Number of spheres	d_n/d_A	c
Close-to-sphere (CTS)	13	1.15	0.901
Star	7	1.17	0.447
H-shape	7	1.38	0.378
Large CTS	32	1.12	0.712

were 200×200 grid points. The height was varied with the Reynolds number, to minimize influence of periodical images. For low Reynolds numbers a height of 200 grid points proved to be enough, for higher Reynolds numbers lengths up to 1000 grid points were used.

According to the experimental results of Tran-Cong et al. (2004), the particles fall with the largest projected surface area perpendicular to the direction of the flow. Therefore, the particles in the simulation were given this orientation with respect to their velocity, and similar to the simulation of random arrays, a force was exerted on the fluid counteracting the force from the particles. Particle velocity and fluid viscosity were varied to obtain a large range of Reynolds numbers. The simulations were run until steady state was reached, after which the force on each particle was measured. An example of the drag force on an irregularly shaped particle is shown in figure 7.2. If steady state was not reached after $150 - 200$ hours of calculation time on a parallel cluster (which occurred in particular in high Reynolds number simulations) the results were extrapolated, assuming an exponential approach as is shown in figure 7.3. This method was tested and proved to be accurate within 0.2 %.

Apart from this simulations of clusters with a larger inter-particle distance were performed. The distance between the particles was increased, while the configuration was kept the same. All other aspects of these simulations are equal to the cases described above.

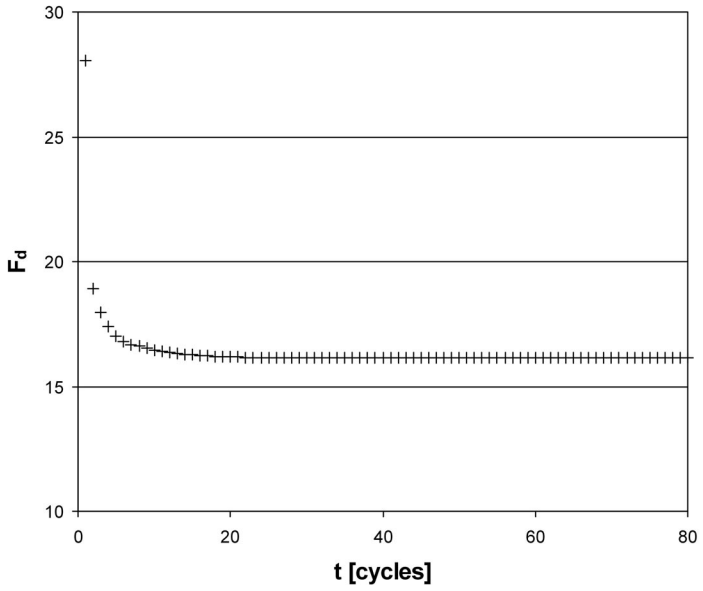

Figure 7.2: Drag force on an irregularly shaped particle.

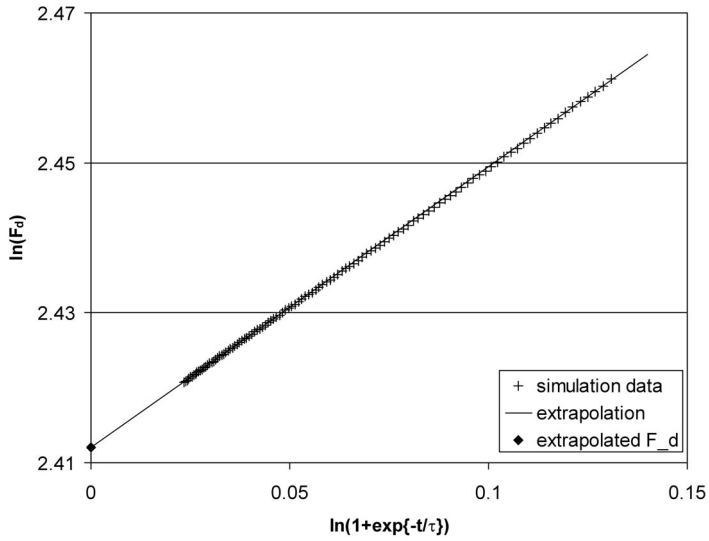

Figure 7.3: Extrapolation of the force on an irregularly shaped particle to infinite time.

7.3 Results

Figures 7.4 and 7.5 show cross-sections of some typical flow profiles around a close-to-spherical particle at different Reynolds numbers. The velocities are scaled to a situation where the particles are not moving. At low Reynolds numbers the profile is symmetrical around the cluster, showing laminar flow. Increasing the Reynolds numbers leads to longer wakes, as expected. At the particle boundaries no-slip conditions apply.

The force on each particle was measured, from which the total drag force F_d on the cluster was determined. The surface based drag coefficient was then calculated using equation (7.2). The resulting drag coefficients are shown in figure 7.6 as a function of the surface based Reynolds number of the cluster. The simulation results agree very well with the predictions from equation (7.4) and thus with the experimental results of Tran-Cong et al. (2004). The influence of the shape factors is very well predicted by our simulations. At low Reynolds numbers all values for the drag coefficients are slightly higher than expected, which is probably due to the periodic boundary conditions. Hasimoto's equation (Hasimoto, 1959) predicts that the drag coefficient of a (spherical) particle in an array at these porosities is about 15 % higher than the drag coefficient of a single particle. Probably the same holds for the irregularly shaped particles that are used here. However, at higher Reynolds numbers the results are slightly lower than the experimental values, which is probably due to the dimensions of the simulation volume: the particle is influenced by the wake of its periodical image. Tests confirm that the deviation becomes worse if the length of the box is decreased. However, increasing the simulation volume is prohibitively expensive. Therefore, the focus in the following will be on low Reynolds numbers.

Increasing the inter-particle distance is found to have a strong effect on the drag force, especially in configurations where one or more particles are shielded by other particles. Figure 7.7 shows a cross-section of the flow in a cluster where the distance between the centres of nearest neighbours is equal to 2.5 times the particle diameter. Compared to figure 7.4 it should be noted that although part of the fluid still flows around the cluster as a whole, the flow profiles in the pores are much stronger developed in this case. This strongly effects the drag force on the particles.

Figure 7.8 shows the average drag coefficients of the particles in the cluster as a function of inter-particle distance. The coefficients are normalised by the

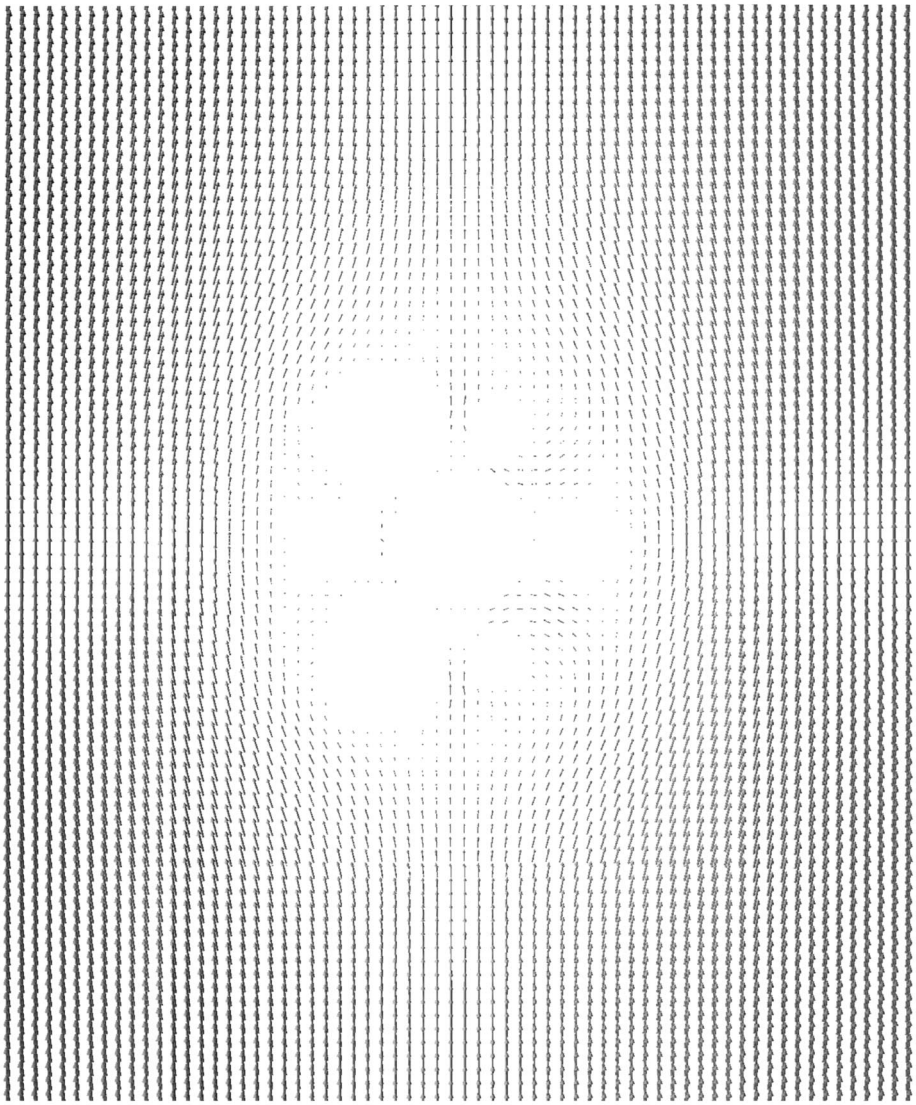

Figure 7.4: Flow profile around an irregularly shaped particle in low Reynolds number regime ($Re_{sp} = 0.058$ for a single constituting particle or $Re_A = 0.13$ for cluster)

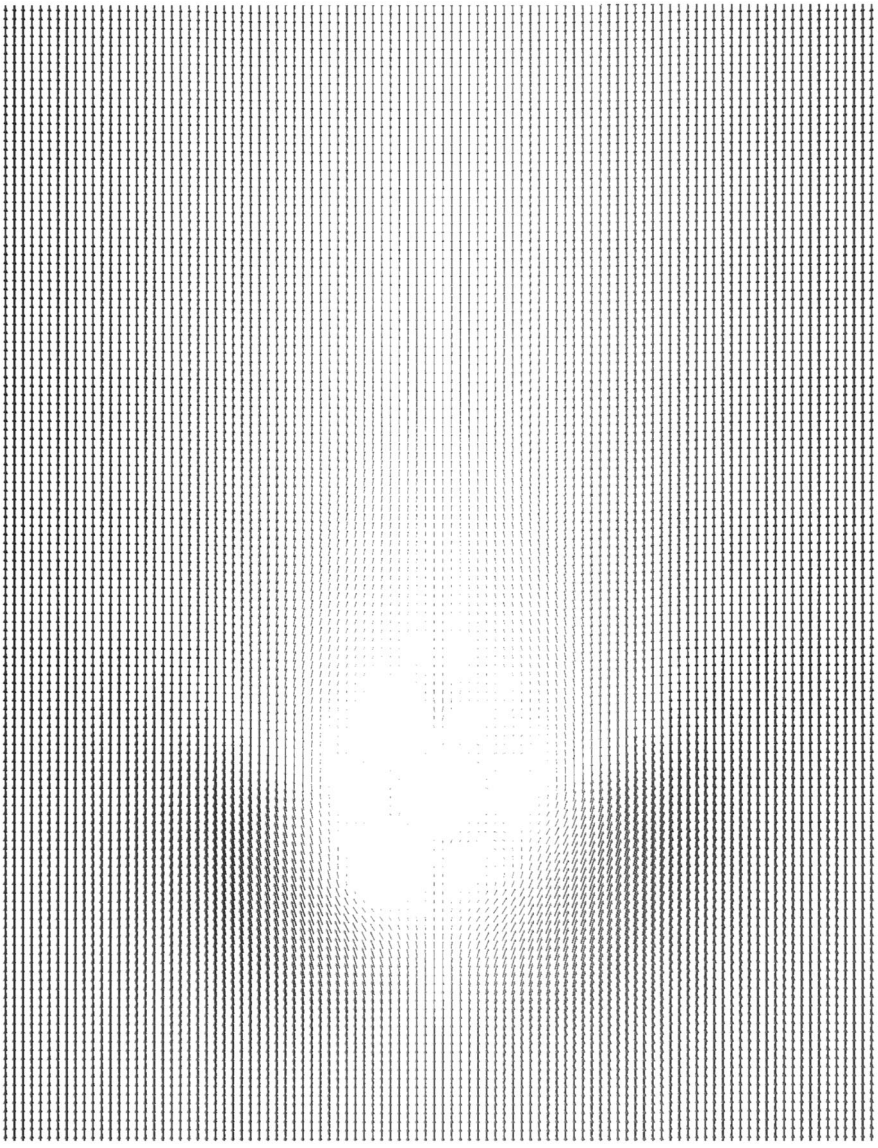

Figure 7.5: Flow profile around an irregularly shaped particle for higher Reynolds number ($Re_{sp} = 5.8$ for a single constituting particle or $Re_A = 13$ for cluster)

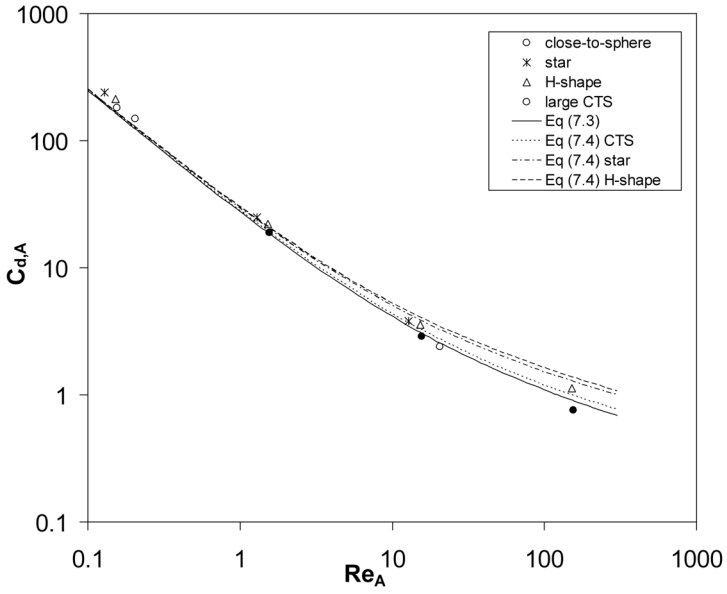

Figure 7.6: Drag coefficients of irregularly shaped particles as a function of the Reynolds number of the cluster (based on projected surface area)

drag of a single particle at the same Reynolds number (according to equation 7.3). The data in this figure were taken from simulations at low Reynolds numbers, but for higher Reynolds numbers (up to order 10) the effect is very similar. At small inter-particle distances the influence of the ratio d_A/d_n is still clearly visible: when a larger fraction of the particles is exposed to the flow, as is the case in the flat H-shaped cluster, the drag force is higher. The 'large CTS'-configuration has the smallest surface to volume ratio, and thus the lowest drag force per particle. At large inter-particle distances this effect disappears, since at that point the fluid moves freely in the pores and the flow profiles around each particle become equal and independent of the positions of other particles. Note that the drag coefficient of the particles at large inter-particle distances reaches a value higher than the drag coefficient of a single particle, since the particles form part of an array instead of being completely solitary particles. In fact, the drag coefficients are in reasonable agreement with Hasimoto's equation, which predicts a value between 1.15 and 1.25, depending on the choice of inter-particle distance (the particle arrays are not regular).

The drag force on individual particles was shown to depend heavily on the

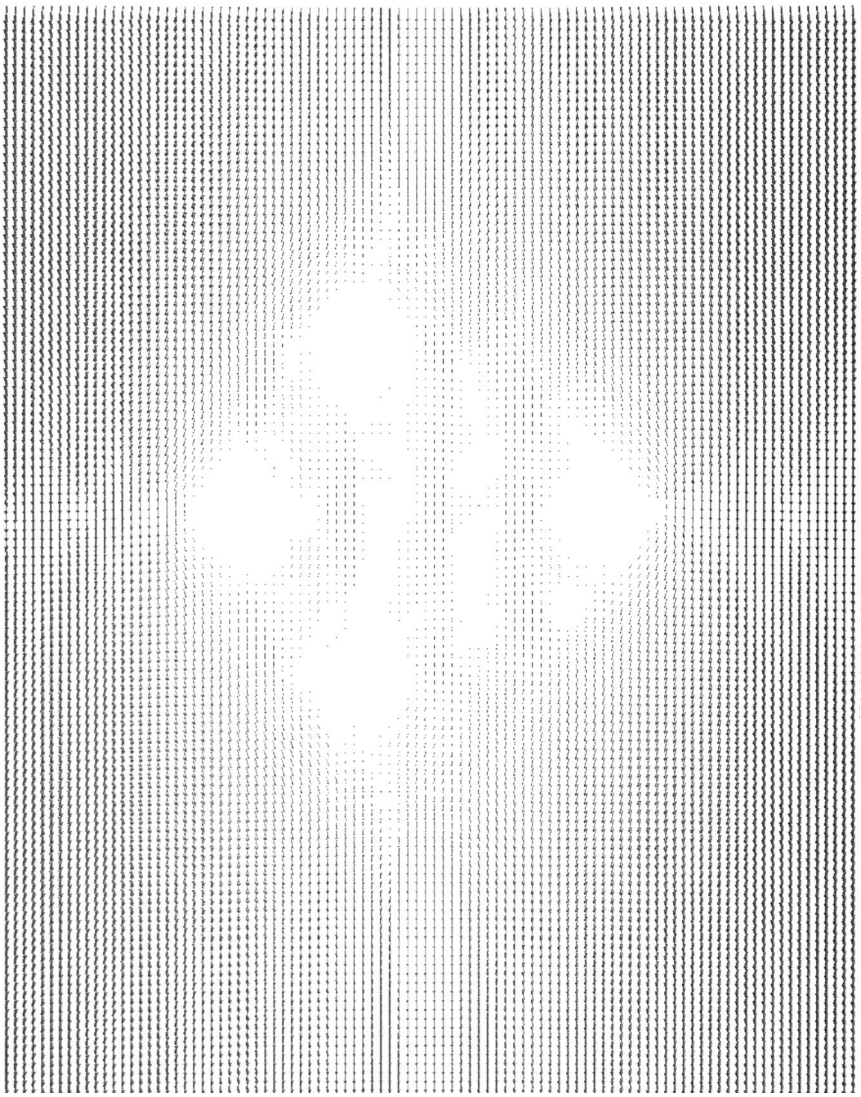

Figure 7.7: Flow profile around a cluster based on the close-to-sphere configuration at low Reynolds number, ($Re_{sp} = 0.058$ for a single constituting particle).

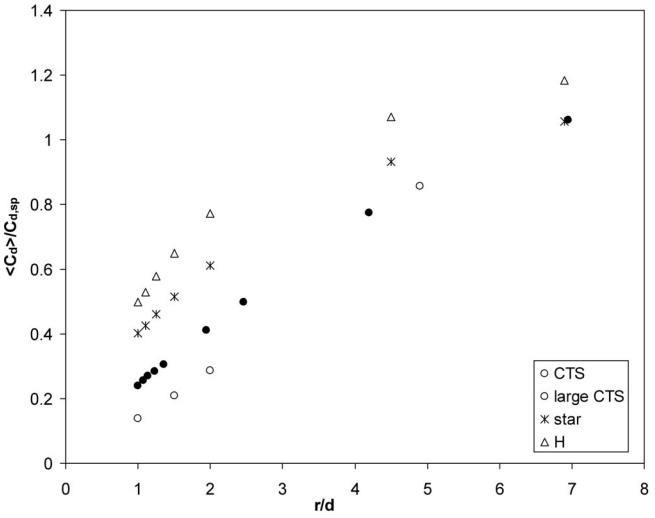

Figure 7.8: Average drag coefficients of particles in clusters of various shapes as a function of inter-particle distance at low Reynolds number, (Re_{sp} = 0.058)

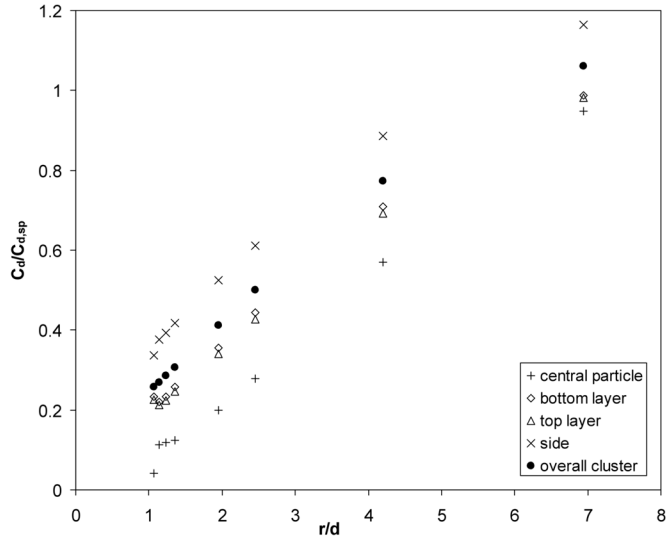

Figure 7.9: Normalised drag coefficients of individual particles in clusters based in the close-to-spherical configuration as a function of inter-particle distance at low Reynolds number, ($\mathrm{Re_{sp}} = 0.058$)

shielding by other particles as well. Figure 7.9 shows the normalised drag coefficients on four different particles in the CTS-configuration as a function of the particle distance at low Reynolds numbers. When the inter-particle distance is small, the fluid in the pores has more or less the same velocity as the particles themselves and the central particle experiences almost no drag force. The particles on the side however experience the strongest velocity gradients, and thus the highest drag force. When the distance is increased, flow patterns in between the particles develop and the drag force on the central particle increases stronger than the average drag force, while the relative contribution of the more exposed particles to the overall drag force decreases. This proves that shielding is an important factor in determining the drag force on individual particles.

Besides the inter-particle distance, the Reynolds number has a strong effect on the drag coefficients of individual particles as well. Figure 7.9 shows that the results for the particles in top and bottom layers are very similar at low Reynolds numbers, as could also be expected from the symmetrical flow patterns (see also figure 7.4). This changes at higher Re when the wake becomes stronger. In that case the force on a particle in the top layer is much lower than the force on a bottom particle if the inter-particle distance is small. At larger distances ($r/d > 5$) the effect of the wake of the cluster as a whole disappears.

7.4 Discussion and conclusions

The simulation results showed that the drag force on an irregularly shaped particle, composed from spheres, is well described by the relation of Tran-Cong et al. (2004). These irregularly shaped particles may also be viewed as clusters with zero inter-particle distances. When the distance between these particles was increased, flow developed in the pores between the particles and the overall drag force on the cluster increased. The drag force on single constituting particles showed a strong dependence on the shielding by other particles.

In the models that are currently used to simulate fluidised-bed reactors, the drag force between gas and particles is usually based on the porosity in a fluid cell, assuming homogeneous distributions within these cells. As an example we look at the configurations in figure 7.10. It should be noted that the porosities for these configurations are equal. Thus, the current models

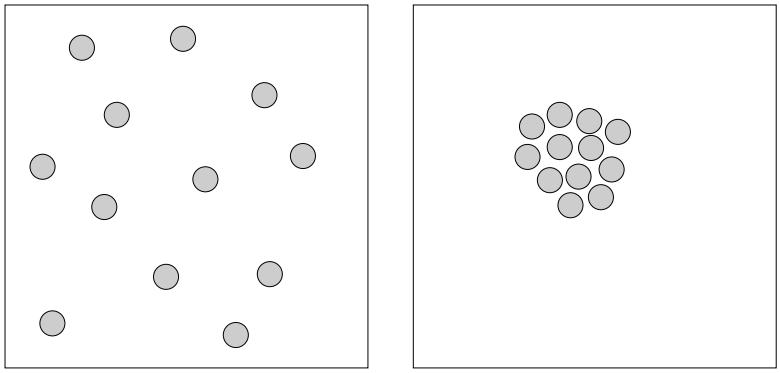

Figure 7.10: Two cells with equal porosities. Left: no clustering. Right: a cluster of particles. The overall drag force in the cell on the right will be much smaller because of the clustering

would assume equal drag forces in both cases. However, our simulations show that the drag force on each particle varies strongly with the inter-particle distance. Omitting the effect of clustering may result in incorrect drag forces and thus non-realistic behaviour in the simulation.

Future research will focus on a method to take clustering into account in the discrete particle models, and possibly the multi-fluid models. A question which is of particular interest is at what inter-particle distance the cluster should not be treated as a single 'large' particle, but rather as a suspension. This transition occurs when the flow starts finding its way through the channels within the cluster, instead of moving primarily around it.

Appendix A

Simulation results

Table A.1: Results from the lattice-Boltzmann simulations for the normalised drag force F in monodisperse arrays of spheres at porosity ε for low Reynolds numbers; ΔF is an estimate for the error in F.

ε	F	ΔF
0.40	38.85	0.33
0.45	27.40	0.24
0.50	20.10	0.22
0.55	15.45	0.13
0.60	11.97	0.12
0.65	8.90	0.14
0.70	7.22	0.06
0.80	4.25	0.07
0.90	2.44	0.04

Table A.2: Results from the lattice-Boltzmann simulations for the normalised drag force F in monodisperse arrays of spheres at porosity ε for intermediate and high Reynolds numbers. α is defined in equation (4.2).

ε	Re	F	α	$\Delta\alpha$
0.40	21.0	48.47	0.4579	0.0165
0.40	30.6	54.62	0.5153	0.0146
0.40	104.9	96.87	0.5526	0.0170
0.40	153.1	121.37	0.5393	0.0111
0.40	209.9	147.33	0.5166	0.0141
0.40	306.3	189.70	0.4930	0.0084
0.40	419.8	234.54	0.4659	0.0073
0.40	612.5	306.62	0.4372	0.0057
0.40	1049.4	455.85	0.3974	0.0056
0.45	21.0	34.43	0.3349	0.0221
0.45	1049.4	333.62	0.2918	0.0064
0.50	21.0	25.51	0.2576	0.0139
0.50	104.9	48.70	0.2726	0.0054
0.50	209.9	74.81	0.2606	0.0032
0.50	419.9	123.82	0.2470	0.0045
0.50	612.5	164.29	0.2354	0.0031
0.50	1049.4	255.40	0.2242	0.0027
0.55	1049.4	210.81	0.1862	0.0027
0.60	21.0	16.13	0.1979	0.0097
0.60	104.9	31.92	0.1902	0.0040
0.60	209.9	49.54	0.1790	0.0033
0.60	420.0	83.11	0.1694	0.0031
0.60	612.5	108.73	0.1580	0.0027
0.60	1049.4	164.74	0.1456	0.0031
0.70	21.0	10.19	0.1413	0.0075
0.70	104.9	20.70	0.1285	0.0031
0.70	209.9	32.72	0.1215	0.0023
0.70	1049.4	110.05	0.0980	0.0021

Continued on next page

Table A.2: *continued*

ε	Re	F	α	$\Delta\alpha$
0.80	21.0	6.24	0.0946	0.0044
0.80	104.9	13.02	0.0836	0.0016
0.80	209.9	20.75	0.0786	0.0014
0.80	1049.4	77.31	0.0696	0.0010
0.90	21.0	3.95	0.0718	0.0024
0.90	104.9	8.37	0.0565	0.0011
0.90	209.9	13.30	0.0518	0.0007
0.90	1049.4	51.10	0.0464	0.0005

Table A.3: Results from the lattice-Boltzmann simulations for the normalised drag force on individual particles and the average normalised drag force in bidisperse arrays of spheres at low Reynolds numbers for various porosities, diameter ratios and mixture compositions.

ε	$\frac{d_1}{d_2}$	$\frac{\phi_2}{\phi}$	F_1	F_2	$\langle F \rangle$
0.35	0.500	0.500	31.42	105.78	51.44
0.40	0.500	0.500	23.06	76.85	37.57
0.40	0.607	0.817	20.10	46.81	38.55
0.40	0.700	0.493	27.94	50.83	36.42
0.50	0.250	0.494	10.69	112.43	22.39
0.50	0.250	0.748	6.65	59.29	23.04
0.50	0.333	0.247	15.70	106.66	21.14
0.50	0.333	0.495	11.45	74.59	22.01
0.50	0.333	0.750	7.39	43.14	21.77
0.50	0.500	0.100	18.67	61.78	20.32
0.50	0.500	0.250	17.37	56.38	21.62
0.50	0.500	0.500	12.75	39.89	20.20
0.50	0.500	0.749	10.28	31.06	21.47
0.50	0.500	0.901	8.47	24.53	21.06
0.50	0.500	0.950	7.23	21.24	19.62
0.50	0.607	0.250	17.01	39.36	20.14
0.50	0.607	0.502	14.27	32.48	20.34
0.50	0.607	0.753	11.65	25.35	20.00
0.50	0.607	0.817	10.94	24.60	20.41
0.50	0.700	0.253	18.20	33.24	20.75
0.50	0.700	0.493	15.44	27.46	19.91
0.50	0.700	0.745	12.94	24.41	20.24
0.60	0.250	0.494	7.23	62.31	14.07
0.60	0.250	0.748	4.68	33.74	14.28
0.60	0.333	0.247	9.29	55.96	12.23
0.60	0.333	0.495	6.98	37.71	12.47
0.60	0.333	0.750	5.14	25.23	13.55
0.60	0.500	0.250	9.86	29.34	12.05

Continued on next page

Table A.3: *continued*

ε	$\frac{d_1}{d_2}$	$\frac{\phi_2}{\phi}$	F_1	F_2	$\langle F \rangle$
0.60	0.500	0.502	8.15	23.33	12.45
0.60	0.500	0.752	6.47	16.56	12.12
0.60	0.607	0.250	9.84	21.54	11.51
0.60	0.607	0.507	8.80	18.30	12.10
0.60	0.607	0.817	6.80	13.33	11.41
0.60	0.700	0.253	10.20	17.41	11.45
0.60	0.700	0.493	9.05	15.08	11.34
0.60	0.700	0.745	8.38	13.62	11.79
0.65	0.500	0.502	6.31	17.03	9.41
0.65	0.700	0.493	7.54	12.24	9.34
0.75	0.500	0.250	4.81	12.06	5.69
0.75	0.500	0.502	3.98	9.28	5.61
0.75	0.500	0.752	3.33	7.09	5.55
0.75	0.607	0.250	4.88	9.18	5.54
0.75	0.607	0.507	4.43	8.37	5.84
0.75	0.607	0.753	3.60	6.52	5.44
0.75	0.607	0.817	3.64	6.40	5.62
0.75	0.700	0.253	5.03	7.81	5.54
0.75	0.700	0.493	4.63	7.31	5.66
0.75	0.700	0.745	4.19	6.14	5.49
0.90	0.500	0.502	2.11	3.64	2.68
0.90	0.700	0.493	2.16	2.90	2.47

Table A.4: Results from the lattice-Boltzmann simulations for the normalised drag force on individual particles and the average normalised drag force in bidisperse arrays of spheres at intermediate and high Reynolds numbers for various porosities, diameter ratios and mixture compositions.

ε	$\frac{d_1}{d_2}$	$\frac{\phi_2}{\phi}$	Re	F_1	F_2	$\langle F \rangle$	α
0.35	0.500	0.500	10	34.94	117.65	57.20	0.5764
0.35	0.500	0.500	100	80.28	275.00	132.47	0.8103
0.35	0.500	0.500	500	233.49	809.17	387.36	0.6718
0.40	0.500	0.500	10	25.56	85.50	41.72	0.4145
0.40	0.607	0.817	10	22.15	51.55	42.46	0.3908
0.40	0.700	0.493	10	31.30	57.17	40.88	0.4462
0.40	0.500	0.500	100	56.95	193.38	93.60	0.5602
0.40	0.607	0.817	100	46.82	106.69	88.26	0.4971
0.40	0.700	0.493	100	70.89	133.68	93.98	0.5756
0.40	0.500	0.500	500	159.81	543.15	262.75	0.4504
0.40	0.700	0.493	500	202.78	378.01	267.39	0.4619
0.50	0.250	0.494	10	12.08	127.09	25.31	0.2918
0.50	0.250	0.748	10	7.42	66.18	25.72	0.2674
0.50	0.333	0.247	10	17.82	121.71	24.02	0.2881
0.50	0.333	0.495	10	12.93	84.54	24.88	0.2873
0.50	0.333	0.750	10	8.32	48.39	24.45	0.2684
0.50	0.500	0.100	10	21.08	69.72	22.95	0.2622
0.50	0.500	0.250	10	19.63	63.22	24.39	0.2765
0.50	0.500	0.500	10	14.59	46.10	23.21	0.3016
0.50	0.500	0.749	10	11.56	35.20	24.28	0.2804
0.50	0.500	0.901	10	9.56	27.49	23.63	0.2563
0.50	0.500	0.950	10	8.11	23.92	22.08	0.2465
0.50	0.607	0.250	10	19.03	44.10	22.54	0.2400
0.50	0.607	0.502	10	16.16	36.67	23.01	0.2664
0.50	0.607	0.753	10	13.21	28.78	22.69	0.2695
0.50	0.607	0.817	10	12.14	27.18	22.57	0.2160
0.50	0.700	0.253	10	20.61	37.68	23.50	0.2748
0.50	0.700	0.493	10	17.46	30.94	22.48	0.2568

Continued on next page

Table A.4: *continued*

ε	$\frac{d_1}{d_2}$	$\frac{\phi_2}{\phi}$	Re	F_1	F_2	$\langle F \rangle$	α
0.50	0.700	0.745	10	14.53	27.35	22.70	0.2452
0.50	0.250	0.494	100	27.11	284.90	56.77	0.3438
0.50	0.250	0.748	100	16.06	144.49	55.98	0.3294
0.50	0.333	0.247	100	40.37	276.31	54.43	0.3330
0.50	0.333	0.495	100	29.25	192.10	56.41	0.3439
0.50	0.333	0.750	100	18.58	108.91	54.88	0.3311
0.50	0.500	0.100	100	48.12	160.19	52.40	0.3208
0.50	0.500	0.250	100	44.19	142.29	54.91	0.3329
0.50	0.500	0.500	100	31.89	101.02	50.80	0.3060
0.50	0.500	0.749	100	26.03	81.41	55.68	0.3421
0.50	0.500	0.901	100	21.19	61.51	52.81	0.3174
0.50	0.500	0.950	100	18.36	54.42	50.23	0.3061
0.50	0.607	0.250	100	42.10	98.57	49.99	0.2985
0.50	0.607	0.502	100	36.40	81.55	51.53	0.3119
0.50	0.607	0.753	100	29.97	66.28	52.05	0.3205
0.50	0.700	0.253	100	47.19	85.59	53.70	0.3295
0.50	0.700	0.493	100	39.23	70.15	50.73	0.3081
0.50	0.700	0.745	100	32.50	61.36	50.88	0.3063
0.50	0.250	0.494	500	71.78	755.37	150.38	0.2560
0.50	0.333	0.495	500	74.80	500.26	145.36	0.2467
0.50	0.500	0.100	500	134.81	449.30	146.83	0.2530
0.50	0.500	0.250	500	111.03	365.48	138.60	0.2340
0.50	0.500	0.500	500	88.57	271.60	139.09	0.2378
0.50	0.500	0.749	500	69.08	215.93	147.72	0.2525
0.50	0.500	0.901	500	55.90	165.89	142.01	0.2419
0.50	0.500	0.950	500	49.38	148.39	136.84	0.2344
0.50	0.607	0.502	500	94.76	212.67	134.25	0.2278
0.50	0.700	0.493	500	105.49	186.82	135.80	0.2318
0.60	0.250	0.494	10	8.32	71.94	16.22	0.2148
0.60	0.250	0.748	10	5.30	38.25	16.19	0.1904
0.60	0.333	0.247	10	10.75	64.71	14.14	0.1911
0.60	0.333	0.495	10	7.96	43.15	14.24	0.1766
0.60	0.333	0.750	10	5.83	28.65	15.38	0.1837
0.60	0.500	0.250	10	11.40	33.91	13.94	0.1885

Continued on next page

Table A.4: *continued*

ε	$\frac{d_1}{d_2}$	$\frac{\phi_2}{\phi}$	Re	F_1	F_2	$\langle F \rangle$	α
0.60	0.500	0.502	10	9.38	27.02	14.38	0.1922
0.60	0.500	0.752	10	7.43	18.86	13.84	0.1722
0.60	0.607	0.250	10	11.39	24.82	13.32	0.1805
0.60	0.607	0.507	10	10.08	20.88	13.84	0.1741
0.60	0.607	0.817	10	7.62	15.18	12.94	0.1534
0.60	0.700	0.253	10	11.77	19.96	13.19	0.1746
0.60	0.700	0.493	10	10.38	17.24	12.98	0.1645
0.60	0.700	0.745	10	9.43	15.54	13.39	0.1604
0.60	0.250	0.494	100	19.53	168.61	38.05	0.2398
0.60	0.250	0.748	100	12.03	87.54	36.92	0.2264
0.60	0.333	0.247	100	25.68	154.12	33.78	0.2155
0.60	0.333	0.495	100	18.50	101.26	33.20	0.2073
0.60	0.333	0.750	100	13.05	64.92	34.69	0.2114
0.60	0.500	0.250	100	27.39	81.94	33.52	0.2147
0.60	0.500	0.502	100	22.40	65.39	34.52	0.2207
0.60	0.500	0.752	100	16.97	43.06	31.60	0.1949
0.60	0.607	0.250	100	27.12	59.06	31.70	0.2018
0.60	0.607	0.507	100	23.52	49.58	32.54	0.2044
0.60	0.607	0.817	100	18.14	35.73	30.54	0.1913
0.60	0.700	0.253	100	27.70	46.78	31.02	0.1957
0.60	0.700	0.493	100	24.27	40.72	30.49	0.1915
0.60	0.700	0.745	100	21.65	35.95	30.92	0.1913
0.60	0.333	0.495	500	48.63	267.63	87.45	0.1500
0.60	0.500	0.502	500	58.83	175.60	91.53	0.1582
0.60	0.700	0.493	500	65.34	111.18	82.60	0.1425
0.65	0.500	0.502	10	7.41	19.71	10.99	0.1572
0.65	0.700	0.493	10	8.82	14.18	10.88	0.1537
0.65	0.500	0.502	100	18.13	47.77	26.79	0.1737
0.65	0.700	0.493	100	20.79	33.92	25.80	0.1646
0.75	0.500	0.250	10	5.73	14.44	6.79	0.1099
0.75	0.500	0.502	10	4.70	11.05	6.65	0.1041
0.75	0.500	0.752	10	3.90	8.35	6.52	0.0968
0.75	0.607	0.250	10	5.84	10.89	6.62	0.1076

Continued on next page

Table A.4: *continued*

ε	$\frac{d_1}{d_2}$	$\frac{\phi_2}{\phi}$	Re	F_1	F_2	$\langle F \rangle$	α
0.75	0.607	0.507	10	5.23	9.81	6.88	0.1039
0.75	0.607	0.753	10	4.29	7.78	6.50	0.1053
0.75	0.607	0.817	10	4.27	7.79	6.78	0.1158
0.75	0.700	0.253	10	5.98	9.21	6.57	0.1034
0.75	0.700	0.493	10	5.30	8.36	6.48	0.0819
0.75	0.700	0.745	10	4.90	7.23	6.45	0.0960
0.75	0.500	0.250	100	14.47	37.23	17.22	0.1152
0.75	0.500	0.502	100	11.58	27.68	16.47	0.1087
0.75	0.500	0.752	100	9.37	20.11	15.68	0.1013
0.75	0.607	0.250	100	14.60	27.49	16.58	0.1104
0.75	0.607	0.507	100	12.75	24.19	16.85	0.1101
0.75	0.700	0.253	100	14.66	22.89	16.15	0.1061
0.75	0.700	0.493	100	13.25	20.43	16.04	0.1038
0.75	0.700	0.745	100	11.51	17.44	15.43	0.0994
0.75	0.500	0.502	500	31.03	77.68	44.93	0.0786
0.75	0.700	0.493	500	38.41	61.93	47.42	0.0835
0.90	0.500	0.502	10	2.73	4.71	3.47	0.0789
0.90	0.700	0.493	10	2.75	3.72	3.16	0.0691
0.90	0.500	0.502	100	7.08	13.01	9.19	0.0651
0.90	0.700	0.493	100	7.29	9.90	8.38	0.0591
0.90	0.500	0.502	500	19.15	38.27	25.56	0.0458

Table A.5: Results from the lattice-Boltzmann simulations for the normalised drag force on individual particles and the average normalised drag force in a polydisperse array of spheres, consisting of four particle types with diameter ratios 1:2:3:4.

ε	$\langle Re \rangle$	F_1	F_2	F_3	F_4	$\langle F \rangle$	$\langle F \rangle_{theory}$
0.502	0.2	7.82	22.23	44.54	75.24	21.22	20.26
0.502	10	8.78	24.95	49.87	84.46	23.81	22.50
0.502	100	19.48	55.37	111.02	188.48	52.92	48.84
0.502	500	54.07	155.73	313.98	530.39	148.37	147.44

Appendix B

Error analysis experiments

As an example the calculation of the error in a monodisperse experiment is presented. The calculation of the uncertainty in bidisperse experiments is very similar and results in errors of the same order.

All pressure drops are measured with an error of 1 % or less. From the pressure drop, the normalised drag force is calculated using equation (2.2):

$$F = \frac{\varepsilon}{(1-\varepsilon)} \frac{d^2}{18\mu U} \frac{\Delta P}{L} \ .$$

The relative error in F is thus given by:

$$\frac{\Delta F}{F} = \frac{\Delta \varepsilon}{\varepsilon} + \frac{\Delta\,(1-\varepsilon)}{(1-\varepsilon)} + 2.0 \cdot \frac{\Delta d}{d} + \frac{\Delta \mu}{\mu} + \frac{\Delta U}{U} + \frac{\Delta\,(\Delta P)}{(\Delta P)} + \frac{\Delta L}{L} \ .$$

The standard deviation in the particle diameter is 2 % or less for all particle species. The distance between the measuring points L, column length L_c and diameter D_c are measured with an accuracy of 0.2 mm.

The porosity is determined from the weight of the particles in the column:

$$\varepsilon = 1 - \phi = 1 - \frac{m_p}{\rho_p V_c} \ .$$

The relative error in the packing fraction ϕ is:

$$\frac{\Delta \phi}{phi} = \frac{\Delta m_p}{m_p} + \frac{\Delta \rho_p}{\rho_p} + 2 \cdot \frac{\Delta D_c}{D_c} + \frac{\Delta L_c}{L_c} = 0.0002 + 0.002 + 2 * 0.0025 + 0.0007 \approx 0.008 \ .$$

The viscosity is determined from the time it takes to fall through a capillary, and the error in this measurement is less than 1%. However, the viscosity is strongly influenced by the temperature, which fluctuates slightly during the experiments and may also depend on position in the reactor. A variation in the temperature of only 0.2 K results in a change in the porosity of almost 2 %, which is why a relative error in the viscosity of 0.03 will be used here. The velocity is determined based on the pump frequency after calibration of this flow, and the error made is estimated to be 1 %.

The relative error in the value for the normalised drag force determined from the experiments is thus:

$$\frac{\Delta F}{F} = 0.015 + 0.008 + 0.001 + 2.0 \cdot 0.02 + 0.03 + 0.01 + 0.001 \approx 0.11 \ .$$

Furthermore, there is also an error in the theoretically predicted value due to the error in the porosity and Reynolds number with which it is calculated. For the low Reynolds regime this error is:

$$\frac{\Delta F_{th}}{F_{th}} = 2 \cdot \frac{\Delta \varepsilon}{\varepsilon} + \frac{\Delta \left(1 - \varepsilon\right)}{\left(1 - \varepsilon\right)} = 2 \cdot 0.015 + 0.008 \approx 0.04 \ ,$$

for high Reynolds numbers the relative error is of the same order. The error in bidisperse systems is comparable to the error in monodisperse systems.

The relative error in the measured normalised drag force is thus 11 %, while the error in the theoretical prediction is 4 %, a total error of 15 %.

Notation

C_d	–	drag coefficient
d	–	particle diameter
F	–	normalised dragforce (normalised by Stokes-Einstein drag)
F_b	N	buoyancy force
F_d	N	drag force
$F_{f\to s}$	N	total force that fluid exerts on particle
k	–	Kozeny constant
m_p	kg	particle mass
N	–	number of particles
P	Pa	pressure
r_h	m	hydraulic radius: ratio of pore volume to surface area of medium
Re	–	Reynolds number
t	s	time
$\mathbf{U}$	m/s	superficial velocity
$\mathbf{u}$	m/s	local fluid velocity
$\mathbf{v}_p$	m/s	particle velocity
V	m^3	system volume
V_p	m^3	particle volume

y_i	$-$	ratio of diameter of type i particle to average diameter, $d_i / \langle d \rangle$
β	$\mathrm{kg/m^3s}$	interphase momentum transfer coefficient
ε	$-$	porosity
κ	$\mathrm{m^2}$	permeability
μ	kg/ms	viscosity
ρ	$\mathrm{kg/m^3}$	fluid density
τ	$\mathrm{kg/ms^2}$	viscous stress tensor
ϕ	$-$	solids packing fraction
χ_i	$-$	fraction of phase i with respect to total solids fraction
$\langle .. \rangle$	[..]	average property

Variables in lattice-Boltzmann model (all in lattice units):

c	$\Delta x / \Delta t$	velocity of grid direction
c_s	$\Delta x / \Delta t$	speed of sound
d	Δx	effective particle diameter
d_0	Δx	initial particle diameter
n	n	discretised velocity distribution
n^{eq}	n	equilibrium velocity distribution
t	Δt	time
$\mathbf{r}$	Δx	position
$\mathbf{u}$	$\Delta x / \Delta t$	velocity
$\mathbf{j}$	$n \Delta x / \Delta t$	momentum
$\mathbf{\Pi}$	$n \left(\Delta x / \Delta t\right)^2$	stress
ρ	$n / \left(\Delta x\right)^3$	density

Bibliography

G.K. Batchelor. Sedimentation in a dilute dispersion of spheres. *J. Fluid Mech.*, 52:245–268, 1972.

G.K. Batchelor. Sedimentation in a dilute polydisperse system of interacting spheres. part 1. general theory. *J. Fluid Mech.*, 119:379–408, 1982.

G.K. Batchelor and C.-S. Wen. Sedimentation in a dilute polydisperse system of interacting spheres. part 2. numerical results. *J. Fluid Mech.*, 124: 495–528, 1982.

S. Berres, R. Bürger, and E.M. Tory. On mathematical models and numerical simulation of the fluidization of polydisperse suspensions. *Appl. Math. Model.*, 29:159–193, 2005.

P.L. Bhatnagar, E.P. Gross, and M. Krook. A model for collision processes in gases. i. small amplitude processes in charged and neutral one-component systems. *Phys. Rev.*, 94:511–525, 1954.

P.M. Biesheuvel. Comments on "a generalized empirical description for particle slip velocities in liquid fluidized beds" by k.p. galvin, s. pratten and g. nguyen tran lam. *Chem. Eng. Sci.*, 55:1945–1947, 2000.

P.M. Biesheuvel, H. Verweij, and V. Breedveld. Microdivers to study sedimentation in polydisperse, concentrated colloidal suspensions. *AIChE J.*, 47:1969–1977, 2001.

G.A. Bokkers. *Multi-level modelling of the hydrodynamics in gas phase polymerisation reactors*. PhD thesis, University of Twente, Enschede, The Netherlands, 2005.

G.A. Bokkers, M. van Sint Annaland, and J.A.M. Kuipers. Mixing and segregation in a bidisperse gas-solid fluidised bed: a numerical and experimental study. *Powder Techn.*, 140:176–186, 2004.

P.C. Carman. Fluid flow through granular beds. *Trans. Inst. Chem. Eng.*, 15:150–166, 1937.

H. Chen, S. Chen, and W.H. Matthaeus. Recovery of the navier-stokes equations using a lattice-gas boltzmann method. *Phys. Rev. A*, 45:R5339–R5342, 1992.

R. Clift, J.R. Grace, and M.E. Weber. *Bubbles, Drops and Particles*. Academic Press, New York, 1978.

R. Di Felice. On the voidage function in two-phase multiparticle systems. *Int. J. Multiphase Flow*, 20:153–159, 1994.

R. Di Felice. Hydrodynamics of liquid fluidisation. *Chem. Eng. Sci.*, 50: 1213–1245, 1995.

H. Enwald, E. Peirano, and A.E. Almstedt. Eulerian two-phase flow theory applied to fluidization. *Int. J. Multiphase Flow*, 22:suppl, 21–66, 1996.

S. Ergun. Fluid flow through packed columns. *Chem. Eng. Progr.*, 48:89–94, 1952.

R.M. Fand, B.Y.K. Kim, A.C.C. Lam, and R.T. Phan. Resistance to the flow of fluids through simple and complex porous media whose matrices are composed of randomly packed spheres. *ASME J. Fluids Eng.*, 109: 268–273, 1987.

P.U. Foscolo, L.G. Gibilaro, and S.P. Waldram. A unified model for particulate expansion of fluidised beds and flow in fixed porous media. *Chem. Eng. Sci.*, 38:1251–1260, 1983.

D. Frenkel and B. Smit. *Understanding molecular simulation; from algorihms to applications*. Academic Press, San Diego/London, 2002.

K.P. Galvin, S. Pratten, and G. Nguyen Tran Lam. A generalized empirical description for particle slip velocities in liquid fluidized beds. *Chem. Eng. Sci.*, 54:1045–1052, 1999.

L.G. Gibilaro, R. Di Felice, S.P. Waldram, and P.U. Foscolo. A predictive model for the equilibrium composition and inversion of binary-solid liquid fluidized beds. *Chem. Eng. Sci.*, 41:379–386, 1986.

D. Gidaspow and B. Ettehadieh. Fluidization in two-dmensional beds with a jet. 2. hydrodynamic modeling. *Ind. Eng. Chem. Fundam.*, 22:193–201, 1983.

M.J.V. Goldschmidt. *Hydrodynamic modelling of fluidised bed spray granulation.* PhD thesis, University of Twente, Enschede, The Netherlands, 2001a.

M.J.V. Goldschmidt, J.M. Link, S. Mellema, and J.A.M. Kuipers. Digital image analysis measurements of bed expansion and segregation dynamics in dense gas-fluidised beds. *Powder Techn.*, 138:135–159, 2003.

H. Hasimoto. On the periodic fundamental solutions of the stokes equations and their application to viscous flow past a cubic array of spheres. *J. Fluid Mech.*, 5:317–328, 1959.

R.J. Hill, D.L. Koch, and A.J.C. Ladd. The first effects of fluid inertia on flows in ordered and random arrays of spheres. *J. Fluid Mech.*, 448: 213–241, 2001a.

R.J. Hill, D.L. Koch, and A.J.C. Ladd. Moderate-reynolds-number flows in ordered and random arrays of spheres. *J. Fluid Mech.*, 448:243–278, 2001b.

B.P.B. Hoomans. *Granular dynamics of gas-solid two-phase flows.* PhD thesis, University of Twente, Enschede, The Netherlands, 1999.

B.P.B. Hoomans, J.A.M. Kuipers, W.J. Briels, and W.P.M. van Swaaij. Discrete particle simulation of bubble and slug formation in a two-dimensional gas-fluidiseed bed: a hard-sphere approach. *Chem. Eng. Sci.*, 51:99–118, 1999.

D. Katoshevski, B. Zhao, G. Ziskind, and E. Bar-Ziv. Experimental study of the drag force acting on a heated particle. *J. Aerosol Sci.*, 32:73–86, 2001.

S. Kim and W.B. Russell. Modelling of porous media by renormalization of the stokes equations. *J. Fluid Mech.*, 154:269–286, 1985.

D.L. Koch and A.S. Sangani. Particle pressure and marginal stability limits for a homogeneous monodisperse gas-fluidized bed: kinetic theory and numerical simulations. *J. Fluid Mech.*, 400:229–263, 1999.

S. Koo and A.S. Sangani. Effective-medium theories for predicting hydrodynamic transport properties of bidisperse suspensions. *Phys. of Fluids*, 14:3522–3533, 2002.

A.J.C. Ladd. Hydrodynamic transport coefficients of random dispersions of hard spheres. *J. Chem. Phys.*, 93:3484–3494, 1990.

A.J.C. Ladd. Numerical simulations of particulate suspensions via a discretized boltzmann equation, part i. *J. Fluid Mech.*, 271:285–339, 1994a.

A.J.C. Ladd and R. Verberg. Lattice-boltzmann simulations of particle-fluid suspensions. *J. Stat. Phys*, 104:1191–1251, 2001.

S.-C. Liang, T. Hong, and L.-S. Fan. Effects of particle arrangements on the drag force of a particle in the intermediate flow regime. *Int. J. Multiphase Flow*, 22:285–306, 1996.

R.S. Maier, D.M. Kroll, H.T. Davis, and R.S. Bernard. Simulation of flow in bidisperse sphere packings. *J. Colloid Interface Sci.*, 217:341–347, 1999.

J.H. Masliyah. Hindered settling in a multi-species particle system. *Chem. Eng. Sci.*, 34:1166–1168, 1979.

G.R. McNamara and G. Zanetti. Use of the boltzmann equation to simulate lattice-gas automata. *Phys. Rev. Lett.*, 61:2332–2335, 1988.

S. Mirza and J.F. Richardson. Sedimentation of suspensions of particles of two or more sizes. *Chem. Eng. Sci.*, 34:447–454, 1979.

G. Mo and A.S. Sangani. A method for computing stokes flow interactions among spherical objects and its application to suspensions of drops and porous particles. *Phys. of Fluids*, 6:1637–1652, 1994.

H. Moritomi, T. Iwase, and T. Chiba. A comprehensive interpretation of solid layer inversion in liquid fluidised beds. *Chem. Eng. Sci.*, 37:1751–1757, 1982.

H. Moritomi, T. Yamagishi, and T. Chiba. Prediction of complete mixing of liquid-fluidized binary solid particles. *Chem. Eng. Sci.*, 41:297–305, 1986.

N.-Q. Nguyen and A.J.C. Ladd. Lubrication corrections for lattice-boltzmann simulations of particle suspensions. *Phys. Rev. E*, 66:046708, 2002.

V.S. Patwardhan and C. Tien. Sedimentation and liquid fluidization of solid particles of different sizes and densities. *Chem. Eng. Sci.*, 40:1051–1060, 1985.

Y.H. Qian, D. d'Humires, and P. Lallemand. Lattice bgk models for navier-stokes equation. *Europhys. Lett.*, 17:479–484, 1992.

J.F. Richardson and W.N. Zaki. Sedimentation and fluidisation: part 1. *Trans. Instn Chem. Engrs.*, 32:35–53, 1954.

A.S. Sangani and A. Acrivos. Slow flow through a periodic array of spheres. *Int. J. Multiphase Flow*, 8:343–360, 1982.

L. Schiller and A. Naumann. über die grundlegenden berechnungen bei der schwerkraftaufbereitung. *Ver. Deut. Ing. Zeitung*, 77:318–320, 1933.

M. Syamlal. *Multiphase hydrodynamics of gas-solid flow*. PhD thesis, Illinois Institute of Technology, Chicago, U.S.A., 1985.

A. Tewari and A.M. Gokhale. Nearest-neighbor distances between particles of finite size in three-dimensional uniform random microstructures. *Mater. Sci. Eng.*, 385:332–341, 2004.

D.M.E. Thies-Weesie and A.P. Philipse. Liquid permeation of bidisperse colloidal hard-sphere packings and the kozeny-carman scaling relation. *J. Colloid Interface Sci.*, 162:470–480, 1994.

L.T. To and Z.H. Stachurski. Random close packing of spheres in a round cell. *J. Non-Cryst. Solids*, 333:161–171, 2004.

S. Tran-Cong, M. Gay, and E.E. Michaelides. Drag coefficients of irregularly shaped particles. *Powder Tech.*, 139:21–32, 2004.

R. Turton and O. Levenspiel. A short note on the drag correlation for spheres. *Powder Techn.*, 47:83–86, 1986.

M.A. van der Hoef, M. Ye, M. van Sint Annaland, and J.A.M. Kuipers. Multi-level modeling of gas-fluidized beds. *to appear in Adv. Chem. Eng.*, 2005.

C.Y. Wen and Y.H. Yu. Mechanics of fluidization. *Chem. Eng. Progr. Symp. Series*, 62:100–111, 1966.

C. Zhu, K. Lam, H.H. Chu, X.D. Tang, and G.Liu. Drag forces of interacting spheres in power-law fluids. *Mech. Res. Comm.*, 30:651–662, 2003.

A.A. Zick and G.M. Homsy. Stokes flow through periodic arrays of spheres. *J. Fluid Mech.*, 115:13–26, 1982.

Dankwoord

Na bijna vijf jaar onderzoek (en al ruim elf jaar in Twente), is nu dan eindelijk mijn proefschrift gereed. Een tijd om even terug te kijken op die periode, en vooral om even stil te staan bij de mensen die me in al die tijd gesteund hebben.

Toen mij ruim vijf jaar geleden, tijdens mijn afstuderen gevraagd werd of ik interesse had in een promotie-opdracht, moest ik daar nog wel even over nadenken. Ik was er niet helemaal van overtuigd dat het wel iets voor mij was om me vier jaar lang met één project bezig te houden, en wist ook niet of ik wel nog vier jaar in Enschede wilde blijven wonen. Uiteindelijk heb ik toch voor die promotie gekozen. Hoewel het af en toe met vallen en opstaan is gegaan en ik het begrip 'promotiedip' ook zeker heb ondervonden, heb ik een goede tijd gehad en veel geleerd.

Aan mijn promotor Hans Kuipers ben ik zeer veel dank verschuldigd, omdat hij mij de kans heeft geboden deze promotie tot een goed einde te brengen en voor alle begeleiding en aanwijzingen die ik gedurende de afgelopen vijf jaar heb mogen ontvangen. Ook mijn dagelijks begeleider Martin van der Hoef wil ik hier bedanken voor de vele discussies en voor de simulaties die hij gedaan heeft, en omdat hij er altijd in is blijven geloven, zelfs wanneer ik zelf in een dip zat.

FOM heeft het onderzoek gefinancierd, en NCF zorgde voor rekentijd bij Sara in Amsterdam. Zonder die steun had dit proefschrift er niet gelegen.

Many thanks to Anthony Ladd for allowing us to use his lattice-Boltzmann code, without which I could not have done the job. His suggestions were also highly appreciated.

Aan het eind van mijn promotie heb ik Wil Paping mogen begeleiden bij zijn afstudeeropdracht, die ik wil bedanken voor alle gedane experimenten en

het enthousiasme waarmee hij altijd op zoek ging naar nieuwe mogelijkheden voor de opstelling. Ook Wil's familie wil ik hierbij betrekken vanwege het vele rijgwerk dat ze gedaan hebben voor de tweede opstelling; het is jammer dat deze experimenten helaas niet meer in dit boekje gepubliceerd konden worden.

Robert Brouwer heeft de opstellingen gebouwd, bedankt daarvoor. Wat begon als een simpel schetsje op een kladblaadje bleek in de praktijk toch vaak lastiger dan gedacht; vooral het lekdicht maken van de tweede opstelling en het snel genoeg rond kunnen pompen van de glycerine hadden nog heel wat voeten in de aarde. Ook de andere technici wil ik bedanken voor het meedenken en de goede suggesties, en Robert Meijer ook voor de ondersteuning op computer gebied.

Martin van Sint Annaland heeft geholpen met de visualisatie-software voor de deeltjesconfiguraties en de snelheden. Maarten Biesheuvel heeft mij op enkele artikelen over sedimentatie van bi- en polydisperse systemen gewezen, en een belangrijke bijdrage geleverd aan de inversie-berekeningen.

Nicole, Ria en tijdens de vakantie ook Irene, bedankt voor de administratieve ondersteuning en de gezelligheid. Ook vele andere diensten binnen de faculteit hebben het mogelijk gemaakt dat ik me op mijn werk kon richten zonder me druk te hoeven maken over alles wat daarmee (zijdelings) verband houdt.

De afgelopen vijf jaar zouden natuurlijk niet hetzelfde zijn geweest zonder alle collega's en afstudeerders. Bedankt allemaal voor de hulp bij computerproblemen, het onderhoud van het cluster, codes voor validatie en tips met betrekking tot die codes en alles wat ik hier vergeet. Maar bovenal bedankt voor de vele discussies in de pauze, lezingen, vakgroepuitjes, zeilweekenden en niet te vergeten de borrels; dit alles maakte het Vlugterlab tot een geweldige werkomgeving. Ook Liesbeth Kuipers wil ik hier bedanken voor het enthousiasme waarmee ze het jaarlijkse Waarbeekfeest, de skivakanties en vele andere gezellige uitjes regelde.

Naast het werken was er natuurlijk meer. Vrijwel elke dinsdagavond bracht ik bij MSO door, eerst alleen met de harp (en vaak zelfs alleen de 'derde helft') maar de laatste tweeeneenhalf jaar ook op viool. Bedankt voor alle onvergetelijke momenten, zoals de reizen, de repetitieweekenden en vaak bijzondere concerten (van 'Romeo en Julia' tot 'Jesus is alive' en 'Lord of the Rings').

De groep van 'The Cat' zorgde voor gezelligheid bij het jaarlijkse Catweek-

end en alle verjaardagen. Door alle concerten en de laatste tijd door de drukte was ik misschien niet altijd aanwezig, maar de keren dat ik er wel was waren (wat mij betreft) zeker de moeite waard. Ook jullie steun tijdens de laatste maanden heb ik zeer op prijs gesteld! Ook alle andere vrienden en vriendinnen wil ik bedanken voor de leuke jaren. Mensen bij naam noemen houdt altijd het risico in dat je iemand vergeet en daarom doe ik het maar niet, maar alle mailtjes, avondjes uit of juist op de bank zitten bijkletsen, wandelingen, middagjes shoppen enzovoort waren altijd een welkome afwisseling.

En last maar zeker niet least ben ik mijn ouders en broer(tje) zeer dankbaar voor alle steun die zij mij altijd gegeven hebben. In moeilijke perioden kon ik altijd op hen terug vallen, en ze waren altijd bereid mee te denken over wat er nog moest gebeuren, of te helpen met kralen rijgen of andere zaken buiten het werk om.

Nogmaals bedankt allemaal!

Renske

Levensloop

Renske Beetstra werd op 6 april 1976 geboren in Voorburg. Na de lagere school in Apeldoorn behaalde zij in 1994 haar VWO-diploma aan het Gymnasium Apeldoorn. In juli van datzelfde jaar nam ze deel aan de Internationale Chemie Olympiade in Oslo (Noorwegen), alwaar zij een gouden medaille behaalde.

In september 1994 werd begonnen met de studie Chemische Technologie aan de Universiteit Twente in Enschede. Tijdens deze studie liep ze stage bij Auburn University in Auburn, Alabama (VS) waarbij een verpakkingsproces en de regeling daarvan gemodelleerd werden. De studie werd in mei 2000 afgesloten met een afstudeeropdracht in de groep 'Fundamentele Aspecten van de Procestechnologie' op het gebied van de modellering van wervelbedden, waarbij aannames uit de kinetische theorie voor granulaire stroming geverifiëerd werden met behulp van een discrete deeltjes model.

In november 2000 begon Renske met een promotieonderzoek naar de wrijvingskracht tussen vaste deeltjes en fluïda met behulp van rooster-Boltzmann modellen in de groep 'Fundamentele Aspecten van de Procestechnologie'. De resultaten van dat onderzoek staan in dit proefschrift beschreven.